Title
Design and Analysis of Programmable Receiver Front-Ends Based on LPTV Circuits

Author
Hameed, Sameed

Publication Date
2017

Peer reviewed|Thesis/dissertation

UNIVERSITY OF CALIFORNIA

Los Angeles

Design and Analysis of Programmable Receiver Front-Ends Based on LPTV Circuits

A dissertation submitted in partial satisfaction
of the requirements for the degree
Doctor of Philosophy in Electrical Engineering

by

Sameed Hameed

2017

ABSTRACT OF THE DISSERTATION

Design and Analysis
of Programmable Receiver Front-Ends
Based on LPTV Circuits

by

Sameed Hameed
Doctor of Philosophy in Electrical Engineering
University of California, Los Angeles, 2017
Professor Sudhakar Pamarti, Chair

Wide programmability is increasingly desirable in transceiver designs. Due to the proliferation of frequency bands that need to be supported in wireless standards, such as LTE, WiFi, etc., the continued reliance on bulky off-chip SAW/BAW filters and on-chip inductors in current receiver designs is increasingly untenable. Hence, more integrated approaches are necessary, especially for future radio concepts, such as cognitive radios (CRs), where the channel bandwidth and center frequency are dynamic and not known a-priori. Current state-of-the-art on-chip receiver designs rely on techniques such as discrete-time analog signal processing, N-path filtering, and the mixer-first receiver topology. Nevertheless, on-chip filtering still does not approach the selectivity or linearity of their off-chip counterparts. Hence, new approaches are necessary.

This work presents a programmable receiver front-end that uses the recently developed concept of Filtering-by-Aliasing (FA). By utilizing a linear, periodically time-varying (LPTV) circuit with a sampled output, sharp baseband filtering is achieved that can be upconverted to any desired LO frequency with an integrated passive mixer. Further, to achieve impedance matching with the antenna, an S_{11} constraint is added to the design of the FA filters, while time-interleaving is applied to further increase filter sharpness. Measurements on a fabricated prototype achieved a wide LO tuning-range of 0.1-1GHz, wide filter bandwidth (BW)

tunability, a filter stop-band suppression of 70dB with a transition band only 4×BW, high close-in blocker tolerance with >21dBm IIP_3 at only 1.2×BW offset frequency, and a wide-band S_{11} better than -9dB throughout the LO range. Further, an analysis technique for general LPTV circuits is developed utilizing the concept of conversion matrices. By deriving conversion matrix-based frequency-domain equivalent circuits, LPTV circuits can be analyzed just like LTI circuits. Circuit laws, such as KVL and KCL can be easily applied to derive frequency responses. Example applications to mixer-first receivers, N-path filters, and the problem of impedance matching in LPTV circuits are highlighted to showcase the utility of the analysis technique.

The dissertation of Sameed Hameed is approved.

Subramanian Srikantes Iyer

Danijela Cabric

Babak Daneshrad

Sudhakar Pamarti, Committee Chair

University of California, Los Angeles

2017

To my family ...

for their unwavering support and understanding

TABLE OF CONTENTS

LIST OF FIGURES

LIST OF TABLES

ACKNOWLEDGMENTS

I would to express my sincere gratitue to my research advisor, Prof. Sudhakar Pamarti. This work would not have been possible without his continuous support and guidance. His patience and depth of knowledge went a long way in helping to bring this work to fruition. One cannot count the number of times he has spent discussing research with me late into the night. He is undoutably one of the easist research advisors to work with, even while challenging students to do the best they can.

I would also like to thank my committee members Prof. Babak Daneshrad, Prof. Danijela Cabric and Prof. Subramanian Iyer for their valuable time and inputs. I would also like to thank Prof. Milos Ercegovac who was previously on my committee. I am also indebted to Prof. Asad Abidi, Prof. Behzad Razavi, Prof. Alan Willson, Prof. Shervin Moloudi and others for their comprehensive courses in circuit design, signal processing and communication systems. They have no doubt made me a better electrical engineer.

I would like to acknowledge the following organizations for funding my research: National Science Foundation through NSF Grant ECCS 1408647, UCLA Graduate Division through its Dissertation Year Fellowship, and finally Broadcom Foundation and MediaTek through their fellowships. I would also like to thank Prof. Frank Chang and TSMC for providing chip fabrication for my first chip described in Chapter 2.

I would like to thank Dr. Mansour Rachid for initiating this research direction and for discussions. I am grateful for the time I had with my fellow group members Neha Sinha, Manas Bachu, Abhishek Ghosh, Farid Shirinfar, Jeffrey Lee, Nitin Nidhi, and others. They were the best support one could hope for in graduate school. I would also like to thank my friends - Shailesh, Chetan, Mukul, Abishek, Ashwath, Mihir, Hari, Kirti, Qaiser, Joseph, Anurag, Hitesh, and Pranay among many others who made my stay at UCLA memorable.

I am also deeply grateful to my girlfriend, Sonia, who has kept me lively and happy. She has been there for me throughout and has constantly helped and encouraged me both inside as well as outside of work. Last, but not the least, I would like to express my deep gratitude towards my parents and family for their constant love, support and dedication.

VITA

2010	Research Intern, Department of Electrical Communication Engineering, IISc Bangalore, Bengaluru, India.
2011	B. Tech. (Electrical Engineering), IIT Madras, Chennai, India.
2011–2016	Graduate Student Researcher, Electrical Engineering Department, UCLA, Los Angeles, California.
2013	RFIC Design Intern, Broadcom Corporation, Irvine, California.
2013	M.S. (Electrical Engineering), UCLA, Los Angeles, California.
2014	Teaching Assistant, Electrical Engineering Department, UCLA, Los Angeles, California.
2015	Special Reader, Electrical Engineering Department, UCLA, Los Angeles, California.
2016–present	RFIC Design Intern, Silvus Technologies, Inc., Los Angeles, California.

PUBLICATIONS

Hameed, S.; Pamarti, S., "A Time-Interleaved Filtering-by-Aliasing Receiver Front-End Achieving >70dB Suppression at <4×Bandwidth Frequency Offset," *2017 IEEE International Solid-State Circuits Conference Digest of Technical Papers (ISSCC)*, pp.418,419, Feb. 5-9 2017.

Pamarti, S.; Sinha, N.; Hameed, S.; Rachid, M., "Time-Varying Circuit Approaches for Software Defined and Cognitive Radio Applications," *2016 International SoC Design Conference (ISOCC)*, Jeju, South Korea, pp. 155-156, Oct. 2016.

Hameed, S.; Sinha, N.; Rachid, M.; Pamarti, S., "A Programmable Receiver Front-End Achieving >17dBm IIP_3 at <1.25×BW Frequency Offset," *2016 IEEE International Solid-State Circuits Conference Digest of Technical Papers (ISSCC)*, pp.446,447, 31 Jan.-4 Feb. 2016.

Hameed, S.; Rachid, M.; Daneshrad, B.; Pamarti, S., "Frequency-Domain Analysis of *N*-Path Filters Using Conversion Matrices," *Circuits and Systems II: Express Briefs, IEEE Transactions on* , vol.63, no.1, pp.74-78, Jan. 2016.

Hameed, S.; Rachid, M.; Daneshrad, B.; Pamarti, S., "Frequency-Domain Analysis of a Mixer-First Receiver Using Conversion Matrices," *Circuits and Systems (ISCAS), 2015 IEEE International Symposium on* , vol., no., pp.541,544, 24-27 May 2015.

Hameed, S.; Shin, J.; Chang, M.-C.F.; Pamarti, S., "A 9.8-bit ENOB 1.25 GHz Open-Loop Phase Modulator," *2014 Government Microcircuit Applications & Critical Technology (GOMACTech) Conference*, pp.211,215, 31 March-3 April 2014.

Shin, J.; Hameed, S.; Gu, Q.J; Chang, M.-C.F.; Pamarti, S., "A Wide Bandwidth Open-Loop Phase Modulator," *2013 Government Microcircuit Applications & Critical Technology (GOMACTech) Conference*, 11-14 March 2013.

CHAPTER 1

Introduction

1.1 Motivation

The demand for data continues unabated. Data requirements are projected to increase exponentially in the foreseeable future, driven primarily by portable devices. To keep up with this increasing demand, scarce wireless spectrum has been increasingly partitioned and allocated under modern communication standards such as LTE and WiFi [1, 2]. LTE has already been proposed for more than 40 different licensed frequency bands worldwide according to local availability of spectrum. LTE in unlicensed spectrum (LTE-U) is a proposal that calls for use of unlicensed spectrum to improve LTE network performance when licensed spectrum is scarce or congested [1]. Similarly WiFi has been proposed to be used in the sub-GHz digital TV bands when they are unoccupied by TV signals in an opportunistic manner [2]. Hence, there is increasing diversity in the specific frequency bands used worldwide for common communication standards. The situation is expected to be exacerbated with widespread adoption of networked everyday devices, the paradigm also known as the "*Internet of Things*" [3].

Another theme in the continued development of wireless networks has been opportunistic use of licensed spectrum. Studies have found that many licensed bands are vacant for a large fraction of time. Hence it has been proposed that such unutilized bands can be detected and used by a secondary set of users that rely on intellignet radios. These intelligent radios, referred to as cognitive radios [4] will sense vacant spectrum, and utilize them as long as the primary licensee to the spectrum is inactive. A cognitive radio, thus realized, is expected to quickly scan through a large range of frequency bands to find vacant spectrum, and rapidly begin utilization once a vacant slot is found so as to maximize overall system throughput.

A common theme to these developments is that wireless radios are increasingly expected to be reconfigurable, both in center frequency and bandwidth. In case of a standards-based receiver, this is to ensure reduced dupliation of radio components while supporting multiple frequency bands. In case of a cognitive radio, reconfigurability is essential to operate in a vacant band that is not known a-priori. Further, these radios will also be subjected to large unwanted blocker signals in bands adjacent to their operational frequency, while simultaneously being required to ensure low interference to licensed users in adjacent bands. Conventional radios are ill-suited for use in such reconfigurable radios due to the following:

- Conventional radios use inductors to tune to their center frequency. However, such tuning is narrow-band and is usually limited in range, thus requiring multiple parallel inductor-based front-ends to cover a large range of frequency bands. Moreover, inductors are bulky and do not scale with process and so are not cost-effective.
- Conventional radios also rely on sharp off-chip SAW/BAW band-select filters to filter blockers in the adjacent bands. Unfortunately, such filters are fixed in center frequency and bandwidth, while also being large compared to the rest of the radio.

Hence new architectures are necessary for future wireless radios. A few archiectures have already been proposed in literature towards this effect.

1.2 Reconfigurable Radio Architectures

1.2.1 The Software Radio Architecture

The simplest architecture for a fully reconfigurable wireless radio is the so-called Software Radio architecture shown in Fig. 1.1 [5]. Here, the antenna directly interacts with a wide-band analog-to-digital converter (ADC) and digital-to-analog converter (DAC). The data converters in turn interact with a fully flexible back-end digital signal processing (DSP) core that isolates the signal in the desired frequency bands.

While this architecture is simple, it is impractical simply because from the high per-

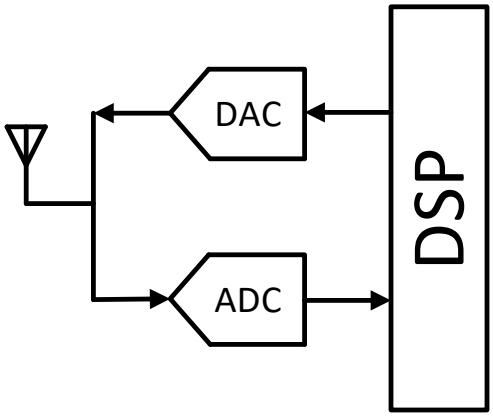

Figure 1.1: The software radio architecture

formance required of the data converters. For example, the ADC experiences the full RF signal swing at the antenna and so must digitize a small wanted signal without corrupting it in the presence of arguably much larger unwanted blockers occupying the same spectrum. Hence, the dynamic range requirements on the ADC are prohibitively large. For example, for a sampling frequency of F_s=1GHz, a moderate dynamic range of 100dB requires about 10W of power [6]. This is significantly larger than the typical power budget of a portable device. Moreover, most of the digitized data is wasted since only a small range of frequencies in the spectrum contains the wanted signal. Hence research has focused on less demanding architectures.

1.2.2 The Software-Defined Radio Architecture

A more practical approach that has gained acceptance in literature is the Software-Defined Radio (SDR) architecture [7]. The idea is to use reconfigurable signal-conditioning circuitry before the data converters so that they don't have to handle the full dynamic range of the RF signals. Hence the requirements on the data converters are moderated and more easily realizable using present technology. As shown in Fig. 1.2, this involves addition of a tunable transmitter after the DAC that will shape the DAC output to ensure that the transmitted signal is accurate, but does not interfere with signals outside the radio's frequency band. In case of the ADC, the preceding reconfigurable receiver is expected to remove unwanted out-

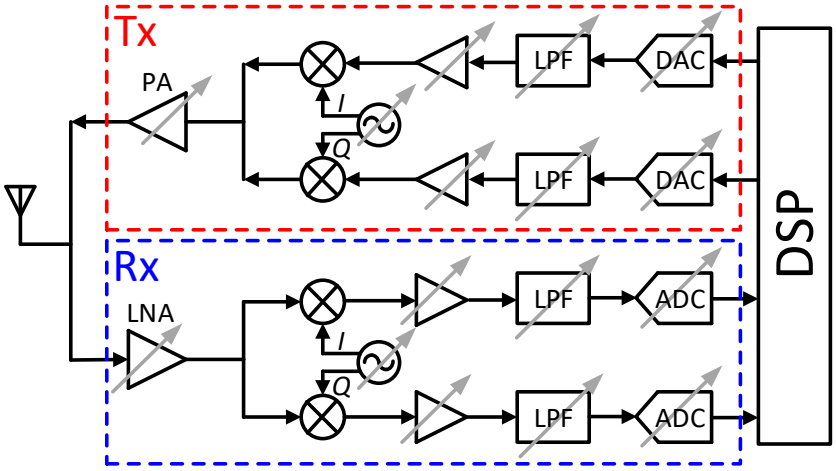

Figure 1.2: The software-defined radio architecture

of-band signals, while ensuring that the in-band signal is uncorrupted. Clearly the challenge in this approach is to design the reconfigurable blocks to ensure adequate performance of the radio over a large range of input signal frequencies. While both the tunable transmitter and reconfigurable receiver are open research problems, this dissertation focuses on realizing highly programmable receivers.

1.3 The Programmable Receiver Problem

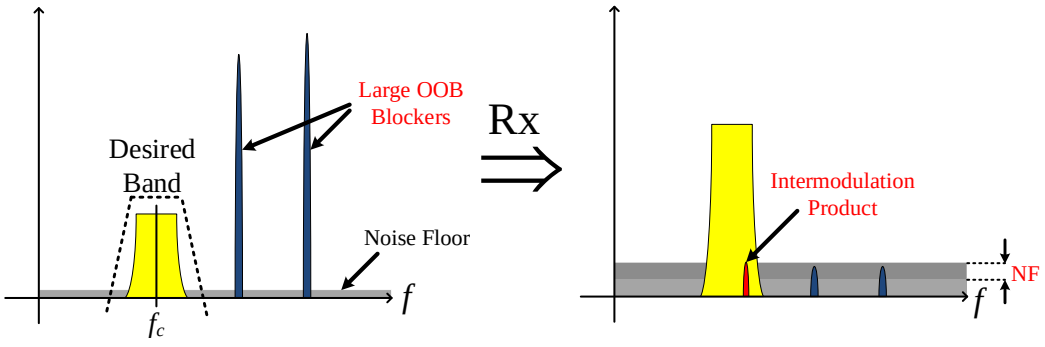

Figure 1.3: The receiver problem

A conventional wireless receiver isolates a wanted input signal from the antenna for demodulation. As shown in Fig. 1.3, the desired signal band (centered around a known center frequency, f_c, with a known bandwidth) may be small and is usually surrounded by

large out-of-band (OOB) blockers. Hence the receiver is expected to filter out all unwanted content before providing the wanted signal to data converters for digitization and further processing. However, receiver non-idealities may corrupt the wanted in-band signal: first, the receiver may add noise, thus degrading the signal-to-noise ratio (SNR) of the wanted signal limiting the range or data-rate of the communication system. Second, any non-linearity in the receiver could lead to the large OOB signals producing in-band intermodulation (IM) distortion products that can further corrupt the wanted signal. Hence receivers are expected to be designed for:

- High dynamic range (DR)
  - Low noise figure (NF) to reduce SNR degradation.
  - High linearity ($\mathrm{IIP}_3/\mathrm{IIP}_2/B_{\mathrm{1dB},CP}$) to minimize IM proucts.
- Impedance matching to antenna interface
  - Good S_{11} to minimize transmission line effects.
  - Allows use of off-chip filters if necessary.

These requirements make receiver design a significant challenge.

In case of a programmable receiver, the design constraints are further compounded. While a programmable receiver has to achieve all the requirements placed on a conventional receiver, it also has to achieve it for a range of operating conditions. Hence such a receiver has to implement highly programmable band-pass filters to isolate the wanted signal, while achieving impedance matching, low noise and high linearity for a wide array of center frequencies and channel bandwidths. Hence a significant amount of research has focused on this problem.

1.4 Organization of the Dissertation

This dissertation tackles the challenge of realizing programmable receivers using a new approach based on linear, periodically time-varying (LPTV) circuits. As shown in the example

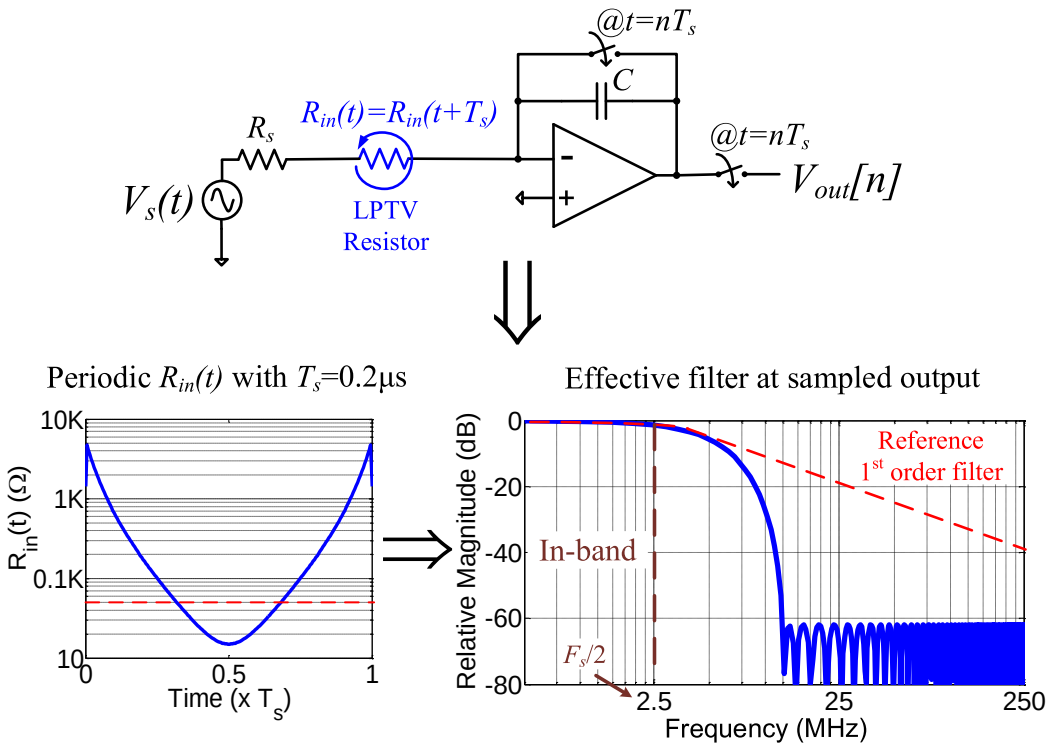

Figure 1.4: Sharp filtering using LPTV circuits

in Fig. 1.4, sharp filtering is achieved by using LPTV components in combination with the recently formulated technique of Filtering by Aliasing (FA) [8]. The rest of this dissertation discusses how LPTV circuits can be used to implement highly programmable receivers and develops analysis techniques to analyze such circuits.

Chapter 2 describes the design of a programmable receiver front-end based on the LPTV circuit shown in Fig. 1.4 and its implementation.

Chapter 3 details improvements to the receiver by time-interleaving multiple LPTV front-ends and the achieved results.

Chapter 4 develops an analysis technique that extends LTI circuit analysis methods to LPTV circuits using the concept of conversion matrices.

Chapter 5 discusses impedance matching in programmable receiver front-ends based on LPTV circuits using conversion matrices.

Finally **Chapter 6** concludes the dissertation with some discussion on future work.

CHAPTER 2

A Programmable Receiver Front-End Based on LPTV Circuits

2.1 Introduction

A programmable receiver front-end is essential to the operation of an SDR [7]. Traditional radios utilize off-chip SAW/BAW filters to suppress OOB blockers before the main receiver front-end. However, due to their bulky and non-reconfigurable nature they are ill-suited for SDR applications. While recent works have attempted to introduce some programmability in off-chip filters [9], their performance has been insufficient for practical use. Hence research has concentrated on fully on-chip filtering solutions to achieve reconfigurability.

2.2 Prior Art

On-chip approaches have primarily been based on a combination of three techniques:

- Discrete-time (DT) charge-domain signal processing [7, 10, 11, 12, 13, 14].
- N-path filtering [14, 15, 16, 17, 18].
- The mixer-first receiver topology [19, 20, 21, 22].

DT approaches rely on directly sampling the RF signal on a capacitor and subsequently processing the stored charge using switched-capacitor techniques. The general structure of a DT receiver front-end is shown in Fig. 2.1. The availability of high-quality switches with high clock rates in deep sub-micron CMOS technologies makes this an attractive approach. One

of the earliest efforts at an SDR were based on such a DT approach with multiple stages of integration sampling [11]. Subsequent works rely on implementing DT-IIR filters via charge sharing between capacitors for sharp filtering of the received signal [12, 13, 14]. However, DT approaches are generally limited in linearity by the first sampling stage (usually an active LNTA that sees the entire RF signal swing).

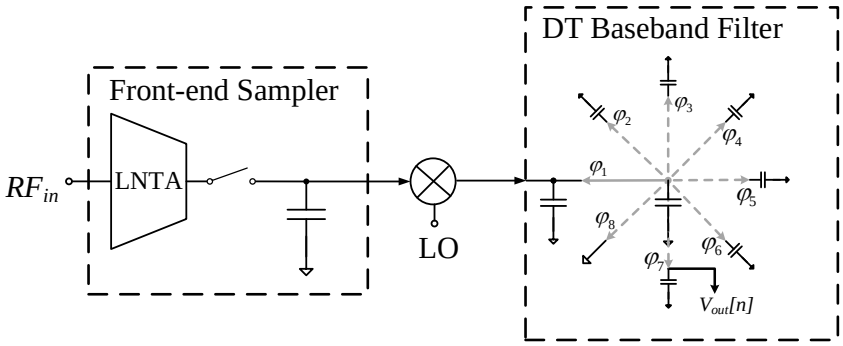

Figure 2.1: Discrete-time receiver front-ends

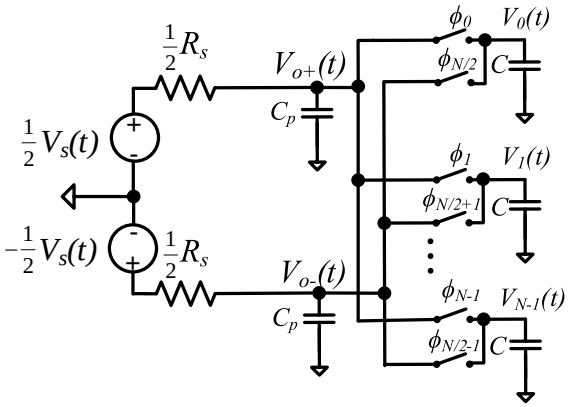

Figure 2.2: Differential band-pass N-path filter

Several works have used the concept of N-path filtering [23] for implementing high-linearity receivers. By mixing the input down to DC, filtering with a simple low pass filter, and subsequently upconverting back to RF, a high-Q band-pass filter is obtained with clock-tunable center frequency. Implementing the filter with only passive components, for example, using commutating capacitors as shown in Fig. 2.2, ensures high linearity [15, 16], but only gives second order band-pass filtering at RF. Cascading such N-path filters using active

stages results in an overall higher-order filter, but impedance matching and reduced linearity are concerns. For example, [18] implements a 6^{th} order band-pass filter in this manner as shown in Fig. 2.3. In [14] N-path filtering is used with DT-IIR filtering to achieve higher-order filters while impedance matching is ensured with a programmable switched-capacitor resistance. It uses only passive components for high linearity, but at the cost of NF.

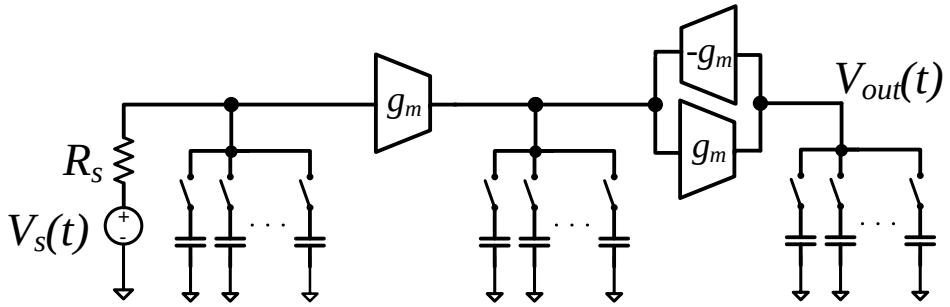

Figure 2.3: Higher-order N-path filtering by cascading

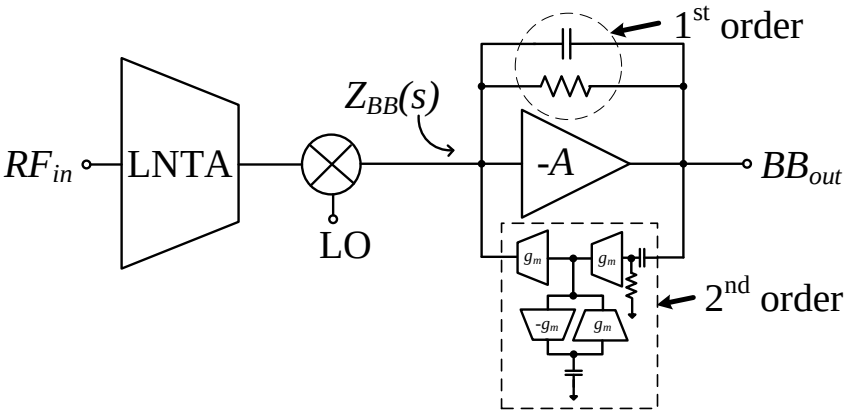

Figure 2.4: Mixer-first receivers

An alternative approach to apply N-path filtering is the popular mixer-first receiver topology. High linearity is achieved by eliminating the LNA, and placing the antenna at the input of a passive mixer. The baseband low-pass section of the mixer gets upconverted to RF to give a high-Q band-pass filter. LO programmable matching is also possible with a resistive component in the baseband [19], but the band-pass filter is only second order with a passive first order low-pass baseband, while NF is also high. Higher order baseband filtering [22] is possible as shown in Fig. 2.4, but with lower linearity due to the use of active

components. A recent work [21] instead uses the mixer resistance to achieve a broadband match, while keeping the baseband in feedback for high linearity. As shown in Fig. 2.5, a noise cancelling current-driven path was also added for low NF, but overall linearity is high for only far-out blockers due to first order baseband filtering.

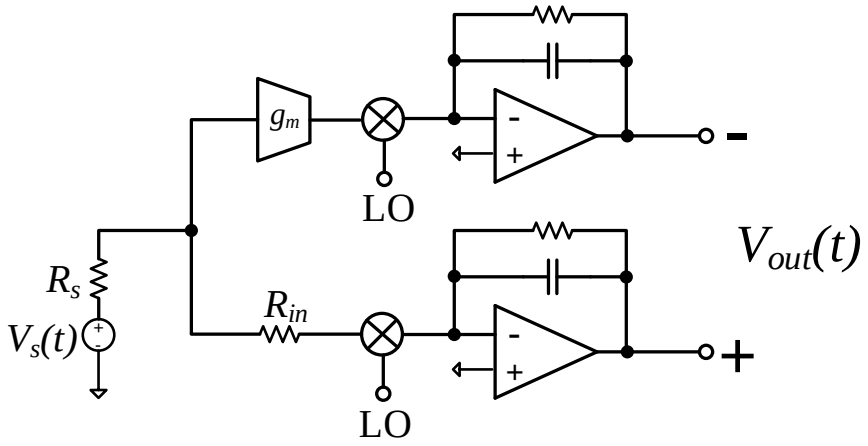

Figure 2.5: Noise-cancelling mixer-first receiver

In this work, we applied a new approach to achieve programmable receiver front-ends that achieves sharp filtering, while maintaining linearity in the presence of large close-in blockers. It uses the recent concept of Filtering by Aliasing (FA) [8]. First demonstrated using a passive filter circuit [24], the technique uses a sampled linear, periodically time-varying (LPTV) circuit to realize an effective sharp LTI filter from the input to the sampled output. While the passive filter achieves sharp programmable filtering, with high linearity and low power, it has a high noise figure and cannot be matched easily to the antenna interface. Instead, we use an integrate-and-dump circuit along with a time-varying resistor to apply the FA technique, which allows for impedance matching, sharp filtering and high linearity while improving the noise performance as well.

2.3 The Filtering by Aliasing Concept

It is well known sampling a continuous-time (CT) signal leads to undesirable aliasing. For a sampling rate of F_s, signal content in frequencies beyond $F_s/2$ will alias into the wanted

frequency range in the Nyquist band (frequencies below $F_s/2$). Traditionally, sufficient anti-alias filtering is needed beyond $F_s/2$ to prevent this effect. However, aliasing is a deterministic effect and so its effects can be described precisely. This realization has led to the development of a recent anti-alias filtering technique known as "Filtering by Aliasing" (FA).

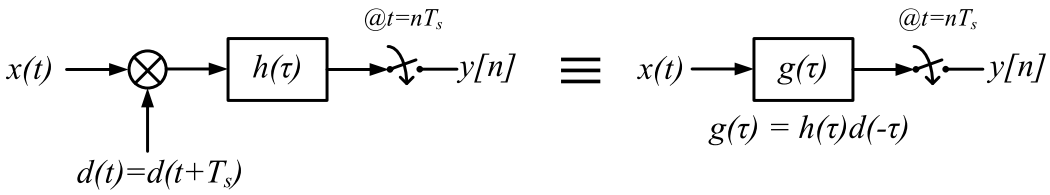

Figure 2.6: Block diagram of a Filtering by Aliasing system, and the realized apparent LTI anti-aliasing filter

FA utilizes LPTV circuits to incorporate aliasing into the realization of sharp anti-alias filtering. A simple block diagram of the technique is shown in Fig. 2.6, which consists of a simple filter, $h(\tau)$, whose output is sampled with a sampling period, T_s. When the input to this filter is first multiplied with a periodic "spreading" signal, $d(t)$, whose period is T_s, then it can be shown that the system is equivalent to the input being passed through an apparent LTI filter, $g(\tau) = h(\tau)d(-\tau)$, before sampling. The key result is that given a filter $h(\tau)$, the anti-alias filter, $g(\tau)$, can be designed based on the choice of $d(t)$. Further, the multiplication of the input with a periodic $d(t)$ makes the system LPTV with respect to the input, $x(t)$.

To further illustrate the technique, consider the example shown in Fig. 2.7. The input, $x(t)$, is multiplied by $d(t)$, and so its spectrum, $X(f)$, is spread in the frequency domain due to the convolution with $D(f)$ and is subsequently filtered by $H(f)$. $D(f)$ is precisely designed considering the filter $H(f)$ so that the unwanted frequency bands in the system (occupied by blockers) are filtered away. On sampling the spread and filtered copies of the unwanted frequency bands in the input are suppressed, while the wanted band remains. Hence, filtering by aliasing!

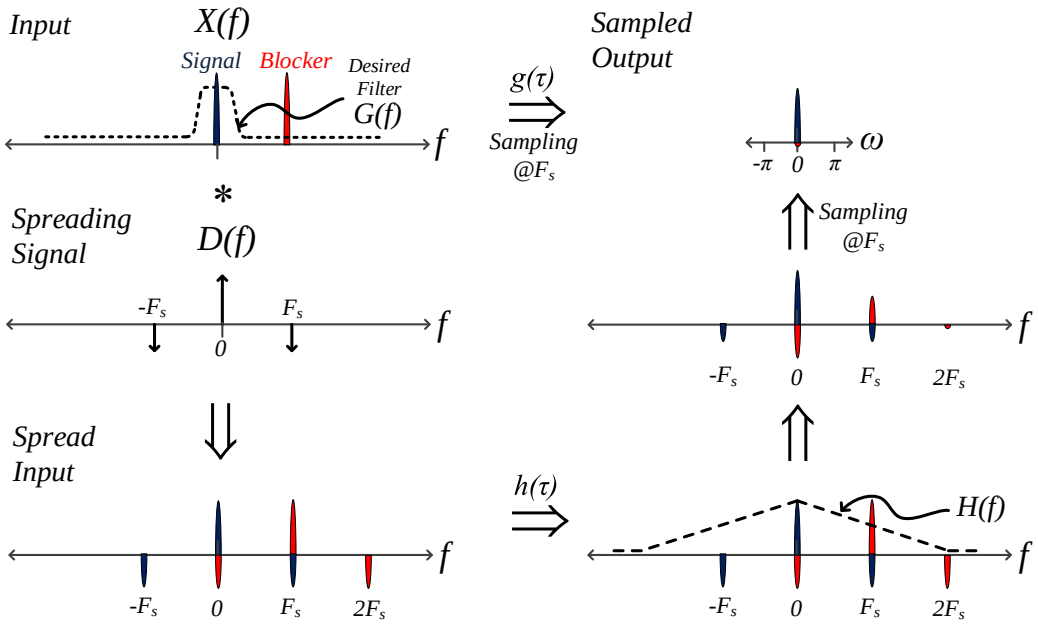

Figure 2.7: Frequency-domain view of the FA system based on an example input spectrum, $X(f)$ and filter $H(f)$

2.4 Receiver Topology

Consider the circuit shown in Fig. 2.8. While similar to the highly linear (baseband) main path of the receiver in [21] due to the feedback-based topology, the FA technique can be applied to give rise to sharp programmable filtering. The input resistor is varied periodically, while the output is sampled, both with a period of T_s to realize an FA system. It can be seen on inspection that

$$d(t) = \frac{1}{R_s + R_{in}(t)}, \quad h(\tau) = \frac{1}{C} \exp\left(-\frac{\tau}{RC}\right) u(\tau) \tag{2.1}$$

(where $u(\tau)$ is the unit-step function), and so the effective impulse response, $g(\tau)$, obtained is given by

$$g(\tau) = d(-\tau)h(\tau) = \frac{1}{C\left[R_s + R_{in}(-\tau)\right]} u(\tau). \tag{2.2}$$

To design the filter, $d(t)$ and hence $R_{in}(t)$ must be chosen appropriately. As described in

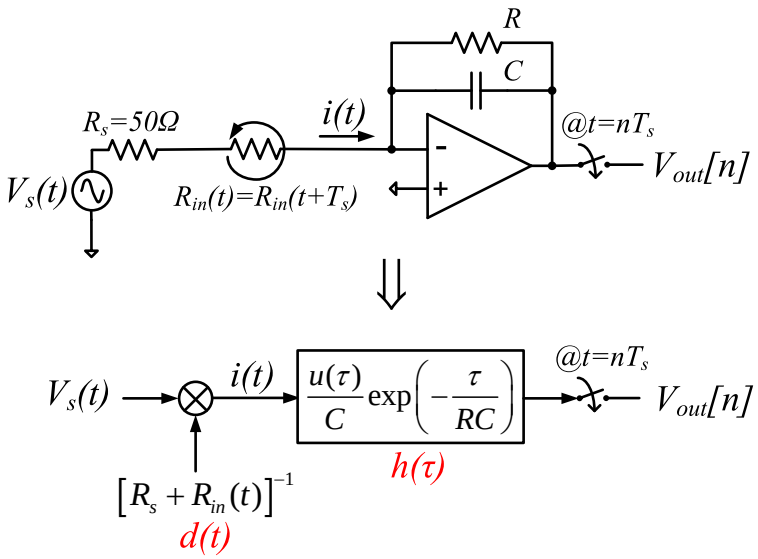

Figure 2.8: FA applied to the main-path of the noise cancelling mixer-first receiver [21]

[8], one method is to discretize the system at a high oversampling rate, $F_{ck} = 1/T_{ck}$, where $F_{ck}/F_s = N \gg 1$. In that case, $R_{in}(t)$ can be replaced by its oversampled version $R_{in}[\eta] = R_{in}[\eta + N] = R_{in}(\eta T_s)$. Hence $d(t)$ can be replaced by $d[\eta] = d[\eta + N] = 1/\left(R_s + R_{in}[\eta]\right)$, while $h(\tau)$ can be replaced by its discrete-time equivalent $h[\eta] = \alpha^\eta u[\eta] T_{ck}/C$, where $\alpha = \exp\left(-\frac{T_{ck}}{RC}\right)$ (obtained using impulse invariance). This corresponds exactly to the case of a single-pole $h(\tau)$ described in [8], and so the frequency response of the discrete-time effective filter $g[\eta] = d[-\eta]h[\eta]$ is given by

$$G(e^{j\omega}) = \frac{T_{ck}}{C} \frac{\sum_{\eta=0}^{N-1} d[-\eta]\alpha^\eta \exp(-j\omega\eta)}{1 - \alpha^N \exp(-j\omega N)}. \tag{2.3}$$

Examining the expression of $G(e^{j\omega})$ shows that it contains an N-tap FIR portion controlled by the sequence $d[\eta]$ (represented by the numerator), and an IIR portion depending only on α, that exists due to the single-pole filter, $h(\tau)$. In continuous time, this simply represents an FIR filter of length T_s controlled by $d(t)$ followed by the filter $H(f)$. To further simplify $G(e^{j\omega})$, we can let $\alpha \to 1$, i.e., let $R \to \infty$. Hence, the op-amp is configured as an integrator. However, this means that the filter has infinite gain at DC (represented by the pole moving to $\omega = 0$). This can be avoided by simply resetting the integrator after ev-

ery sampling instant, i.e., configuring the op-amp as an integrate-and-dump circuit instead. Hence, the final circuit is configured as shown in Fig. 2.9. Now the output samples can be derived on inspection as exactly

$$V_{out}[n] = \int_{t=(n-1)T_s}^{nT_s} \frac{V_s(t)}{C\left[R_s + R_{in}(t)\right]} dt, \tag{2.4}$$

and so the effective impulse response, $g(\tau)$, is obtained as

$$g(\tau) = \frac{1}{C\left[R_s + R_{in}(-\tau)\right]}, \ 0 \leq \tau < T_s, \tag{2.5}$$

i.e., an analog FIR filter of length T_s controlled entirely by the periodic signal $d(t) = 1/\left[R_s + R_{in}(t)\right]$.

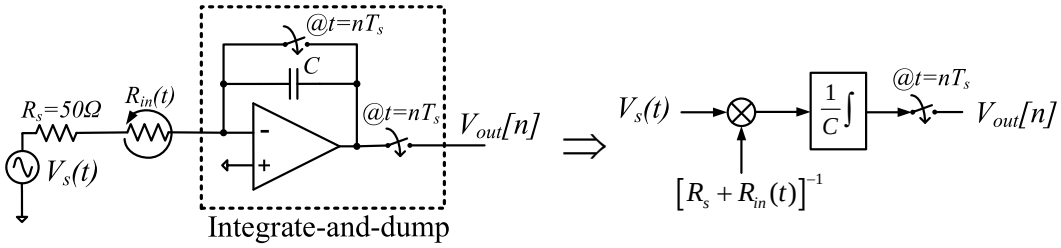

Figure 2.9: Simplified circuit for applying FA based on an integrate-and-dump block

2.5 Receiver Front-End Design Parameters

2.5.1 Filter Design and Optimization

The FIR filter described by (2.5) can be chosen to be any desired window function to achieve filtering. For example, setting $R_{in}(t) = R_s$ (for perfect impedance matching) realizes a rectangular window of length T_s given by

$$g_{rect}(\tau) = \frac{1}{2CR_s}, \ 0 \leq \tau < T_s. \tag{2.6}$$

Any other desired non-negative window of length T_s (for example, triangular, Hann, Hamming, Kaiser, etc.) can also be realized by setting $R_{in}(t)$ appropriately. Alternatively, $g(\tau)$ can be designed using any conventional digital FIR filter design technique. This can be done based on the oversampled discrete-time effective equivalent obtained in (2.3) that simplifies to the following for the circuit in Fig. 2.9 (since $\alpha \to 1$):

$$G(e^{j\omega}) = \frac{T_{ck}}{C} \sum_{\eta=0}^{N-1} d[-\eta] \exp(-j\omega\eta). \tag{2.7}$$

The frequency response in (2.7) can be treated as design of an N-tap FIR filter design problem, and techniques such as the Parks-McClellan algorithm, convex optimization, etc. can be used. In this work, we utilize linear programming to generate the coefficients $d[\eta]$ such that they satisfy constraints on the filter magnitude response, $|G(e^{j\omega})|$. The parameters in the optimization are the filter's pass-band edge frequency, F_{pass} (typically set to $F_s/2$) and stop-band edge frequency, F_{stop}. These map to $\omega_{pass} = F_{pass}/(2\pi F_{ck})$ and $\omega_{stop} = F_{stop}/(2\pi F_{ck})$ in the discrete-time filter design problem. The constraints in the optimization are typical of design of low-pass digital FIR filters, where the goal is to minimize the stop-band gain, δ_{stop} (or maximize stop-band suppression $A_{stop} = 1/\delta_{stop}$), subject to the constraints:

$$\begin{aligned} G_0(1-\delta_{pass}) \le |G(e^{j\omega})| \le G_0, \quad & \omega \in [0, \omega_{pass}] \\ |G(e^{j\omega})| \le G_0\delta_{stop}, \quad & \omega \in [\omega_{stop}, \pi], \end{aligned}$$

where δ_{pass} is the pass-band loss/ripple (typically set to 3dB) and G_0 is the (arbitrary) pass-band gain. In addition, other constraints are $d[\eta] \ge 0$ (since $R_{in}[\eta] \ge 0$), and $d[\eta] = d[N-\eta]$ (to obtain minimum phase FIR filters). Once the optimization generates the coefficients, $\{d[\eta]\}$, the time-varying resistance values, $\{R_{in}[\eta]\}$, are obtained using (2.5).

Figure 2.10 shows an example filter impulse and magnitude responses (and the corresponding resistance variation) obtained for F_s =5MHz, F_{pass} =2.5MHz, and F_{stop} =12.5MHz. The obtained filter is clearly much sharper than the reference 1^{st} order LTI filter obtained in works such as [19, 21]. Note that the choice of $F_{ck}(= NF_s)$ does not affect the obtained

A_{stop}, as long as F_{ck} is sufficiently greater than F_{stop}. However, in practice the resistance variation, $R_{in}(t)$, is implemented as a sampled-and-held version of the sequence, $R_{in}[\eta]$, at the clock rate, F_{ck}. Hence the obtained continuous-time impulse response, $g(\tau)$, is also sampled-and-held at the rate, F_{ck}. Thus, it's frequency response is given by

$$G(f) = \frac{1}{T_{ck}} G\left(e^{j2\pi f T_{ck}}\right) \operatorname{sinc}\left(f T_{ck}\right). \tag{2.8}$$

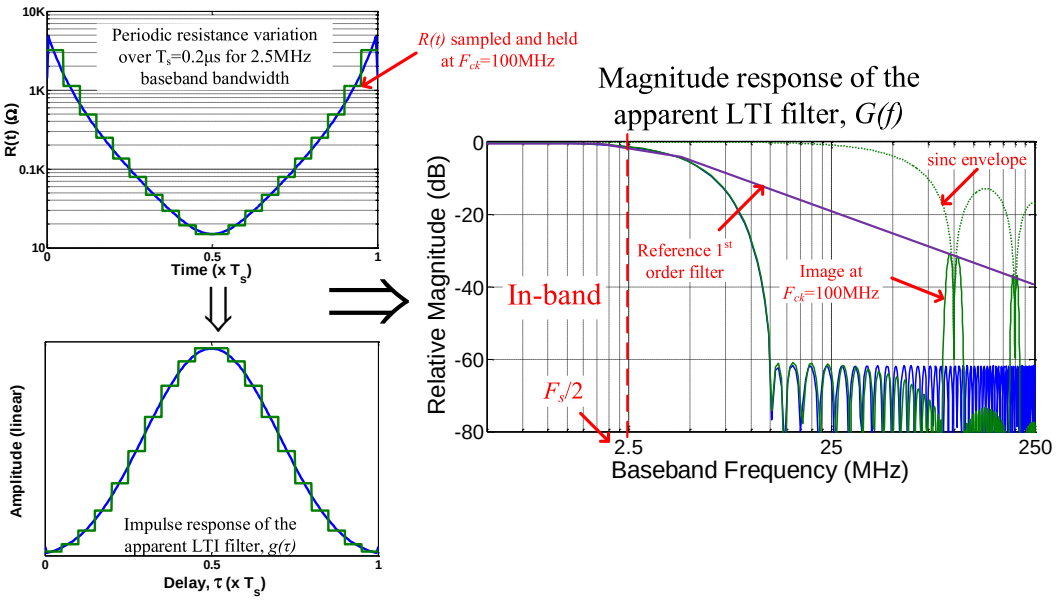

Figure 2.10: Example resistance variation, $R_{in}(t)$, and the corresponding impulse response, $g(\tau)$, and magnitude response, $G(f)$ shown for the case of (1) blue: oversampling factor, $N \to \infty$, and (2) green: $N = 20$

This leads to the images of the filter pass-band appear every F_{ck}, but filtered by the nulls of the sinc due to sample-and-hold operation (as seen in Fig. 2.10 for the case of a low N=20). The worst-case image power is around $f = F_{ck} - F_{pass}$, with a suppression of about $(1 - \delta_{pass}) \operatorname{sinc}(1 - F_{pass} T_{ck})$, where F_{pass} is the pass-band bandwidth, and δ_{pass} is the pass-band ripple. For typical values of $1 - \delta_{pass} \approx -3dB$, and $F_{pass} = F_s/2$, the image suppression is plotted versus oversampling rate in Fig. 2.11. F_{ck} should hence be chosen such that the suppression $\approx A_{stop}$. For A_{stop} of 50dB, an oversampling factor of 100 is sufficient.

Another important factor that determines the actual filter shape and A_{stop} achieved is

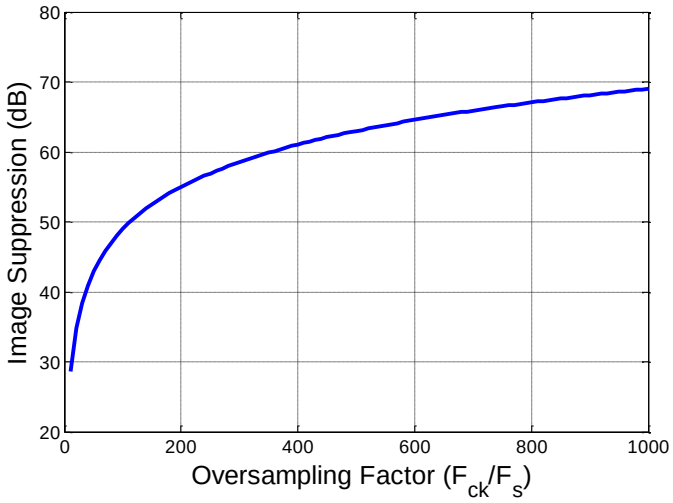

Figure 2.11: Worst case image suppression vs. oversampling factor, $N = F_{ck}/F_s$

the precision of the resistance variation, $R_{in}(t)$. In a practical implementation, $R_{in}(t)$ is quantized. Figure 2.12 shows the effects of quantization on the filter magnitude response, when $R_{in}(t)$ is implemented as a binary-scaled RDAC with a minimum resistance of 16Ω and an additional 11Ω of constant series resistance added due to op-amp input impedance and mixer switch resistance (similar to this work). It can be noted that about 8 bits of accuracy is required to guarantee higher than 50dB of A_{stop}.

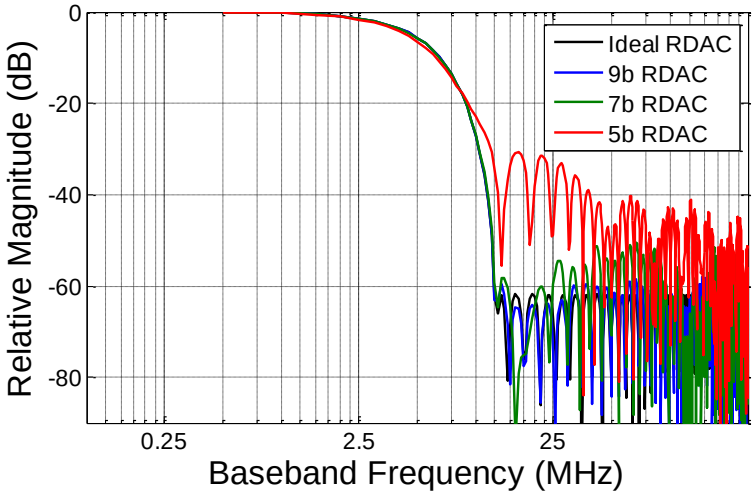

Figure 2.12: Achieved filter magnitude response vs. accuracy of resistance variation, $R_{in}(t)$

Finally, to obtain filtering at RF, an N-path passive mixer (not the same as the oversampling factor, $N = F_{ck}/F_s$) can be incorporated into to upconvert the baseband filter to any

LO frequency as shown in Fig. 2.13 (similar to mixer-first receivers such as [19, 20, 21, 22]). This work utilizes 4-path mixers driven by 25% duty-cycle LO waveforms to achieve band-pass filters with both in-phase and quadrature-phase outputs.

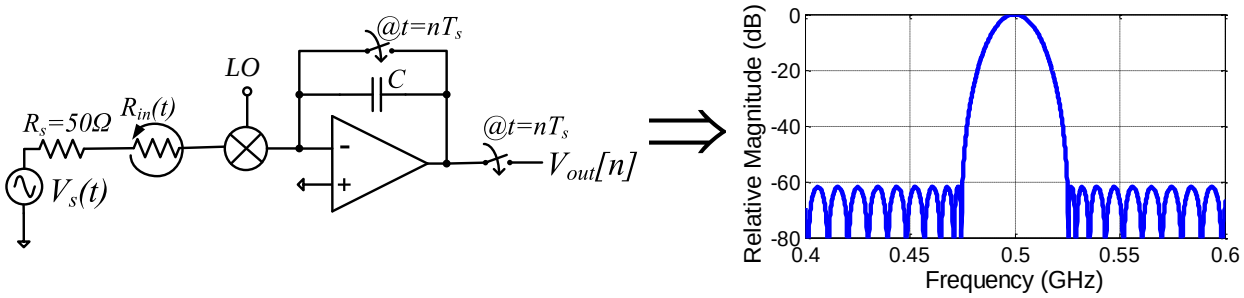

Figure 2.13: Band-pass filtering by incorporating a passive mixer into the baseband filter in Fig. 2.9

2.5.2 Impedance Matching

An important consideration for receiver front-ends is to achieve impedance matching with the antenna impedance, R_s, that is typically 50Ω. A good match is conventionally expressed as achieving an S_{11} < -10dB throughout the received channel. To achieve this, it is essential to derive the S_{11} for the proposed receiver front-end. For the circuit in Fig. 2.13, the input impedance at any time instant is simply given the time-varying resistance, $R_{in}(t)$ (which should include the op-amp input impedance and series impedances, such as mixer switch resistance) that is a memory-less resistance. Hence in steady-state, the instantaneous ratio between the incident wave, $V_I(t)$, and reflected wave, $V_R(t)$, is given by

$$\Gamma(t) = \frac{V_R(t)}{V_I(t)} = \frac{R_{in}(t) - R_s}{R_{in}(t) + R_s}. \tag{2.9}$$

Note that since $R_{in}(t)$ is periodic with period T_s, $\Gamma(t)$ is also periodic, and hence it's Fourier transform, $\Gamma(f)$, consists of tones at F_s and its harmonics (as shown in Fig. 2.14). To calculate S_{11} at a frequency of f_0, the incident wave is a sinusoid at f_0 denoted as $V_I(t) = \exp(j2\pi f_0 t)$. Then the reflected wave is simply given by $V_R(t) = \Gamma(t)\exp(j2\pi f_0 t)$. Then the frequency spectrum of the reflected waveform, $V_R(f)$ is given by the spectrum of

the incident waveform, $V_I(f)$, convolved with $\Gamma(f)$ as shown in Fig. 2.14). Then the S_{11} at frequency f_0 is given by

$$S_{11}(f_0) = \frac{V_R(f_0)}{V_I(f_0)} = \Gamma(f=0) = mean\left(\frac{R_{in}(t) - R_s}{R_{in}(t) + R_s}\right). \tag{2.10}$$

Hence the S_{11} simply depends upon the mean value of $\Gamma(t)$. Note that it is also frequency independent due to the fact that the input impedance, while time-varying, is still memoryless, and hence the impedance match is wideband.

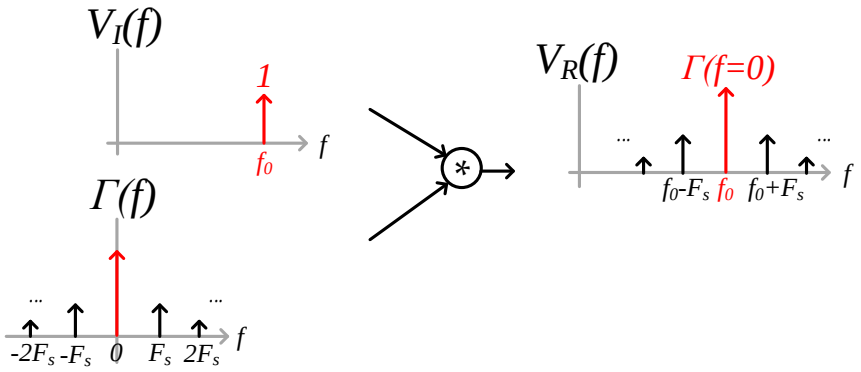

Figure 2.14: Fourier transforms of the incident and reflected waveform for a single-tone incident voltage waveform

To achieve good impedance match, an additional S_{11} constraint needs to be added to the filter optimization routine. Hence, S_{11} needs to be related to the filter impulse response, $g(\tau)$. By manipulating (2.10) using (2.5), it can be shown that

$$S_{11} = 1 - (2R_sC)\, mean\left[g(\tau)\right], \;\; 0 \le \tau < T_s. \tag{2.11}$$

(2.11) can be further simplified by normalizing $g(\tau)$ to the impedance matched rectangular window from (2.6) to

$$S_{11} = 1 - mean\left[g_{norm}(\tau)\right], \;\; 0 \le \tau < T_s, \tag{2.12}$$

where $g_{norm}(\tau) = g(\tau)/g_{rect}(\tau) = 2R_s/\left[R_s + R_{in}(-\tau)\right]$, with $g_{norm}(\tau) = 1$ being the trivial LTI case for perfect matching. In fact, any window function can be used to realize a perfect

matched filter, $g(\tau)$, as long as its DC gain is scaled to give S_{11}=0 according to (2.11), i.e., $\int_0^{T_s} g(\tau)\,dt = T_s/(2R_sC)$ or $\int_0^{T_s} g_{norm}(\tau)\,dt = T_s$. For example, a triangular window given by

$$g_{trng}(\tau) = \left[1 - \left|\frac{T_s - 2\tau}{T_s}\right|\right] \frac{1}{R_sC},\ 0 \le \tau < T_s \tag{2.13}$$

will give $S_{11} = 0$. Further, it can be verified that any linear combination $(1-\alpha)g_{rect}(\tau) + \alpha g_{trng}(\tau)$ will still be perfectly matched.

There seems to be no downside to impedance matching according to (2.11) and (2.12). However, in an actual implementation there is a minimum value realizable for the resistance variation, $R_{in}(t)$. This minimum value, R_{min}, while ideally 0, is usually set by design constraints such as area/power related to the realization of $R_{in}(t)$. For example, R_{min} is limited by the input impedance presented by the integrator in Fig. 2.9. Further, $R_{in}(t) < \infty$, leading to the additional constraint:

$$0 < g_{norm}(\tau) \le \frac{2R_s}{R_s + R_{min}},\ 0 \le \tau < T_s. \tag{2.14}$$

This condition limits the range of filters that can be attained. For example, for the filter$(1-\alpha)g_{rect}(\tau)+\alpha g_{trng}(\tau)$, (2.14) implies that $|\alpha| \le \frac{R_s - R_{min}}{R_s + R_{min}}$. Note that higher α implies higher side-lobe suppression. For example, $\alpha = 1$ gives a triangular window, but requires $R_{min} = 0$. It must also be noted that $R_{min} < R_s$ for achieving $S_{11} = 0$. A similar limitation on side-lobe suppression with impedance matching can be shown for other windows as well. For example, consider the Kaiser window [25] of length T_s given by

$$g_{kaiser}(\tau) = \frac{I_0\left[\alpha\sqrt{1 - \{(\tau - 0.5T_s)/0.5T_s\}^2}\right]}{I_0[\alpha]},\ 0 \le \tau < T_s,$$

where $I_0(.)$ is the zeroth-order modified Bessel function of the first kind, and the parameter α is used to vary the window side-lobe suppression (higher α for more suppression). As shown in Fig. 2.15, the achieved maximum α and side-lobe suppression depend entirely on R_{min}. Hence there is a clear trade-off between R_{min} and the filter suppression achieved with impedance matching.

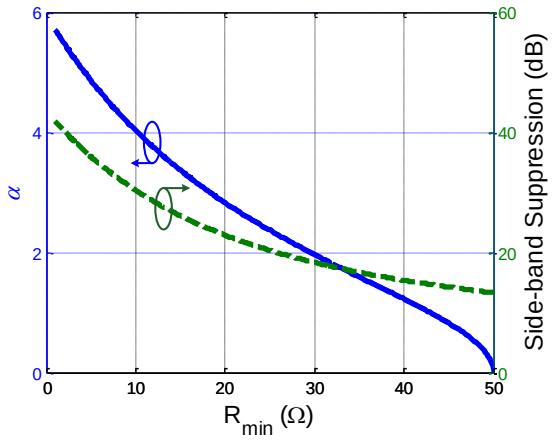

Figure 2.15: Trade-off between R_{min} and maximum α (and side-lobe suppression) when $g(\tau)$ is implemented using Kaiser window with $S_{11} = 0$

In the general filter design problem, an additional constraint $|S_{11}| \leq \beta$ can be added using (2.12), where β is the desired S_{11}, while satisfying (2.14). These two constraints can be combined to give the constraint:

$$\left|1 - \frac{2R_s}{R_s + R_{min}} mean\left[g_{norm}^{max}(\tau)\right]\right| \leq \beta, \;\; 0 \leq \tau < T_s, \tag{2.15}$$

where $g_{norm}^{max}(\tau) = g(\tau)/g_{max} = [R_s + R_{min}]/[R_s + R_{in}(-\tau)]$, and g_{max} is the peak value achievable by $g(\tau)$, i.e., $g_{max} = 1/C(R_s + R_{min})$. The S_{11} constraint essentially restricts the range of variation of the impulse response, or equivalently the resistance variation, $R_{in}(t)$. For example, Fig. 2.16 shows the resistance variation obtained with and without the additional constraint for S_{11} of -20dB for R_s=50Ω, and R_{min}=27Ω (similar to the implementation in this work). The matched case clearly has lower resistance variation, and hence sacrifices A_{stop} to achieve the desired S_{11}.

Figure 2.17 shows the variation A_{stop} achieved with required S_{11} for various transition bandwidths of $K = F_{stop}/F_{pass}$, with $F_{pass} = F_s/2$, $R_s = 50\Omega$, and $R_{min} = 27\Omega$ (similar to the implementation in this work). While A_{stop} does improve with increasing transition bandwidths, it can be seen that the improvement is far less compared to the unmatched case (corresponding to the point with worst S_{11} in each curve). The variation of A_{stop} achieved while varying R_{min} is also shown in Fig. 2.17 for $K = 5$ and S_{11}=-20dB.

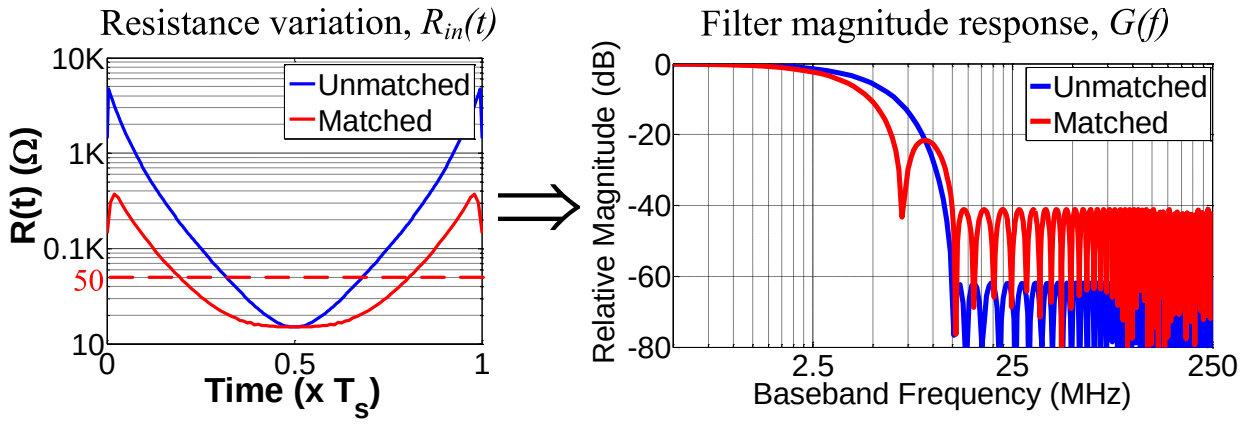

Figure 2.16: Example resistance variation and filter magnitude response obtained with an S_{11} requirement of -20dB

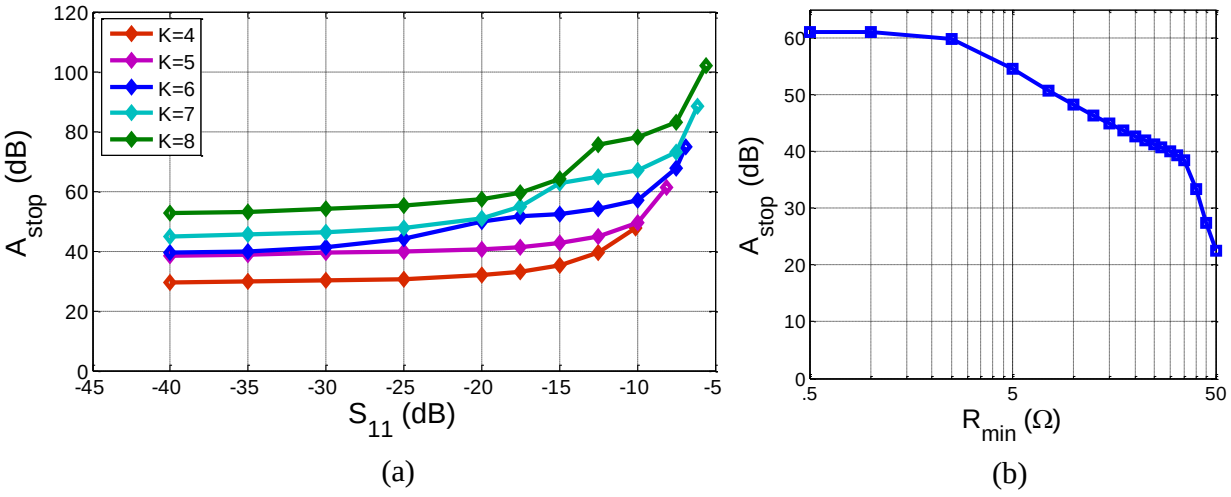

Figure 2.17: (a) Achieved filter stop-band suppression, A_{stop} vs. S_{11} required, (b) A_{stop} vs. R_{min} for $K = 5$ and S_{11}=-20dB

2.5.3 Noise Figure

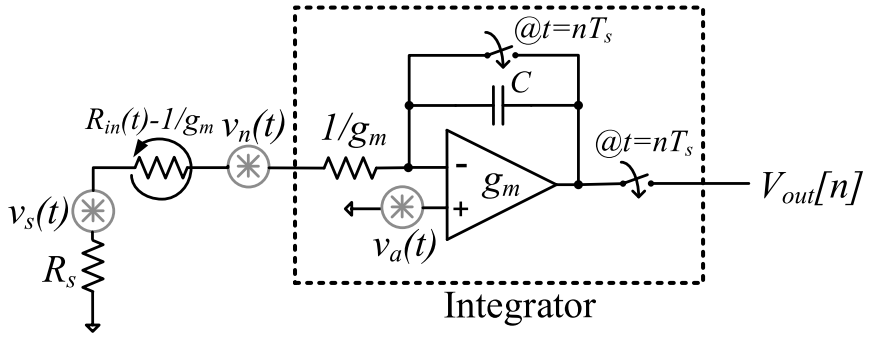

Figure 2.18: Equivalent circuit of baseband for noise analysis

The noise performance of the receiver's baseband equivalent circuit can be analyzed based on the circuit shown in Fig. 2.18. The op-amp is considered to be a simple g_m stage with input-referred noise voltage $v_a(t)$, while the noise sources corresponding to the source, R_s, and time-varying resistance, $R_{in}(t) - 1/g_m$, are $v_s(t)$ and $v_n(t)$ respectively. Note that the input-impedance of the op-amp, $1/g_m$, is separated from the controlled resistance variation, $R_{in}(t)$ for simplifying the noise expressions. The noise sources are considered white and Gaussian with autocorrelations:

$$\begin{aligned} R_{ss}(t,\tau) &= E\left[v_s(t)v_s(t+\tau)\right] = 2kTR_s\delta(\tau), \\ R_{aa}(t,\tau) &= E\left[v_a(t)v_a(t+\tau)\right] = 2kT\tfrac{\gamma}{g_m}\delta(\tau), \\ R_{nn}(t,\tau) &= E\left[v_n(t)v_n(t+\tau)\right] = 2kT\left[R_{in}(t) - g_m^{-1}\right]\delta(\tau), \end{aligned} \tag{2.16}$$

where k is the Boltzmann constant, and T is the temperature in Kelvin. Using superposition, the output voltage due to the current integrated on the capacitor can be obtained as

$$V_{out}[n] = \int_{t=(n-1)T_s}^{nT_s} \frac{V_s(t) + V_n(t) + V_a(t)}{C\left[R_s + R_{in}(t)\right]} dt. \tag{2.17}$$

From (2.17) and using (2.16), the variance of the output noise samples can be calculated to be

$$E\left[V_{out}^2[n]\right] = \frac{2kT}{C^2}\int_{t=(n-1)T_s}^{nT_s}\frac{R_s}{\left[R_s+R_{in}(t)\right]^2}dt+ \frac{2kT\gamma}{C^2}\int_{t=(n-1)T_s}^{nT_s}\frac{g_m^{-1}}{\left[R_s+R_{in}(t)\right]^2}dt+ \frac{2kT}{C^2}\int_{t=(n-1)T_s}^{nT_s}\frac{R_{in}(t)-g_m^{-1}}{\left[R_s+R_{in}(t)\right]^2}dt, \tag{2.18}$$

where the first term corresponds to noise from R_s, the second to noise from the op-amp, and the last to the noise from $R_{in}(t)-1/g_m$. Note that since $R_{in}(t)$ is periodic with period T_s, the variance is constant. It can also be shown using (2.16) and (2.17) that $E\left[V_{out}[m]V_{out}[n]\right] = 0$ for $m \neq n$, i.e., the output noise density is also white. This is intuitively obvious since the noise contribution to each output sample is from independent samples of the noise sources (the only memory in the system is due to the load capacitor that is reset after every sample).

Since the output noise is white, the relative noise contribution of each noise source with respect to R_s can be calculated by simply dividing the entire expression in (2.18) with the first term, thus giving the noise factor, F:

$$F = 1 + \frac{\gamma}{g_m R_s} + \frac{mean\left[\left(R_{in}(t) - g_m^{-1}\right)/\left(R_s + R_{in}(t)\right)^2\right]}{R_s mean\left[1/\left(R_s + R_{in}(t)\right)^2\right]}. \tag{2.19}$$

This expression can be further simplified for $\gamma = 1$ (short channel-length devices) and (2.12) to give

$$F = \frac{mean\left[1/\left(R_s + R_{in}(t)\right)\right]}{R_s mean\left[1/\left(R_s + R_{in}(t)\right)^2\right]} = 2\frac{mean\left[g_{norm}(\tau)\right]}{mean\left[g_{norm}^2(\tau)\right]},\ 0 \leq \tau < T_s. \tag{2.20}$$

While F captures the relative contributions of each noise source with respect to R_s, it is important to consider the contribution due to aliasing as well (since the output is sampled). Aliasing causes the noise factor due to R_s to be > 1 (unlike in a traditional receiver with a CT output), and so appears as a multiplicative factor on F in the total noise calculation. The multiplying factor can be calculated simply based on the total output noise of R_s and the magnitude response of the filter seen by R_s, i.e., (2.8). Hence for a baseband frequency of Δf, it is given by

$$F_{\text{aliasing}}(\Delta f) = \frac{\sum_{n=-\infty}^{\infty} |G(\Delta f + nF_s)|^2}{|G(\Delta f)|^2}, \ |\Delta f| \leq \frac{F_s}{2}. \tag{2.21}$$

Note that the numerator is the total noise contribution of R_s and so is independent of Δf (since it is white). Moreover, (2.21) can be easily computed for DC, since the numerator is simply the first term in (2.18), and the denominator is $2kTR_s|G(\Delta f = 0)|^2$ (the input noise power spectral density times the square of the DC gain). Using the DC gain of $G(\Delta f = 0) = \int_0^{T_s} \frac{dt}{C[R_s + R_{in}(t)]}$, it can be shown that

$$F_{\text{aliasing}}(\Delta f = 0) = \frac{mean\left[(R_s + R_{in}(t))^{-2}\right]}{\left\{mean\left[(R_s + R_{in}(t))^{-1}\right]\right\}^2} = \frac{mean\left[g_{norm}^2(\tau)\right]}{\left(mean\left[g_{norm}(\tau)\right]\right)^2}, \ 0 \leq \tau < T_s. \tag{2.22}$$

Since the numerator of (2.21) is constant, $F_{\text{aliasing}}(\Delta f) = \frac{|G(\Delta f=0)|^2}{|G(\Delta f)|^2} F_{\text{aliasing}}(\Delta f = 0)$, i.e., the additional degradation at baseband frequency, Δf, is simply given by the filter droop at Δf compared to DC. Hence, the total baseband noise factor, $F_{\text{baseband}}(\Delta f)$, is given by

$$F_{\text{baseband}}(\Delta f) = F \times F_{\text{aliasing}}(\Delta f) = \frac{|G(\Delta f = 0)|^2}{|G(\Delta f)|^2} \frac{2}{mean\left[g_{norm}(\tau)\right]}, \ 0 \leq \tau < T_s. \tag{2.23}$$

Further, using (2.12) it can be noted that (2.23) evaluates to

$$F_{\text{baseband}}(\Delta f = 0) = \frac{2}{1 - S_{11}}, \tag{2.24}$$

i.e., the baseband noise factor at DC is related to the achieved S_{11}. Moreover, in case of perfect matching $S_{11} = 0$, and so $F_{\text{baseband}} = 2$ at DC that is exactly the same as the LTI case, i.e., there is no degradation due to the time-varying resistance! Note that there is an additional degradation at other frequencies due to droop in the filter response. In an LTI front-end there is usually no additional degradation since the out-of-band noise is usually filtered-off by downstream stages.

Finally, when operated as a bandpass filter with a 4-path 25% duty-cycle mixer, the noise figure degradation due to LO harmonics has to be added as well as is given by [21]

$$F_{\text{harmonics}} = \text{sinc}^{-2}(1/4) \approx 0.91\text{dB}. \tag{2.25}$$

Thus, the total noise figure is given by

$$\begin{aligned} F_{\text{total}}(\Delta f)|_{\text{dB}} &= 10\log_{10}\left[F \times F_{\text{aliasing}}(\Delta f) \times F_{\text{harmonics}}\right] \\ &= F|_{\text{dB}} + F_{\text{aliasing}}(\Delta f)|_{\text{dB}} + F_{\text{harmonics}}|_{\text{dB}}, \end{aligned} \tag{2.26}$$

where $F_{\text{harmonics}}$ only appears with bandpass operation. Figure 2.19 shows the calculated noise figure of the impedance-matched filter shown in Fig. 2.16. It can be seen that $F|_{\text{dB}} =$ 2.75dB, $F_{\text{aliasing}}(\Delta f = 0)|_{\text{dB}} = 0.72$dB, and the average NF across frequencies is 5.2dB (the filter droop across the band is about 2.2dB). It can also be simply noted that $F|_{\text{dB}} + F_{\text{aliasing}}(\Delta f = 0)|_{\text{dB}}$ is very close to the 3dB obtained in case of LTI operation (due to S_{11} = -20dB = 0.1), and the only additional contributor to NF is simply from the noise aliasing due to sampling. While this is unavoidable, the noise degradation can be reduced by setting the sampling rate, F_s, such that the received signal single-sideband bandwidth is lower than, for example, $0.25F_s$, thus ensuring that $F_{\text{baseband}}(\Delta f)|_{\text{dB}} < 4$dB inside the signal band (as observed from Fig. 2.19). This does come at the cost of not filtering the adjacent band to the wanted signal.

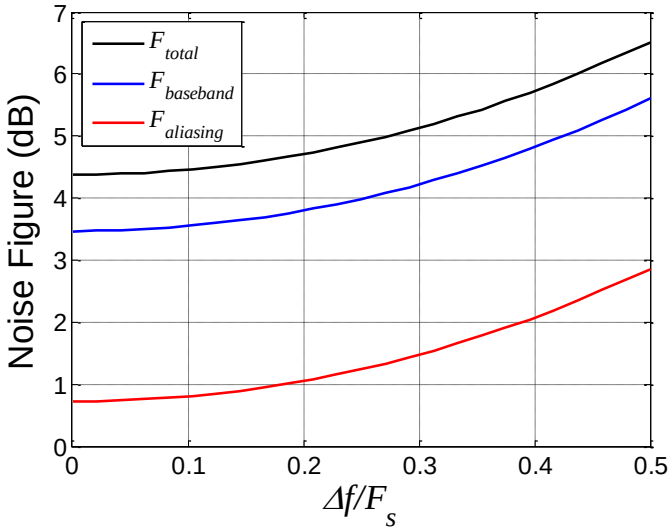

Figure 2.19: Calculated noise figure for the impedance matched filter shown in Fig. 2.16

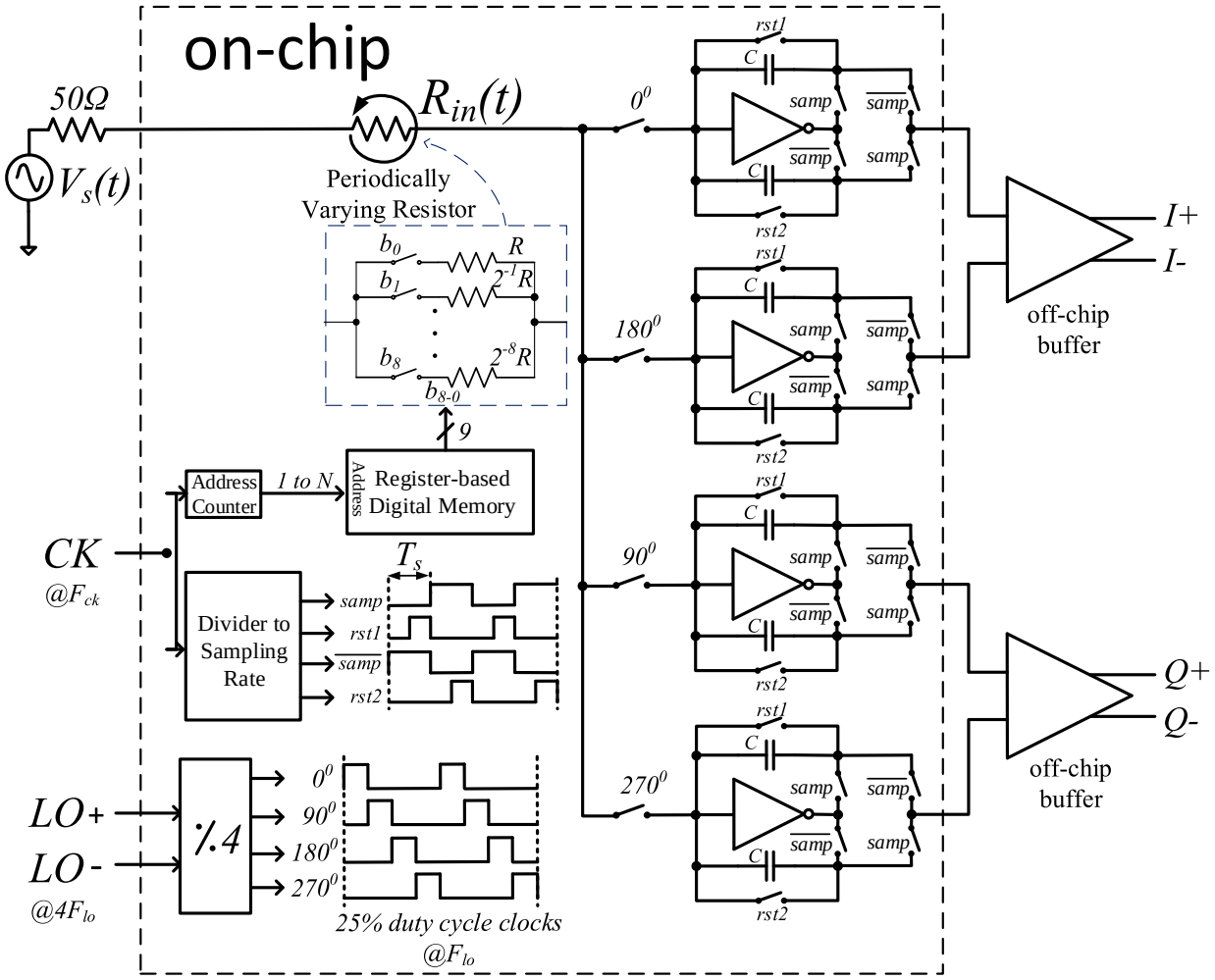

Figure 2.20: Block diagram of the implemented receiver front-end

2.6 Implementation and Non-Idealities

The block diagram of the implemented FA-based receiver front-end is shown in Fig. 2.20. The antenna input is connected to the LPTV resistor, $R_{in}(t)$, that is built as a 9-bit resistor DAC (RDAC). The RDAC control bits are periodic with the period, T_s, and are read out periodically from an on-chip register-based memory at the input clock rate, $F_{ck}(= NF_s)$. The RF current is mixed down to baseband with a 4-path 25% duty-cycle mixer switching at the LO frequency, F_{lo}. The mixer switches use transmission gates and have a resistance of about 3Ω. The base-band is composed of integrators with self-biased inverter-based op-amps whose sampling and reset clocks are generated by dividing F_{ck}.

2.6.1 Resistor DAC

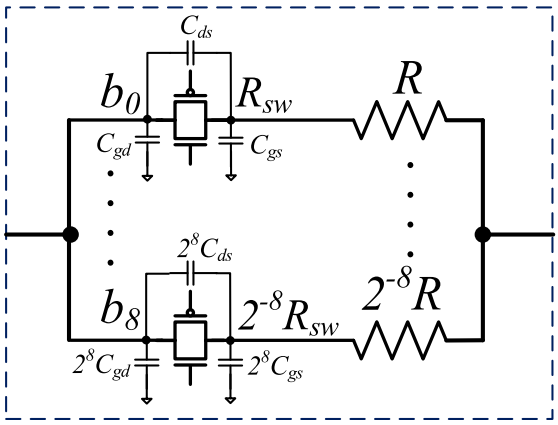

Figure 2.21: Schematic of the 9-bit resistor DAC with annotated switch parasitics

The heart of the receiver front-end is the 9-bit RDAC shown in Fig. 2.21. As shown, the RDAC is implemented in a binary-scaled fashion, with each branch consisting of an *rppoly* resistor in series with a transmission gate control switch. The minimum RDAC resistance was designed to be about 15.7Ω ($R_{sw} + R \approx 8\text{k}\Omega$). The output node of the RDAC is held at virtual ground due to the op-amp, and so the input swing is divided across the linear poly resistor and the non-linear control switch. Hence to maximize the out-of-band linearity of the circuit (when the op-amp outputs dont compress), the ratio of switch resistance, R_{sw}, to

the poly resistance, R has to be minimized. However, lower R_{sw} implies larger switches, and hence higher power consumption for driving them. Furthermore, the parasitic capacitances associated with switch transistors shown in Fig. 2.21 increase with size as well, and hence limit the filtering performance as well. To balance these effects, $R_{sw} : R$ was set to 1:4. The effect of the switch parasitics are considered below, and are similar to the passive LPTV scanner described in [24].

2.6.1.1 C_{ds} Capacitance

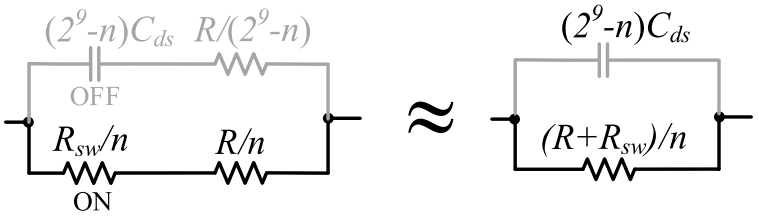

Figure 2.22: RDAC equivalent circuit with C_{ds} capacitance

C_{ds} is mainly present due to routing and so can be minimized to some level during layout. Figure 2.22 shows the effective circuit of the RDAC when set to a code of n with C_{ds} considered. The switches in the ON branches simply present an effective resistance of R_{sw}/n as shown, while those in the OFF branches instead produce an effective capacitance of $(2^9 - n)C_{ds}$. Since the corner frequency $1/2\pi RC_{ds} \gg F_{ck}$, the RDAC is effectively a resistance in parallel with a capacitance, with a code-dependent corner frequency. Moreover, the corner worsens for small n limiting RDAC dynamic range, and thus limits the filter suppression achieved. Fig. 2.23 shows the simulated effect of Cds on a 5MHz BW filter centered at 500MHz. In this work $(R + R_{sw})C_{ds} \approx 1.6$ps. Clearly the stop-band suppression, A_{stop} is limited due to the presence of C_{ds}.

2.6.1.2 C_{gs} and C_{gd} Capacitance

The C_{gs} and C_{gd} capacitances are mainly due to the switch transistors themselves. C_{gd} presents itself directly at the antenna and reduces gain (and worsens noise figure) at high

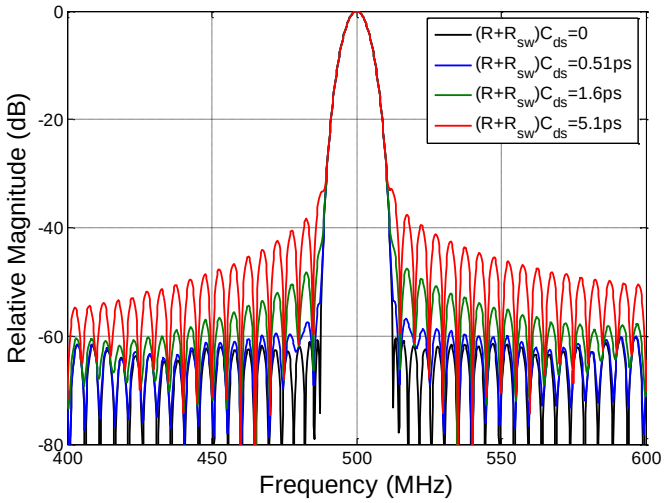

Figure 2.23: Simulated effect of C_{ds} capacitance on the filter magnitude response

LO frequencies, while degrading the S_{11} as well. The C_{gs} capacitances in the RDAC draws current from the source in a code-dependent manner. The simulated effects of both C_{gs} and C_{gd} on a 5MHz BW filter centered at 500MHz is shown in Fig. 2.24 with $C_{gs} = C_{gd}$. As can be seen, only the filter transition band is affected, and the effect is small compared to that of C_{ds} (unlike for the passive filter [24]). In this work, $R_{sw}C_{gs} \approx 3.2$ps. Note that $R_{sw}C_{gs}$ will scale with process.

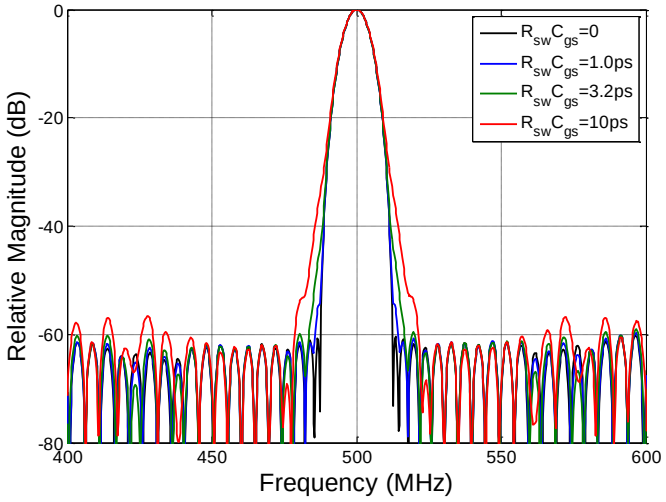

Figure 2.24: Simulated effect of C_{gs}/C_{gd} capacitance on the filter magnitude response

2.6.2 Baseband Integrators

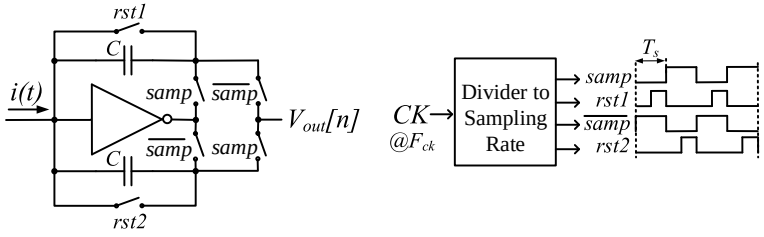

Figure 2.25: Schematic of the inverter-based baseband integrator and required clocks

The baseband integrators consist of simple inverter-based op-amps with tunable capacitor banks in feedback around them as shown in Fig. 2.25. Each capacitor bank is built as a ping-pong structure. This allows one capacitor to be connected across the op-amp, while the voltage stored on the other can read and reset using the clocks shown. The capacitor banks use MIM capacitors and are tunable from $20 - 140$pF to allow for a wide range of filter bandwidths, and their parasitics have no noticeable effect on performance. The op-amps themselves are self-biased due to the ping-pong action. Each op-amp consists of a PMOS and NMOS of length 180nm to increase gain to about 20dB and to reduce the flicker noise corner, and has a transconductance, g_m, of 125mS. The g_m is chosen to minimize noise figure contribution, as well as to minimize the minimum resistance achievable at the front-end, R_{min}, to aid in impedance-matching. The effects of op-amp non-idealities are considered below. For simplicity, finite gain and bandwidth are considered separately, since the former affects low frequency operation, while the latter affects high frequencies.

2.6.2.1 Finite Op-amp Gain

Figure 2.26 shows the case when the op-amp has an open-loop gain of A and the corresponding block diagram. The block diagram can be easily derived from the differential equation of the circuit obtained by applying KCL at the op-amp input (sign of the output is inverted for clarity):

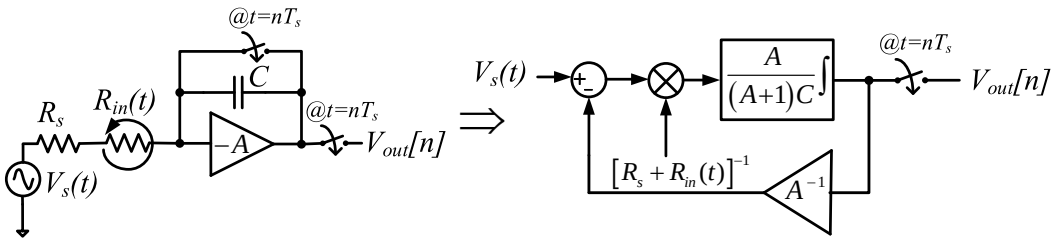

Figure 2.26: Equivalent circuit and block diagram for finite op-amp gain, A

$$\frac{V_s(t) - A^{-1}V_{out}(t)}{R_s + R_{in}(t)} = C\frac{d}{dt}\left[V_{out}(t) + \frac{V_{out}(t)}{A}\right]. \tag{2.27}$$

Alternatively, it can be easily understood as a passive RC circuit formed by the input resistance and a capacitance $(1 + A)C$ produced by Miller effect. Hence, the block diagram can be derived by starting with the one for the passive filter [24] and modifying it based on the presence of the op-amp at the output. From the block diagram, it is clear that the difference is that the feedback path (corresponding to integrator leakage) is attenuated by the op-amp gain compared to the fully passive case.

The equivalent filter impulse response can also be obtained by discretizing (2.27) similar to [24] and (2.3). Hence for every sampling period if we assume discretized input $V_s[\eta] = V_s(\eta T_{ck})$, output $V_{out}[\eta] = V_{out}(\eta T_{ck})$, and resistance variation, $R_{in}[\eta] = R_{in}(\eta T_{ck})$, (2.27) reduces to

$$V_{out}\left[\eta\right] = \alpha[-\eta]V_s\left[\eta\right] + \frac{(1 - \alpha[-\eta])}{A}V_{out}\left[\eta - 1\right], \tag{2.28}$$

where $\alpha[-\eta] = 1 - \exp\left(-\frac{A}{(1+A)}\frac{T_{ck}}{(R_s+R_{in}[\eta])C}\right) \approx \frac{A}{(1+A)}\frac{T_{ck}}{(R_s+R_{in}[\eta])C}$. Then using the fact that $V_{out}[0] = 0$ (due to integrator reset), the discretized apparent impulse response, $g[\eta]$ is given by

$$g[\eta] = \alpha[\eta]\prod_{k=0}^{\eta-1}\frac{(1 - \alpha[k])}{A},$$

with the corresponding frequency response given by

$$G(e^{j\omega}) = \sum_{\eta=0}^{N-1} g[\eta] \exp(-j\omega\eta),$$

where $N = T_s/T_{ck}$ is the oversampling factor. It is easy to see that compared to the passive case, the discharge term, $(1 - \alpha[k])$, is attennuated by the opamp gain, A, thus reducing its effect.

The simulated effect of op-amp gain is plotted in Fig. 2.27 for a 5MHz BW filter centered at 500MHz, with $C = 100$pF. The ideal gain of a single path in the 4-path bandpass circuit is about 10dB. Hence, the filter gain and shape degrades when op-amp gain reaches close to the ideal path gain. Nevertheless, the effect is small, and can be alleviated by increasing C to reduce filter gain.

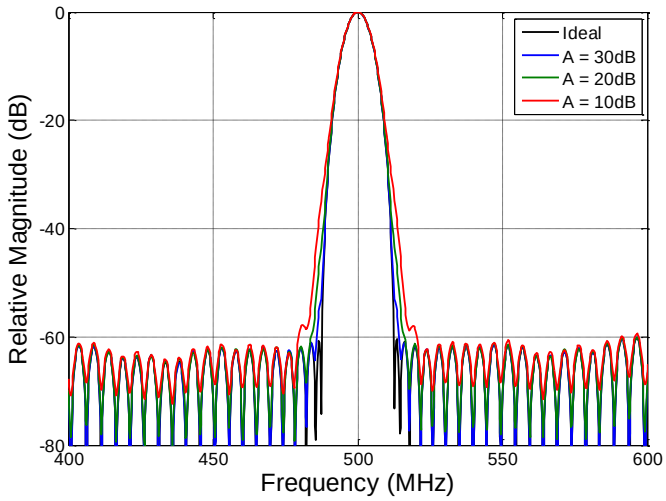

Figure 2.27: Simulated effect of finite op-amp gain, A, on the filter magnitude response

2.6.2.2 Finite Op-amp Bandwidth

The finite bandwidth of a single-stage op-amp in an integrator configuration can be represented by its g_m to give a bandwidth of g_m/C. In this configuration, the input impedance of the op-amp is given by $1/g_m$. Hence, by voltage division, the voltage at the opamp input is simply $v = g_m^{-1} V_s(t) / (R_s + R_{in}(t) + g_m^{-1})$. Thus the output voltage is simply given by the op-amp current, $g_m v$ integrating on the capacitor, and so (inverting the sign of the output

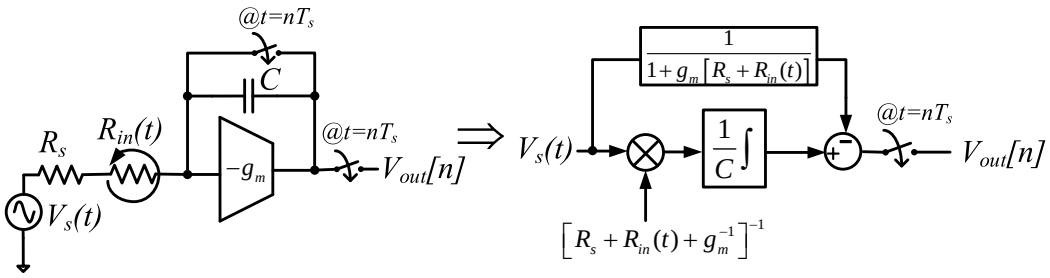

Figure 2.28: Equivalent circuit and block diagram for finite op-amp bandwidth, g_m/C

for clarity)

$$g_m v = \frac{d}{dt}\left[V_{out}(t) + v\right]$$

that reduces to the the block diagram shown in Fig. 2.28. Hence the output voltage samples are given by

$$V_{out}[n] = \int_{t=(n-1)T_s}^{nT_s} \frac{V_s(t)}{C\left[R_s + R_{in}(t) + g_m^{-1}\right]} dt - \frac{g_m^{-1} V_s(nT_s)}{\left[R_s + R_{in}(T_s) + g_m^{-1}\right]}. \tag{2.29}$$

From (2.29) it becomes clear that the op-amp input impedance ($1/g_m$) has to be included in the input resistance seen by the source while designing the filter impulse response.

Intuitively it is easy to see that the voltage division produces an ideal integration, since the op-amp current depends only on the input and flows completely through the capacitor. At high frequencies the capacitor reduces to a short and so the output voltage simply reduces to the op-amp input voltage, v. Thus, we get the equivalent block diagram with an ideal integrator, and an input-to-output leakage path due to the voltage divider at the input.

Note that the since the leakage path has no memory and the output is sampled, its value matters only at the sampling instant as shown in (2.29). Further, the filter impulse response depends only on $(R_s + R_{in}(t) + g_m^{-1})$, while the leakage path behaves like an all-pass filter with a gain of $\sim 1/g_m R_{in}(T_s)$. Since the gain of the desired FA filter is set by $1/C$, if $g_m R_{in}(T_s)/C$ is lower than A_{stop} of the desired filter (depending on the op-amp bandwidth g_m/C), then A_{stop} of the overall filter will be set by the all-pass leakage path.

The simulated effect of op-amp g_m is plotted in Fig. 2.29(a) for a 5MHz BW filter centered at 500MHz, with $C = 100$pF. Note that since the leakage also depends on $R_{in}(T_s)$, the filter design problem can be tweaked such that $R_{in}(T_s) \to \infty$, i.e., the filter is designed for $N-2$ taps, with $g[1] = g[N] = 0$ in (2.7). Figure 2.29(b) shows the simulated effect of this change. Clearly, the effect of low g_m is alleviated. Alternatively, if the voltage across the capacitor is measured as the final sampled output, then the leakage path does not appear.

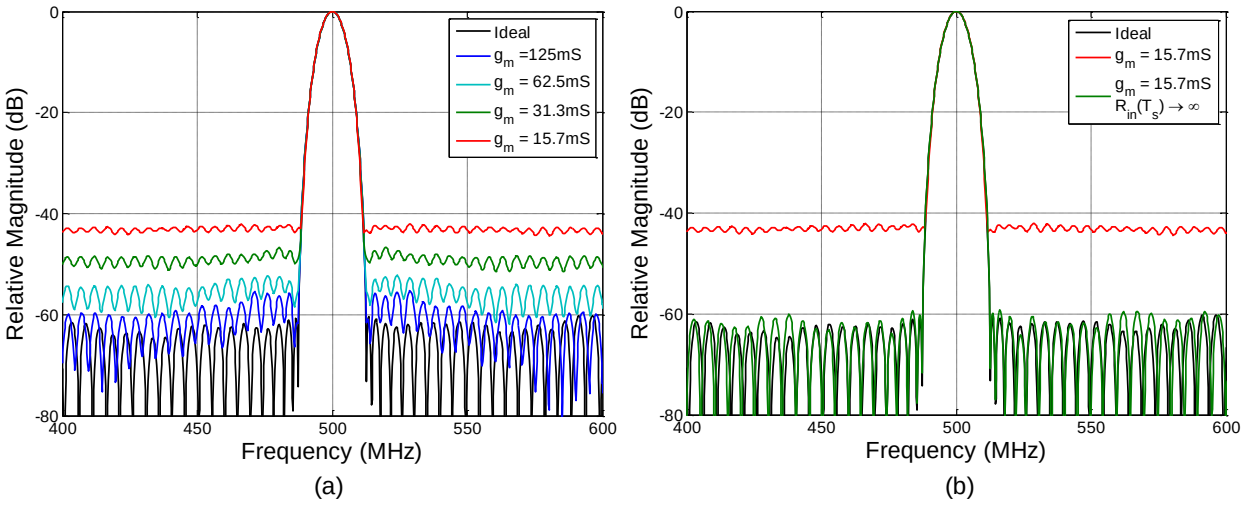

Figure 2.29: (a) Effect of finite op-amp g_m on the filter magnitude response, and (b) its mitigation by setting $R_{in}(T_s) \to \infty$

2.6.2.3 Finite Op-amp Gain and Bandwidth

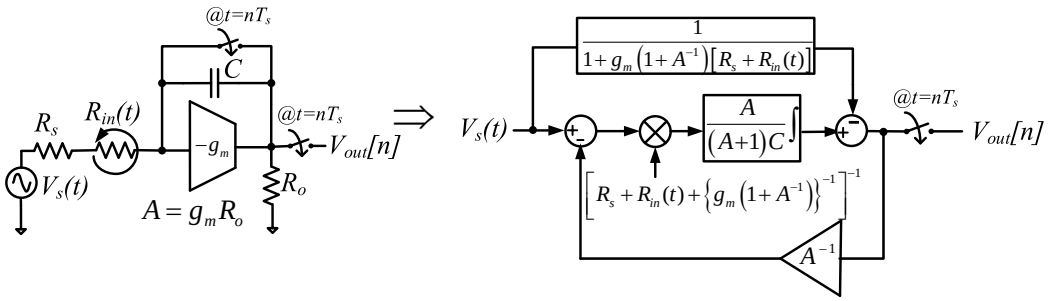

Figure 2.30: Equivalent circuit and block diagram for finite op-amp gain and bandwidth

The effects of finite op-amp gain and bandwidth together gives the block diagram in Fig. 2.30. It can be seen that this is roughly a combinations of the block diagrams Fig. 2.26 and

Fig. 2.28, except that g_m is replaced by $g_m(1+A^{-1})$. Figure 2.31 shows the simulated effect of finite op-amp gain and g_m on a 5MHz BW filter centered at 500MHz, with $C = 100$pF. As noted before, the effect of finite g_m can again be remedied by setting $R_{in}(T_s) \to \infty$.

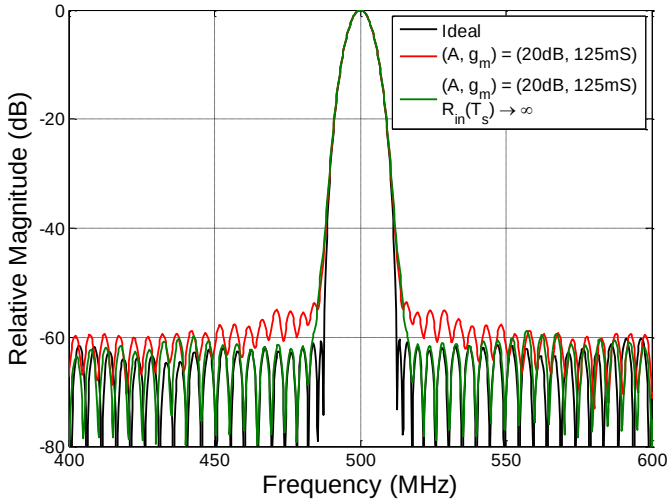

Figure 2.31: Combined effect of finite op-amp gain (A) and bandwidth (g_m) on the filter magnitude response

2.7 Measurement Results

The receiver front-end IC was fabricated in TSMC 1P6M 65nm CMOS process and was packaged in a 40-pin 5mm×5mm QFN package. Figure 2.32 shows the micrograph of the implemented IC. It has an active area of 2mm^2, about two-thirds of which is occupied by capacitors. Note that capacitor area can be significantly reduced while operating with higher filter bandwidths.

A supply voltage of 1.2V is used for the op-amps, the LO dividers, as well as the drivers for controlling the resistor DAC and LO switches. The DC bias of the entire chain is set to around 0.6V due to the op-amp biasing at reset. The rest of the (mostly digital) circuitry runs on a 1V supply. For a 5MHz bandwidth (BW) filter centered on F_{lo}=500MHz, the 1.2V supply draws a current of 57mA from the supply, with each op-amp consuming 13mA, the LO divider and switch drivers consuming about 5mA. The digital and clock generation

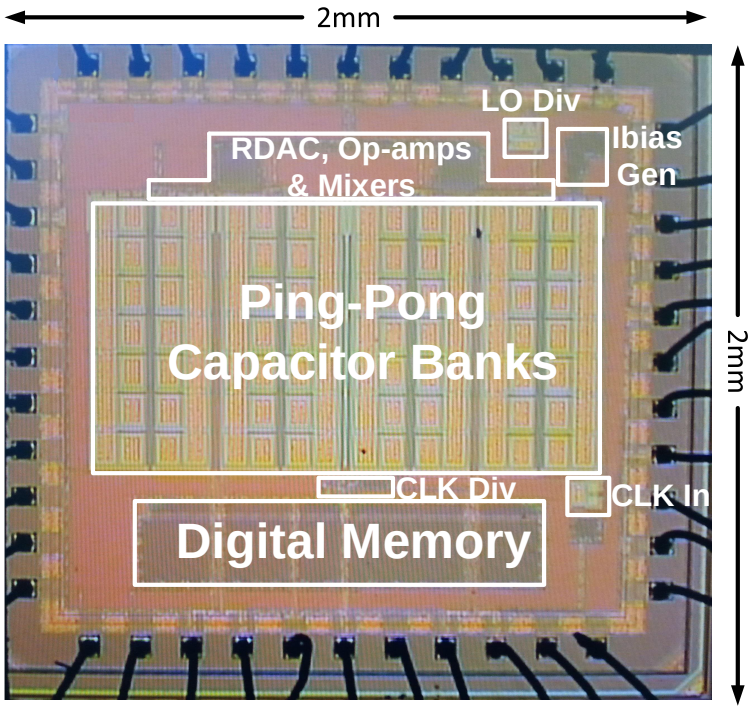

Figure 2.32: Chip micrograph

blocks draw 2mA from the 1V supply for a nominal clock frequency of F_{ck}=1GHz. The system was verified to work up to F_{ck}=2GHz for use with higher filter bandwidths.

The sampled-and-held IC outputs are buffered externally for measurements. Four filter configurations were considered filters 1, 2, and 3 were designed with an S_{11} constraint of -20dB and different transition BWs, while filter 4 only had a transition BW constraint. Figure 2.33(a) shows the measured frequency response of the filter in these configurations. The receiver gain obtained for the 5MHz BW filter with C = 100pF was 18.9dB when configured for matching (filters 1, 2, and 3) and 15.4dB for filter 4. The transition BWs for filters 1, 2, 3, and 4 were 12.5MHz, 22.5MHz, 32.5MHz, and 17.5MHz respectively, while the achieved stop-band rejection was observed to be better than 35dB, 45dB, 50dB, and 48dB respectively. The filter BW was varied from 2.5-40MHz (Fig. 2.33(b)) by varying the resistor variation period (and sampling interval), T_s. The gain scales linearly with T_s and inversely with C. F_{lo} was also varied from 100MHz to 1GHz as shown in Fig. 2.33(c). The gain reduced by 2dB from F_{lo}=100MHz to 1GHz.

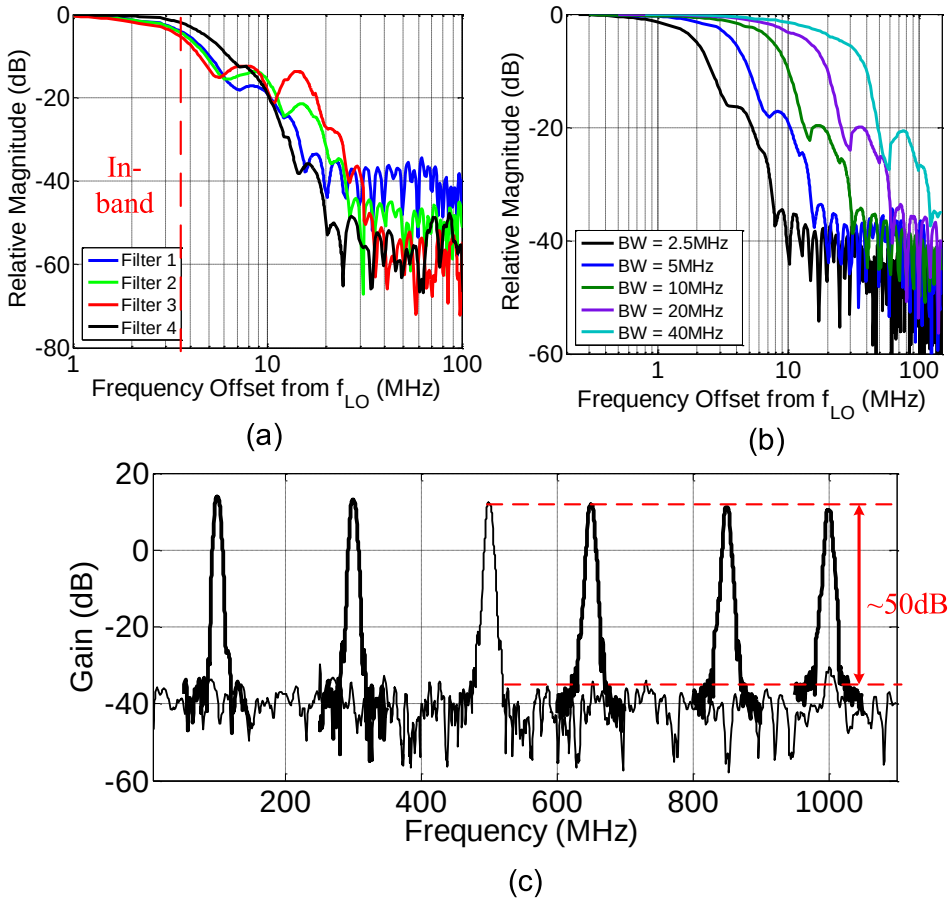

Figure 2.33: a) Measured 5MHz RF BW filter responses, b) Filter 1 responses for BW tuned from 2.5-40MHz, c) Filter 4 responses for the LO varied from 0.1-1GHz

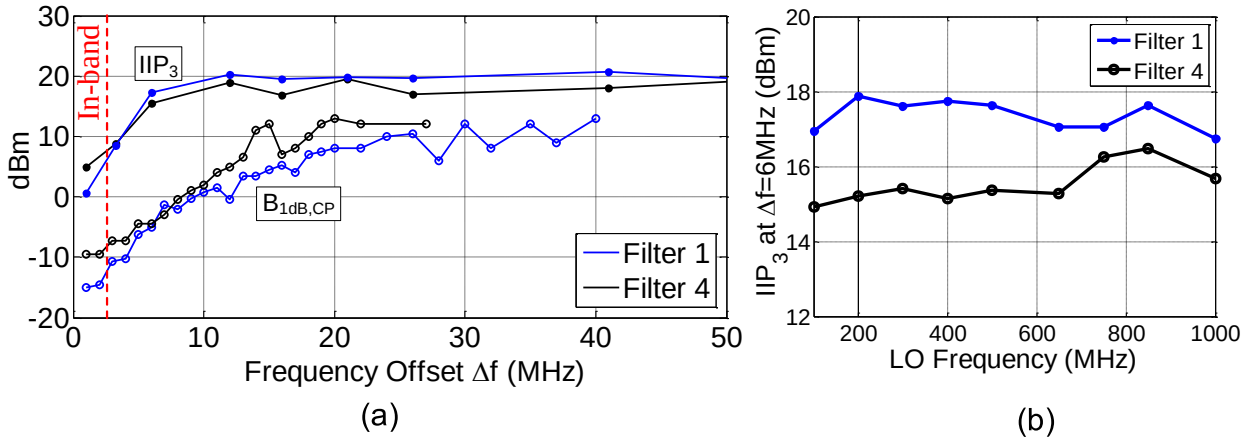

Figure 2.34: a) Measured $\mathrm{IIP_3}$ and $B_{\mathrm{1dB},CP}$ for different frequency offsets from LO for a 5MHz RF BW filter, b) OOB $\mathrm{IIP_3}$ at Δf=6MHz for LO varied from 0.1-1GHz

Figure 2.34 shows linearity measurements. For a 5MHz BW filter 1 configuration (designed for matching) with F_{lo}=500MHz and C = 100pF, while the in-band IIP$_3$ was measured to be about +1dBm, OOB IIP$_3$ was better than +17dBm, and OOB IIP$_2$ was better than +60dBm without calibration, both at 6MHz offset from the carrier. Figure 2.35 shows measured S_{11} of the receiver. The S_{11} was at least -11dB, and better than -12dB for most of the receiver LO range. Note that the S_{11} worsens at higher LO frequencies due to presence of parasitic capacitances from the RDAC, as well as the pads, package and the PCB. The measured noise figure (NF) was 6.5dB. The NF degraded by 12dB if a 0dBm blocker was present at 16MHz offset as shown in Fig. 2.36. The degradation is mostly caused due to the non-optimized design of the LO divider and not due to circuit non-linearity (simulated LO divider phase noise at blocker offset was -155dBc/Hz). It should be noted that if matching is not needed (filter 4 configuration), the in-band IIP$_3$ improves to +5dBm, while the OOB IIP$_3$ was +15dBm at 6MHz offset. The blocker 1dB gain compression point ($B_{1\text{dB},CP}$) is also improved. The S_{11} degrades to only -8dB.

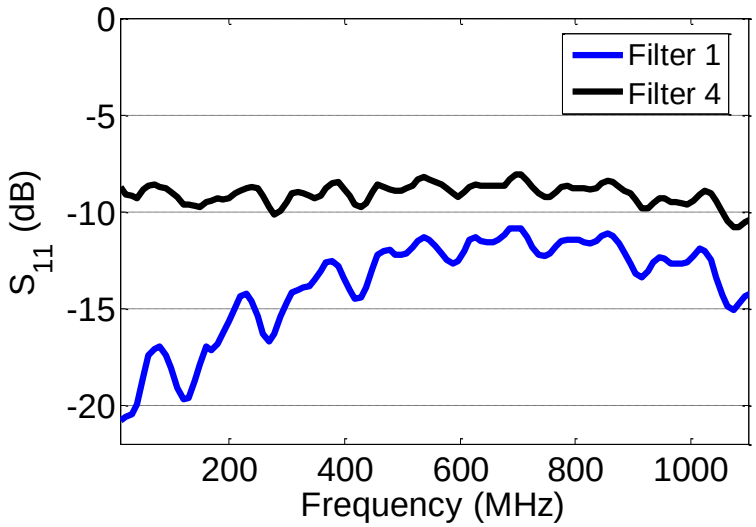

Figure 2.35: Measured S_{11} of the receiver

Table 2.1 compares this work with recent designs. The filtering performance achieved is sharper than most prior art. Comparable linearity is attained, but for blockers at much lower frequency offsets than prior art, with good S_{11} and acceptable NF.

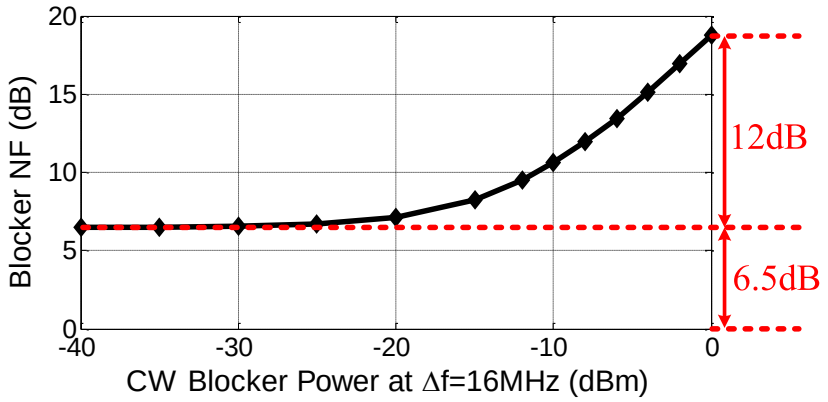

Figure 2.36: Measured blocker noise figure of the receiver

Metric	[12]	[18]	[21]	[22]	This Work	
Architecture	DT Analog	N-path	Mixer-first with Noise Cancelling	Mixer-first + 2nd Order Baseband	FA	FA with Matching
Technology	65nm	65nm	40nm	65nm	65nm	65nm
RF Frequency (GHz)	1.8-2.5	0.1-1.2	0.08-2.7	0.5-3	0.1-1	0.1-1
RF Input	Single-ended	Differential	Single-ended	Differential	Single-ended	Single-ended
BW (MHz)⁺	0.2-20	8	4	2-60	2.5-40	2.5-40
Stop-band Rejection (Transition BW)	>70dB (~4×BW)	59dB (12×BW)	NA	>30dB (~5×BW)	>48dB (3.5×BW)	>35*dB (2.5*×BW)
In-band IIP_3 (dBm)	-7	-12	-20	NA	+5	+1
Out-of-band IIP_3 (dBm)	NA	+26 (Δf=6.25×BW)	+13.5 (Δf=20×BW)	-4.8 (Δf =2×BW)	+15 (Δf=1.2×BW)	+17 (Δf=1.2×BW)
Out-of-band IIP_2 (dBm)	+85	NA	+55	NA	+55 (Δf=1.2×BW)	+60 (Δf=1.2×BW)
$B_{1dB,CP}$ (dBm)	NA	+7 (Δf=6.25×BW)	-2 (Δf=20×BW)	-10 (Δf =2×BW)	+2 (Δf= 2×BW) +13 (Δf=4×BW)	+0.7 (Δf= 2×BW) +8 (Δf=4×BW)
S_{11} (dB)	<-10	-5 to -8	<-8.8	<-10	<-8	<-10
Gain (dB)	82	25	72	50	15.4	18.9
NF (dB)	3.2-4.5	2.8	1.9	4.7	9.8	6.5
Supply Voltage (V)	1.2/2	1.2	1.2/2.5	1.2/2.5	1.2/1	1.2/1
Power Consumption	55-65mW	15-48mA	27-60mA	96mW	56-62mA**	56-62mA**
Active Area (mm^2)	1.1	0.27	1.2	7.8	2	2

⁺RF bandwidth (twice the baseband bandwidth).

*For filter 1. Tunable with a trade-off between transition BW and stop-band rejection.

**Varies with f_{LO}. Power consumption = 59mA for f_{LO}=0.5GHz.

Table 2.1: Performance summary and comparison with prior art

CHAPTER 3

A Time-Interleaved LPTV Receiver Front-End

3.1 Introduction

In Chapter 2 we introduced a receiver front-end based on LPTV circuits. It achieved sharp programmable filtering at RF, while maintaining linearity in the presence of close-in blockers by incorporating a mixer into the sampled integrate-and-dump circuit as shown in Fig. 2.13. By appropriately choosing the periodically time-varying resistor, $R_{in}(t) = R_{in}(t + T_s)$, an equivalent low-pass FIR filter was realized from the input to the sampled output with the desired impulse response, $g(\tau)$, that can be upconverted to a desired LO frequency. It was also shown that by appropriately constraining the resistance variation, a good wideband S_{11} is also achievable.

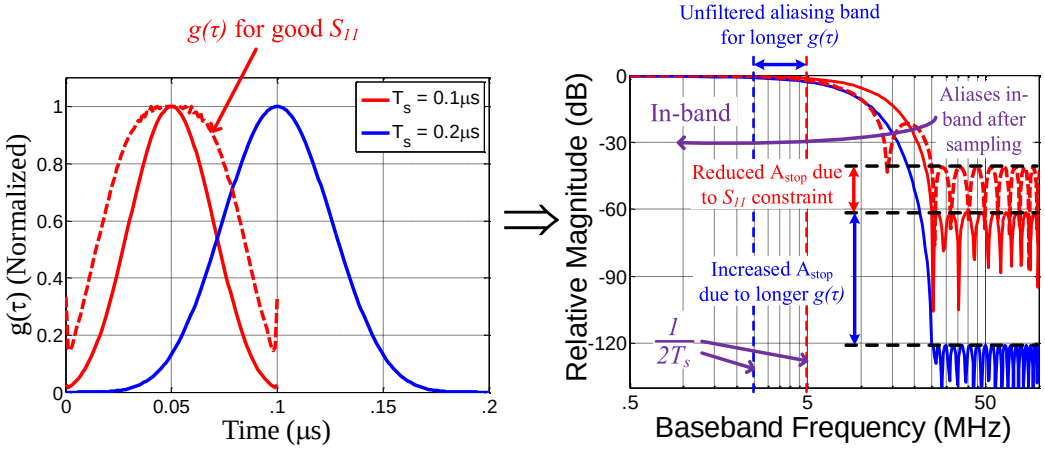

Figure 3.1: Limitations of the LPTV receiver front-end shown in Fig. 2.13 due to the S_{11} constraint and restricted filter length

Nevertheless, the filter stop-band suppression (A_{stop}) is limited due to the additional

S_{11} requirements. Additionally, the inherent sampling implies that the residual blockers alias in-band and cannot be further suppressed by additional filtering. Higher A_{stop} can be potentially achieved by increasing the length of $g(\tau)$. However, in the circuit shown in Fig. 2.13 the filter length is constrained to the output sampling period, T_s. This means that increasing the filter length necessarily reduces the output sampling rate. As shown in Fig. 3.1, for a given filter bandwidth (BW), increasing the length of $g(\tau)$ results in undersampling of the in-band signal. Hence the in-band wanted signal is corrupted by aliasing from adjacent unfiltered bands, and so the filter is rendered useless. Hence, an alternate method is needed to increase the filter length.

In this chapter, we show that the concept of time-interleaving can be used to further improve A_{stop} without sacrificing the performance of the receiver front-end. Time-interleaving allows increase in filter length while maintaining sufficient output sampling rate. Furthermore, we will show that impedance matching becomes easier as well.

3.2 Time-Interleaved FA and Receiver Topology

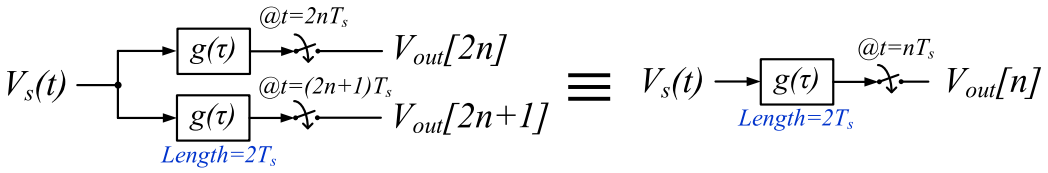

Figure 3.2: Block diagram of a time-interleaved FA system

Time-interleaving (or poly-phasing) is an increasing popular technique that can be used to increase the effective rate of operation of systems such as data converters, integration samplers, digital filters, etc. The concept is to simply time-multiplex multiple identical copies of a single system. Different copies are run by uniformly phase-shifted version of a low-rate clocks, but the time-multiplexed output effectively comes from a higher clock rate system. For example, consider the block diagram in Fig. 3.2, where each filter, $g(\tau)$, is similar to the filter from Fig. 2.9. Note that since the output of each filter is sampled with period $2T_s$, their lengths are $2T_s$ as well. However, if the sampling clocks (and corresponding

variations and clocks in each filter) are offset from each other by T_s, then the effective sampling period is T_s. Hence, the filter length is doubled while maintaining output sampling rate!

3.2.1 Circuit Implementation

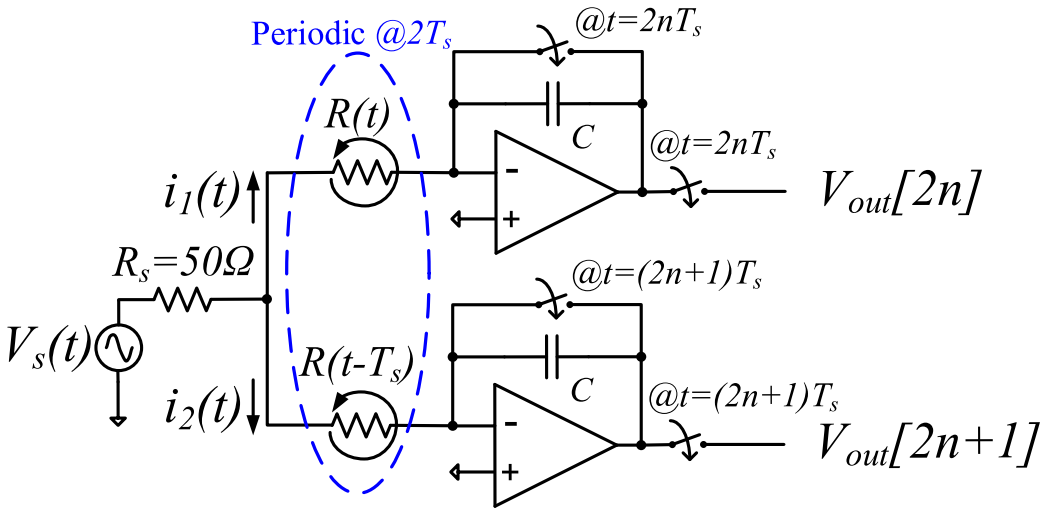

Figure 3.3: Implementation of the time-interleaved FA receiver based on two integrate-and-dump circuits

An example time-interleaved FA system can be achieved using the system shown in Fig. 3.3. By utilizing two sampled integrate-and-dump circuits that are connected together at the source (antenna), each with sampling clocks and resistance variations that are time-shifted by T_s with respect to each other, the block diagram in Fig. 3.2 is realized. Note that the resistance variation, $R(t)$, is periodic the period $2T_s$ that is the sampling period in each path. Then the output voltages can be calculated as

$$\begin{aligned} V_{out}[2n] &= \int_{t=2(n-1)T_s}^{2nT_s} \frac{i_1(t)}{C} dt, \\ V_{out}[2n+1] &= \int_{t=(2n-1)T_s}^{(2n+1)T_s} \frac{i_2(t)}{C} dt. \end{aligned} \tag{3.1}$$

The currents can be simply calculated to be

$$\begin{aligned} i_i(t) &= \frac{R(t-T_s)}{[R(t)+R(t-T_s)]}\frac{V_s(t)}{[R_s+R(t)||R(t-T_s)]}, \\ i_2(t) &= \frac{R(t)}{[R(t)+R(t-T_s)]}\frac{V_s(t)}{[R_s+R(t)||R(t-T_s)]}. \end{aligned} \tag{3.2}$$

Using (3.1) and (3.2), and using the fact that $R(t) = R(t-2T_s)$, it can be verified that $V_{out}[n] = \int_{\tau=0}^{2T_s} g(\tau)V_s(nT_s-\tau)d\tau$, where

$$g(\tau) = \frac{R(T_s-\tau)}{[R(-\tau)+R(T_s-\tau)]}\frac{1}{[R_s+R(-\tau)||R(T_s-\tau)]\,C},\ 0 \le \tau \le 2T_s \tag{3.3}$$

is the realized FIR filter of length $2T_s$. The filter can then be designed using standard digital FIR filter design techniques. We use linear programming to generate the filters.

3.2.2 Impedance Matching

For the circuit in Fig. 3.3, the input impedance at any time instant is simply given by the parallel combination of time-varying resistances, $R(t)$ and $R(t-T_s)$ (which should include the op-amp input impedance and series impedances, such as mixer switch resistance). Hence using (2.10), the S_{11} is given by

$$S_{11} = mean\left[\frac{R(t)||R(t-T_s)-R_s}{R(t)||R(t-T_s)+R_s}\right]. \tag{3.4}$$

Using (3.3), (3.4) can be simplified to give

$$S_{11} = 1-(2R_sC)\,mean\left[g\left(\tau\right)+g\left(\tau-T_s\right)\right],\ T_s \le \tau < 2T_s. \tag{3.5}$$

(3.5) can be further simplified by using the fact that FIR low-pass impulse responses peak at the center, and are small towards the edges, i.e., for (3.2) $g(T_s) \gg g(0) \approx 0$. In that case, the minimum value attainable by $R(t)$, R_{min} (ideally 0, but usually set by other design constraints such as area/power), will be used at the peak of $g(\tau)$, i.e., $R(T_s) = R_{min}$ and $R(0) \to \infty$, and so

$$g\left(T_s\right)+g(0) \approx g\left(T_s\right) = \frac{1}{\left(R_s+R_{min}\right)C} = g_{max},$$

where g_{max} is the peak value of the impulse response, $g(\tau)$. Hence, (3.5) can expressed in terms of the normalized impulse response $g_{norm}^{max}(\tau) = g(\tau)/g_{max}$ (similar to (2.15)) as

$$S_{11} = 1 - \frac{2R_s}{R_s + R_{min}} mean\left[g_{norm}^{max}(\tau) + g_{norm}^{max}(\tau - T_s)\right], \quad T_s \leq \tau < 2T_s. \tag{3.6}$$

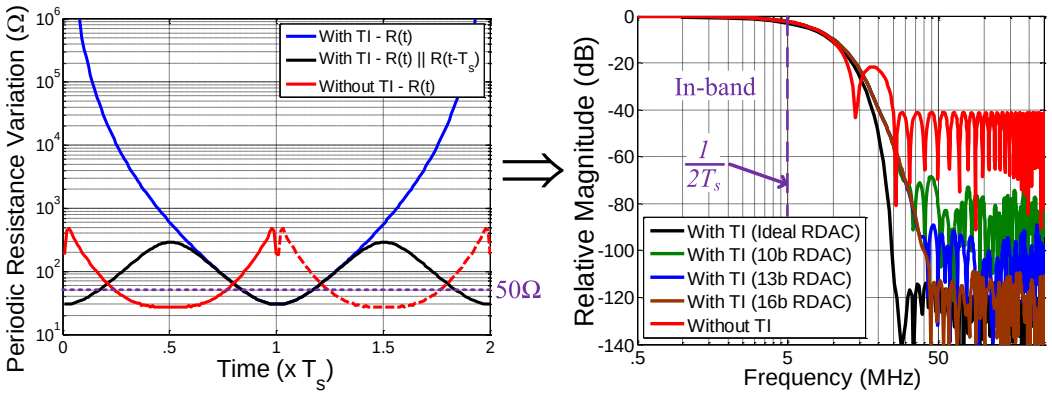

Figure 3.4: Example resistance variation, and the corresponding filter frequency response obtained with time-interleaving for S_{11} = -20dB

Using (3.6), an additional constraint $|S_{11}| \leq \beta$ can be added to the filter design problem, where β is the desired S_{11}. Figure 3.4 shows a filter designed with a desired S_{11} of -20dB with and without time-interleaving for Rs=50Ω, and R_{min}=27Ω (similar to the implementation in this work). It should be noted that up to 120dB of filter suppression can be achieved in this case, compared to only 40dB without time-interleaving. This is clear from the resistance variations, where the parallel combination easily manages to stay around 50Ω similar to the non-interleaved case, but the resistance variation, $R(t)$, itself can vary a lot more. Nevertheless, the actual suppression is limited by the accuracy of the resistance variation, $R(t)$. An accuracy of about 10 bits is necessary for attaining A_{stop} >70dB as seeen in Fig. 3.4.

3.2.3 Noise Figure

The noise performance of the circuit can be analyzed based on the circuit shown in Fig. 3.5. For simplicity, the op-amps are considered to be simple g_m stages with its input-referred noise voltages and input impedances ($1/g_m$) included with the time-varying resistances (case

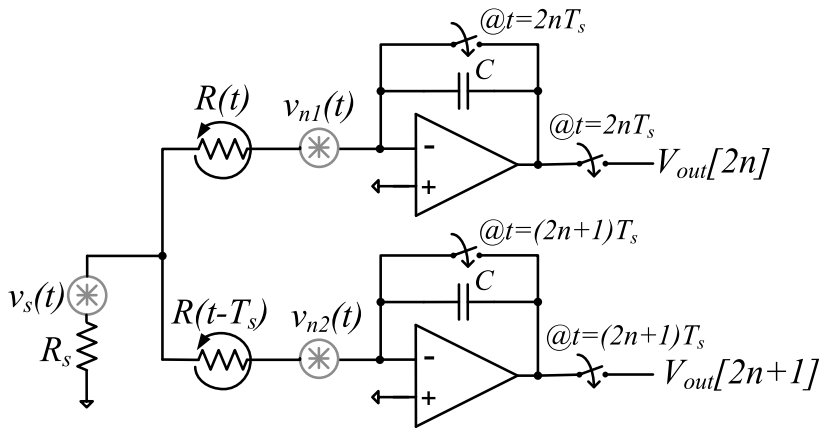

Figure 3.5: Equivalent circuit for noise analysis

of $\gamma = 1$ like in (2.20)). Hence, the noise sources considered are $v_s(t)$, $v_{n1}(t)$ and $v_{n2}(t)$ corresponding to the source, R_s, and time-varying resistances, $R(t)$ and $R(t-T_s)$ respectively. The noise sources are considered white and Gaussian with autocorrelations:

$$\begin{aligned} R_{ss}(t,\tau) &= E\left[v_s(t)v_s(t+\tau)\right] = 2kTR_s\delta(\tau), \\ R_{n_1n_1}(t,\tau) &= E\left[v_{n1}(t)v_{n1}(t+\tau)\right] = 2kTR(t)\delta(\tau), \\ R_{n_2n_2}(t,\tau) &= E\left[v_{n2}(t)v_{n2}(t+\tau)\right] = 2kTR(t-T_s)\delta(\tau), \end{aligned} \tag{3.7}$$

where k is the Boltzmann constant, and T is the temperature in Kelvin. Using superposition, the output voltages can be obtained as

$$\begin{aligned} V_{out}[2n] &= \int_{t=2(n-1)T_s}^{2nT_s} \frac{R(t-T_s)V_s(t)-[R_s+R(t-T_s)]V_{n1}(t)+R_sV_{n2}(t)}{C[R_sR(t)+R_sR(t-T_s)+R(t)R(t-T_s)]}dt, \\ V_{out}[2n+1] &= \int_{t=(2n-1)T_s}^{(2n+1)T_s} \frac{R(t)V_s(t)-[R_s+R(t)]V_{n2}(t)+R_sV_{n1}(t)}{C[R_sR(t)+R_sR(t-T_s)+R(t)R(t-T_s)]}dt. \end{aligned} \tag{3.8}$$

From (3.7) and (3.8), the autocorrelation sequence of the output voltage samples is

$$\begin{aligned} R_{oo}[0] &= E\left[{V_{out}}^2[n]\right] = \frac{2kT}{C^2}\int_0^{2T_s} \frac{R_sR^2(t-T_s)+R(t-T_s)R_s^2+R(t)[R_s+R(t-T_s)]^2}{[R_sR(t)+R_sR(t-T_s)+R(t)R(t-T_s)]^2}dt, \\ R_{oo}[\pm1] &= E\left[V_{out}[n]V_{out}[n\pm1]\right] = \frac{2kT}{C^2}\int_0^{T_s} \frac{R_sR(t)R(t-T_s)-R(t-T_s)R_s[R_s+R(t)]-R(t)R_s[R_s+R(t-T_s)]}{[R_sR(t)+R_sR(t-T_s)+R(t)R(t-T_s)]^2}dt, \\ R_{oo}[\pm m] &= E\left[V_{out}[n]V_{out}[n\pm m]\right] = 0,\ \forall\, m\,\epsilon\,\mathbb{Z},\ |m| \geq 2, \end{aligned} \tag{3.9}$$

where the first term in the numerator in each equation (integral) corresponds to noise from R_s, the second to noise from $R(t-T_s)$, and the last to the noise from $R(t)$. It can be seen that the autocorrelation, $R_{oo}[m]$, is non-zero only for sample delays $|m| \leq 1$. This is intuitively obvious since the noise contribution to output samples in each path are from independent samples of the noise sources (the only memory in the system is due to the load capacitor that is reset after every sample). While the two paths do interact for adjacent samples (since both are operational at the same time), the effect is small. For example, for the filter in Fig. 3.4 the magnitude of the ratio, $R_{oo}[1]/R_{oo}[0]$, is less than 1%. This is because the paths interact only when $R(t) \approx R(t-T_s)$ that happens only for a short period of time.

To compute the noise figure, the noise power spectral density (PSD) can be calculated from the autocorrelation. Further, the noise figure contribution due to noise aliasing (because of sampling), $F_{\text{aliasing}}(\Delta f)$, can be calculated by computing the noise PSD due to noise from R_s alone (computed from the autocorrelation with the first terms in the numerator in each equation in (3.9)), $PSD_{R_s}(\Delta f)$, and comparing it with the case when the noise of R_s simply passes through the filter without aliasing, i.e.,

$$F_{\text{aliasing}}(\Delta f) = \frac{PSD_{R_s}(\Delta f)}{2kTR_s|G(\Delta f)|^2}, \;\; |\Delta f| \leq \frac{F_s}{2}, \tag{3.10}$$

where $G(f)$ is the frequency response of the filter, $g(\tau)$. Similarly, the noise figure contribution of the time-varying resistances to the total baseband noise factor, $F_{\text{baseband}}(\Delta f)$, can be computed by calculating the total PSD, $PSD_{total}(\Delta f)$, using (3.9), and comparing it with $PSD_{R_s}(\Delta f)$, i.e.,

$$F(\Delta f) = \frac{F_{\text{baseband}}(\Delta f)}{F_{\text{aliasing}}(\Delta f)} = \frac{PSD_{total}(\Delta f)}{PSD_{R_s}(\Delta f)}, \;\; |\Delta f| \leq \frac{F_s}{2}, \tag{3.11}$$

Finally, when operated as a bandpass filter with a 4-path 25% duty-cycle mixer, the noise figure degradation due to LO harmonics has to be added as well as is given by [21]

$$F_{\text{harmonics}} = \text{sinc}^{-2}(1/4) \approx 0.91\text{dB}. \tag{3.12}$$

Thus, the total noise figure is given by

$$\begin{aligned} F_{\text{total}}(\Delta f)|_{\text{dB}} &= 10\log_{10}\left[F(\Delta f) \times F_{\text{aliasing}}(\Delta f) \times F_{\text{harmonics}}\right] \\ &= F(\Delta f)|_{\text{dB}} + F_{\text{aliasing}}(\Delta f)|_{\text{dB}} + F_{\text{harmonics}}|_{\text{dB}}, \end{aligned} \tag{3.13}$$

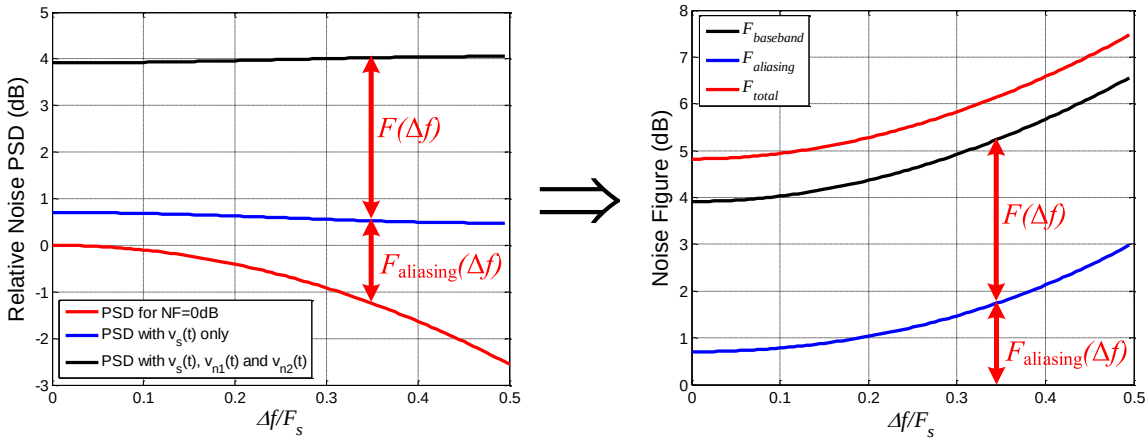

Figure 3.6: Calculated noise figure for the filter in Fig. 3.4

Figure 3.6 shows the calculated PSDs and noise figure of the impedance-matched filter shown in Fig. 3.4. It can be seen that $F|_{\text{dB}} \approx 3.6\text{dB}$, $F_{\text{aliasing}}(\Delta f = 0)|_{\text{dB}} = 0.7\text{dB}$, and the average NF across frequencies is 5.8dB (the filter droop across the band is about 2.5dB). It can be noted that the total PSD is almost white, and $F(\Delta f)$ is almost constant across Δf. This confirms that the correlation between samples is small, and so $F(\Delta f)$ can in fact be approximated by the non-interleaved case (where the PSDs are white). Thus,

$$F(\Delta f) \approx \frac{mean\left[1/(R_s + R(t))\right]}{R_s mean\left[1/(R_s + R(t))^2\right]} \tag{3.14}$$

that evaluates to 3.52dB (an error of <0.1dB).

3.3 Implementation and Non-Idealities

The block diagram of the implemented RF front-end is shown in Fig. 3.7. The 50Ω input is converted to a differential 100Ω input using an external 1:$\sqrt{2}$ balun transformer. The receiver IC consists of two identical time-interleaved paths. In each path the balun output

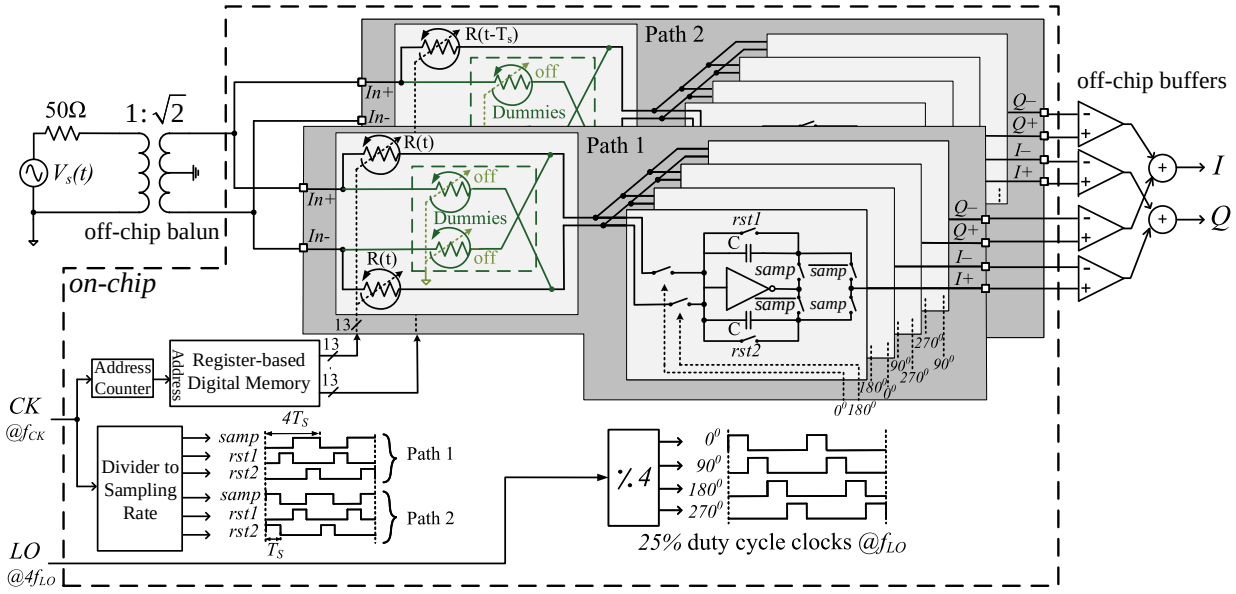

Figure 3.7: Block diagram of the implemented time-interleaved receiver front-end

is connected to a pair LPTV resistors, $R(t)$, that are built as nominally 13b binary-scaled resistor DACs (RDACs). The RDAC control bits are periodic with the period, $2T_s$, and are generated from an on-chip register-based memory that is read out cyclically based on the input clock, F_{ck}. In each path, a set of dummy RDACs (identical to the main RDACs, but with all switches turned off) are connected across the main RDACs in a cross-coupled fashion. This arrangement can be shown to improve the dynamic range of the RDACs.

In each path, the differential RF current is mixed down to baseband by a set of 25% duty-cycle mixer switches switching at the LO frequency, F_{lo}, that realizes a 4-path mixer. The mixer switches use transmission gates with equal sized PMOS and NMOS devices (to minimize LO feed-through and charge injection) and have a resistance of about 3Ω. The baseband integrate-and-dump blocks utilize self-biased inverter-based op-amps, with sampling and reset clocks generated by dividing F_{ck}. Each capacitor bank, C, is built as a ping-pong structure, which allows one capacitor to be connected across the op-amp, while the voltage stored on the other can read and reset using the clocks shown. The capacitor banks use MIM capacitors and are tunable from $10-70$pF to allow for a wide range of filter bandwidths, and their parasitics have no noticeable effect on performance. The op-amps themselves are self-

biased due to the ping-pong action. Each op-amp consists of a high-V_t PMOS and NMOS of length 180nm to increase gain to about 35dB and to reduce the flicker noise corner, and has a transconductance, g_m, of 125mS. The g_m is chosen to minimize noise figure contribution, as well as to minimize the opamp-input impedance ($1/g_m$), thus reducing the minimum resistance achievable at the front-end, R_{min}, to aid in impedance-matching (op-amp gain and g_m do not significantly affect A_{stop} similar to the non-interleaved case). To achieve the time-interleaving operation the RDAC controls and the sampling and reset clocks for the two paths are offset in time by T_s. Each path can be turned on or off independently to test for non-interleaved operation. The LO switches connected to the negative input can also be turned off for single-ended operation.

The most important non-idealities are now considered and their effects shown.

3.3.1 RDAC Parasitics

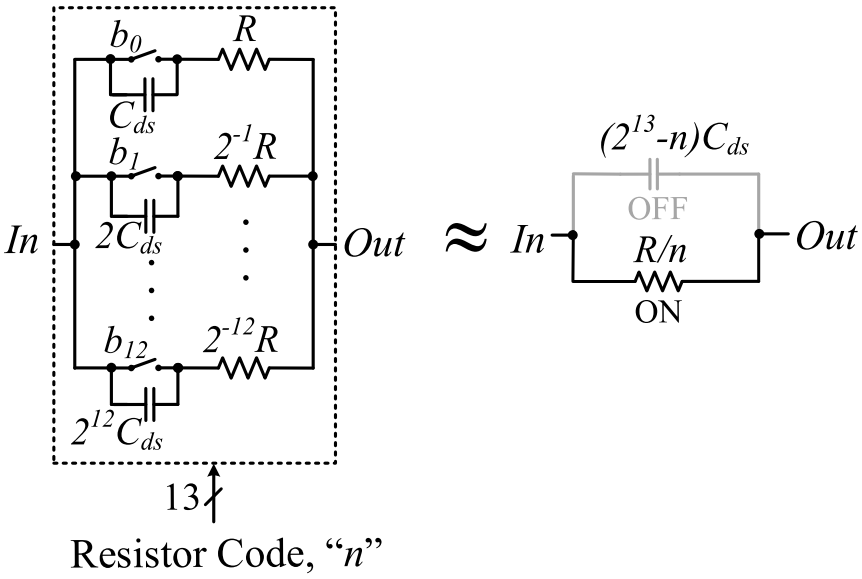

Figure 3.8: Schematic of the 13-bit resistor DAC with annotated C_{ds} parasitic capacitance

The heart of the receiver front-end are the 13-bit RDACs shown in Fig. 3.8. As shown, the RDAC is implemented in a binary-scaled fashion, with each branch consisting of an *rppoly* resistor, R, in series with a transmission gate control switch (with equal sized PMOS

and NMOS devices) with resistance, R_{sw}. The minimum RDAC resistance was designed to be about 15.7Ω. R_{sw} : R was set to 1:4 as a trade-off between linearity, switch parasitics, and power consumption. improve the dynamic range of the RDACs.

As discussed in Chapter 2, the primary contributor to lower A_{stop} is the C_{ds} capacitance that is present mainly present due to routing. As shown in Fig. 3.8, when the RDAC is set to a resistor code of n, the ON-paths contribute to give the desired resistance of R/n. However, the OFF-path C_{ds} capacitance add in parallel to give a capacitance of $(2^{13}-n)C_{ds}$, thus leading to a corner frequency of

$$\omega_{corner} = \frac{n}{2^{13}-n}\frac{1}{RC_{ds}}.$$

Note that ω_{corner} reduces for smaller n, and so the RDAC does not realize large resistance values. Hence the RDAC dynamic range is degraded, leading to lower A_{stop} (a dynamic range of ∼10b is needed for A_{stop} >70dB as shown in Fig. 3.4).

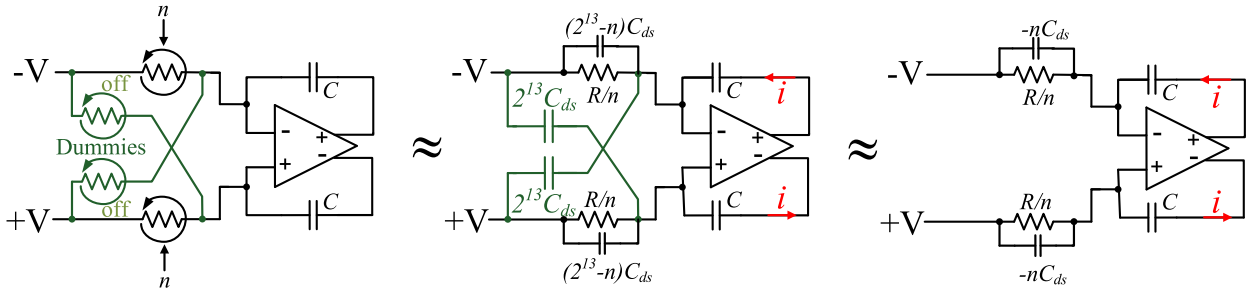

Figure 3.9: Alleviation of parasitic C_{ds} capacitance using cross-coupled dummy RDACs

To alleviate this problem, consider the differential circuit in Fig. 3.9. The main RDACs are set to a code, n, while the two additional dummy RDACs (connected in a cross-coupled fashion) are set to OFF, i.e., set to a code of 0. From the equivalent circuit, it can be seen that the output differential current is given by

$$i = \frac{nV}{R} - nC_{ds}\frac{dV}{dt}.$$

This implies that the equivalent circuit can be drawn as in Fig. 3.9(c). Thus the corner frequency of the RDACs now becomes

$$\omega_{corner} = \frac{1}{RC_{ds}}$$

that is constant with respect to code, n. Moreover this corner frequency is typically much higher than the frequency range of interest and so RDAC dynamic range is restored. Measurement results for an example filter shown in Fig. 3.10 confirms the utility of this technique, with A_{stop} improved by 17dB.

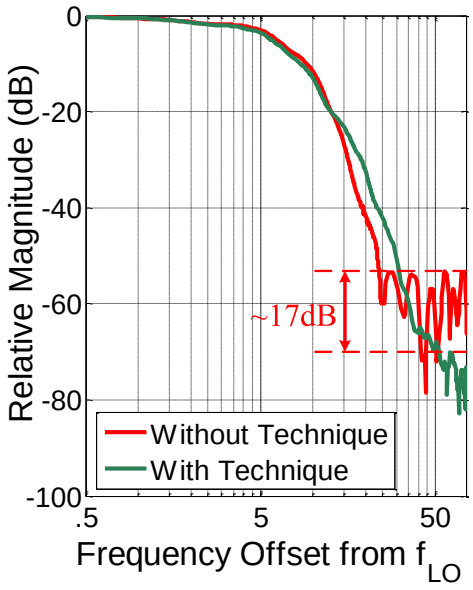

Figure 3.10: Measured improvement in the filter magnitude response due to the cross-coupled dummy RDACs

3.3.2 Path Mismatches

Figure 3.11 shows important sources of mismatch in the time-interleaved implementation. The time-varying resistance values, $R_1(t)$ and $R_2(t)$ are nominally equal, but can be mismatched due to random mismatches in the RDACs or a systematic mismatch between them (this can capture gain mismatches in the baseband integrators as well). Further, the timing offset between the resistance variations, while ideally T_s, can be slightly different as well, i.e., $T_s + \Delta T$ with $\Delta T \neq 0$. This results in slightly mismatched impulse responses in the two paths, given by $g_1(\tau)$ and $g_2(\tau)$:

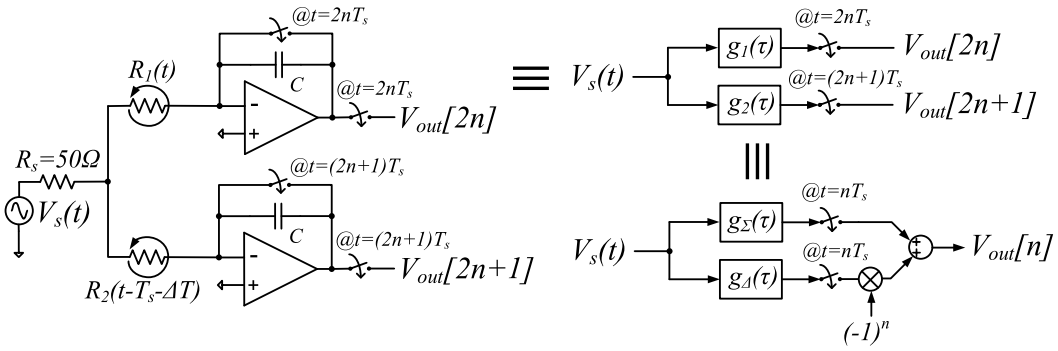

Figure 3.11: Model to analyze the effect of circuit mismatches on the filter

$$g_1(\tau) = \frac{R_2(T_s-\tau+\Delta T)}{[R_1(-\tau)+R_2(T_s-\tau+\Delta T)]}\frac{1}{[R_s+R_1(-\tau)||R_2(T_s-\tau+\Delta T)]C},$$
$$g_2(\tau) = \frac{R_1(T_s-\tau)}{[R_1(T_s-\tau)+R_2(-\tau+\Delta T)]}\frac{1}{[R_s+R_1(T_s-\tau)||R_2(-\tau+\Delta T)]C}, \quad 0 \le \tau \le 2T_s.$$

These can be further simplified to give

$$\begin{aligned} g_\Sigma(\tau) &= \tfrac{1}{2}\left[g_1(\tau) + g_2(\tau)\right], \\ g_\Delta(\tau) &= \tfrac{1}{2}\left[g_1(\tau) - g_2(\tau)\right], \end{aligned} \tag{3.15}$$

as shown in Fig. 3.11, where $g_\Sigma(\tau)$ is the desired filter impulse response, and $g_\Delta(\tau)$ is the undesired image filter response that results due to the imperfect cancellation of the aliasing images (similar to the case of timing mismatch in a time-interleaved ADC). While the desired filter, $g_\Sigma(\tau)$, filters the input and aliases to the correct sub-sampled discrete-time frequency, ω_{corr}, the undesired filter, $g_\Delta(\tau)$, aliases the filtered signal to the image frequency of $(\omega_{corr} \pm \pi)$. The effects of various mismatches can be quantified through the frequency responses of the filters, $g_\Sigma(\tau)$ and $g_\Delta(\tau)$. In the following, the effect of mismatches are characterized for the filter shown in Fig. 3.4.

3.3.2.1 RDAC Resistance Mismatch

The binary-scaled RDACs are built as parallel combination of unit cells that are subject to random mismatches. Hence the RDACs have to be calibrated to achieve the accuracy required for A_{stop} of 70dB. To model the effect of calibration, the random RDAC code vs. resistance curves are generated such that for a code of n, the resistance produced by the

RDAC is modeled to be R/k, where k is uniformly distributed in $\left[\left(n-\frac{\Delta}{2}\right),\left(n+\frac{\Delta}{2}\right)\right]$, and Δ is set by the calibration accuracy (ideally a truncated Gaussian, uniform distribution is a worst-case approximation). For example, in an M-bit RDAC calibrated to B bits of accuracy, $\Delta = 2^{M-B}$. Using such a model and the ideal resistance codes, the filters from (3.15) can be calculated for generating their frequency responses. For example, Fig. 3.12 shows the frequency responses for a randomly generated case for a 13-bit RDAC calibrated to 10 bits. Comparing the filter, $G(f)$ obtained for ideal 13-bit RDACs to the desired $G_\Sigma(f)$, it can be seen that A_{stop} worsens due to mismatch. The stop-band achieved is similar to that of the image filter, $G_\Delta(f)$.

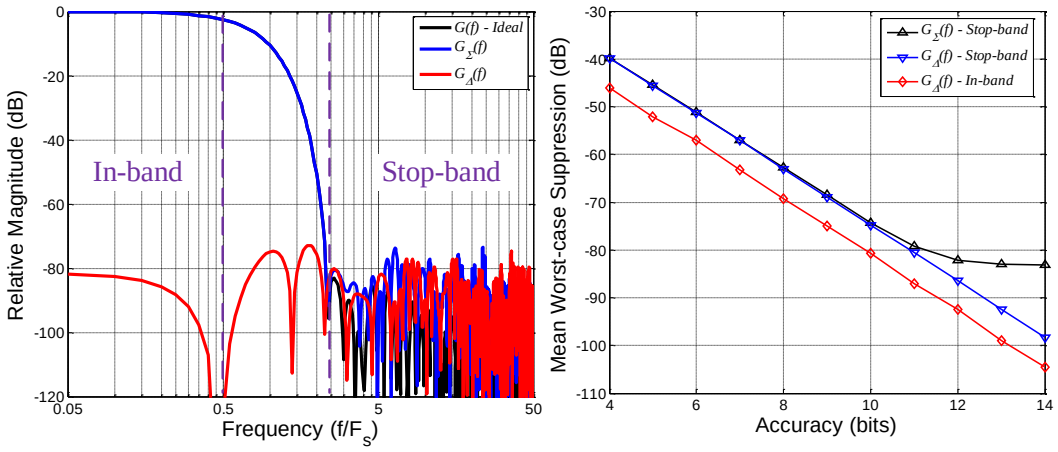

Figure 3.12: Effect of random resistance variation in the RDACs on filter performance

Figure 3.12 also plots the variation of the mean worst-case suppression in the stop-band for $G_\Sigma(f)$ and $G_\Delta(f)$, and the mean worst-case suppression in-band for $G_\Sigma(f)$ and $G_\Delta(f)$ averaged over 1000 randomly generated RDAC profiles (for each accuracy level) for a 13-bit RDAC. It can be seen that to achieve A_{stop} better than 70dB, more than 9 bits of accuracy is necessary.

A second concern in terms of RDAC resistance values is systematic mismatch between RDACs in two time-interleaved paths. For example, consider a systematic mismatch of α between $R_1(t)$ and $R_2(t)$ in Fig. 3.11, i.e., $R_2(t)/R_1(t) = (1-\alpha/2)/(1+\alpha/2)$. The effect of such an offset of the filters can be easily calculated as before. For example, Fig. 3.13 shows the case for α=2%. It can be seen that while stop-band suppression is unaffected,

the suppression of the image filter, $G_\Delta(f)$, in-band is much lower than for random variation. Nevertheless the required in-band suppression is much lower in general, since the aliasing band is the wanted signal band itself. Figure 3.13 also plots the variation of worst-case suppression for the desired and undesired filters as a function of percentage mismatch. It can be seen that to maintain in-band image suppression below 40dB, at least 2% matching is necessary. Note that the requirement will be similar for gain mismatch between integrators, since the effect is similar to the aforementioned systematic mismatch between RDACs.

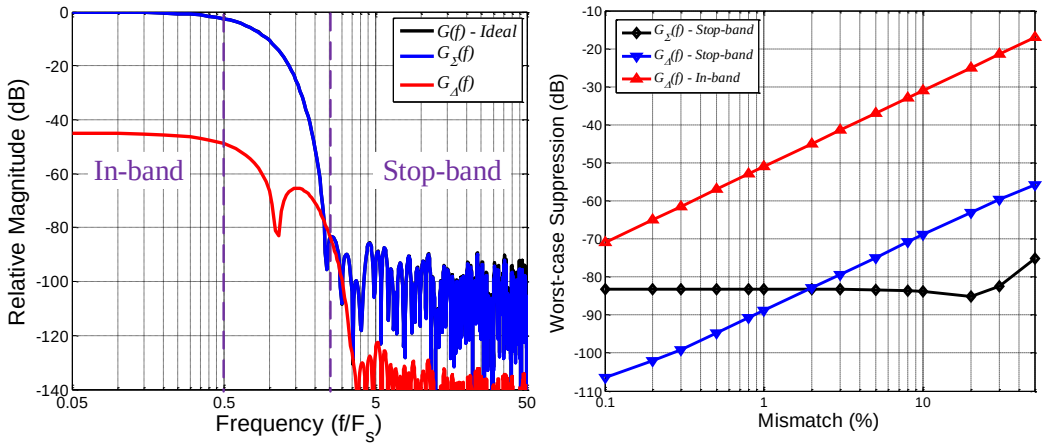

Figure 3.13: Effect of systematic resistance variation between RDACs on filter performance

3.3.2.2 Timing Mismatch

Timing mismatch between RDAC controls can have a severe impact on the image filter. For example, Fig. 3.14 shows the effect of a timing mismatch of ΔT that is 0.5% the net sampling period, T_s. Similar to the case of systematic RDAC mismatch the stop-band suppression is unaffected, but the suppression of the image filter, $G_\Delta(f)$, is only about 45dB. This might be sufficient for typical SNR requirements, since the aliasing image signal is the in-band signal itself. Figure 3.14 also plots the variation of worst-case suppression for the desired and undesired filters as a function of percentage mismatch. It can be seen that to maintain in-band image suppression below 40dB, at least 1% matching is necessary. Nevertheless, it must be noted that the RDAC controls are switched at a clock frequency, F_{ck}. Hence, the RDAC controls can easily be shifted in steps of $T_{ck} = 1/F_{ck}$ to achieve a maximum mismatch

of $T_{ck}/2$. Hence, if T_{ck}/T_s <2%, i.e., an oversampling factor of 50, timing mismatch is not an issue.

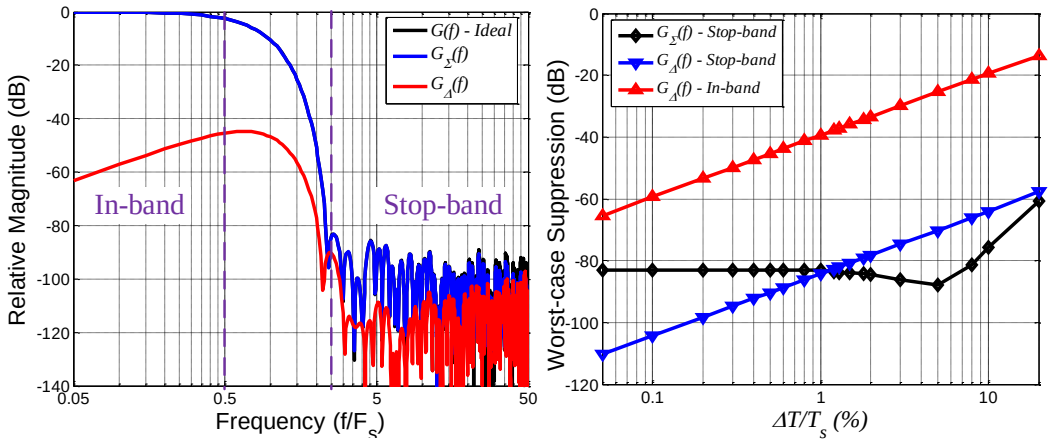

Figure 3.14: Effect of timing skew between RDAC controls of the two paths on filter performance

3.4 Measurement Results

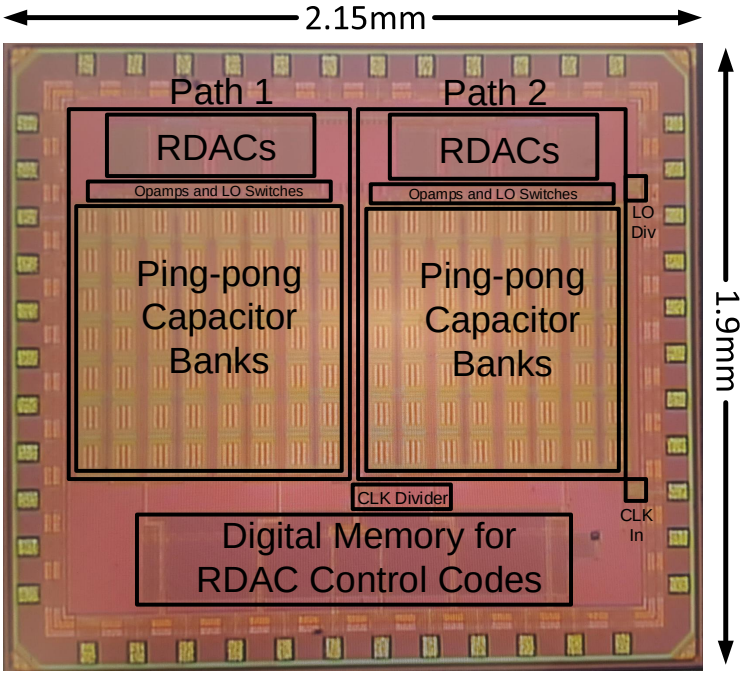

Figure 3.15: Chip micrograph

The receiver front-end IC was fabricated in TSMC 1P6M 65nm CMOS process and was packaged in a 40-pin 5mm×5mm QFN package. Figure 3.15 shows the micrograph of the implemented IC. It has an active area of 2.3mm^2, of which 70% is occupied by capacitors. The capacitor area can be significantly reduced for operating with higher filter bandwidths.

A supply voltage of 1.2V is used for the op-amps, the LO dividers, as well as the drivers for controlling the resistor DAC and LO switches. The DC bias of the entire chain is set to around 0.6V due to the op-amp biasing at reset. The rest of the circuitry runs on a 1V supply. For a 10MHz bandwidth (BW) filter centered on F_{lo} =500MHz, a current of 64.7mA is drawn from the 1.2V supply, with each op-amp consuming 6.5mA, the LO divider and switch drivers consuming about 12.7mA, while the other digital blocks draw 7.75mA from the 1V supply for a nominal clock frequency of F_{ck}=1GHz. The system was verified to work up to F_{ck} =2GHz for use with higher filter bandwidths.

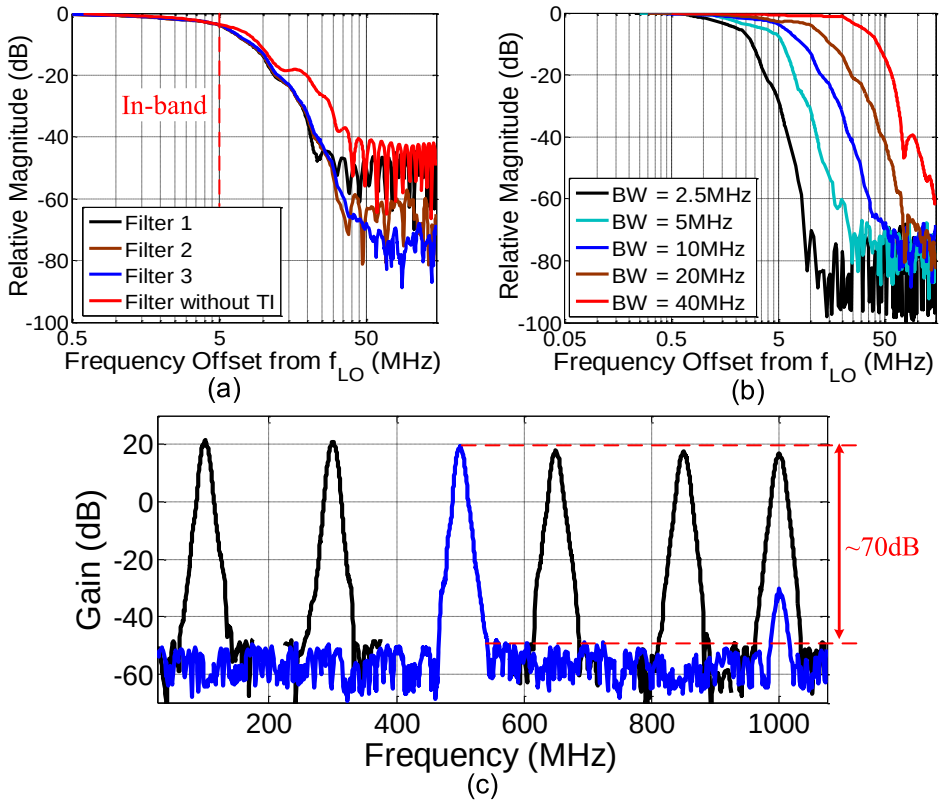

Figure 3.16: a) Measured 10MHz RF BW filter responses, b) Filter 3 responses for BW tuned from 2.5-40MHz, c) Filter 3 responses for the LO varied from 0.1-1GHz

The sampled-and-held outputs of the time-interleaved paths are buffered and combined externally for measurements. Figure 3.16(a) shows the measured filter response in three different time-interleaved 10MHz BW filter configurations (filters 1-3) that vary in transition BW and attenuation. The transition BWs for filters 1, 2, and 3 were 17MHz, 25MHz, and 40MHz respectively, while the achieved stop-band rejection was observed to be better than 45dB, 58dB, and 70dB respectively. In comparison, the measured non-interleaved filter achieved a stop-band rejection of only 40dB with a transition BW of 35MHz. The filter BW was varied from 2.5-40MHz by varying T_s as shown in Fig. 3.16(b). The receiver gain obtained for the 10MHz BW filter with C = 70pF was 23dB. The gain scales linearly with T_s and inversely with C. F_{lo} was also varied from 100MHz to 1GHz as shown in Fig. 3.16(c). The gain reduced by ∼4dB from F_{lo} =100MHz to 1GHz.

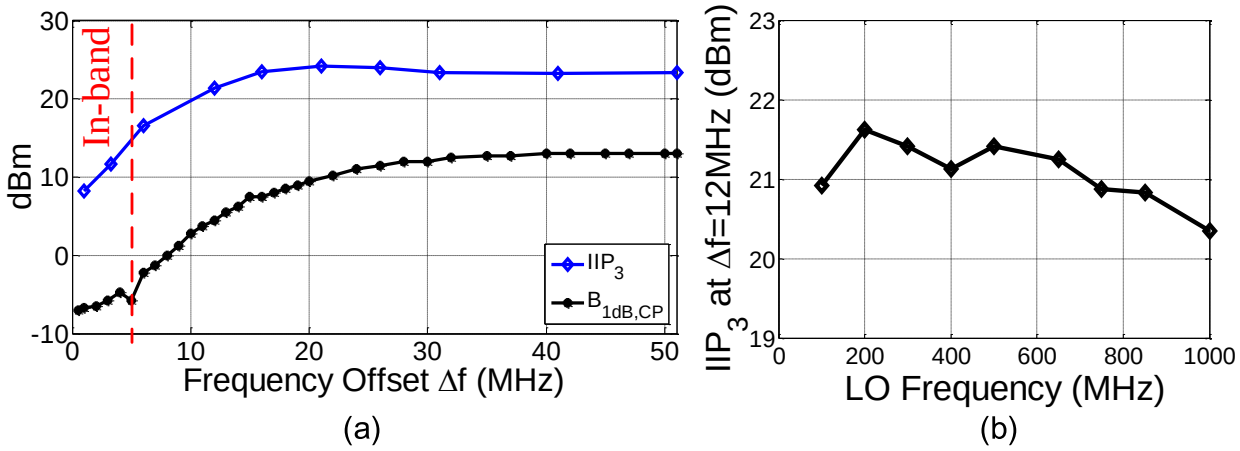

Figure 3.17: a) Measured IIP$_3$ and $B_{1\text{dB},CP}$ for different frequency offsets from LO for a 10MHz RF BW filter, b) OOB IIP$_3$ at Δf=12MHz for LO varied from 0.1-1GHz

Figure 3.17 shows linearity measurements for a 10MHz BW filter 1 configuration with F_{lo} =500MHz and C = 70pF. While the in-band IIP$_3$ was measured to be about +8.2dBm, OOB IIP$_3$ was better than +21.4dBm, and OOB IIP$_2$ was better than +64dBm without calibration, both at 12MHz offset from the carrier. The measured S_{11} is shown in Fig. 3.18. The S_{11} is better than -10dB for most of the receiver LO range, degrading to only -9dB at F_{lo} =1GHz. Note that the S_{11} worsens at higher LO frequencies due to presence of parasitic capacitances from the RDACs, as well as the pads, package and the PCB. The measured NF

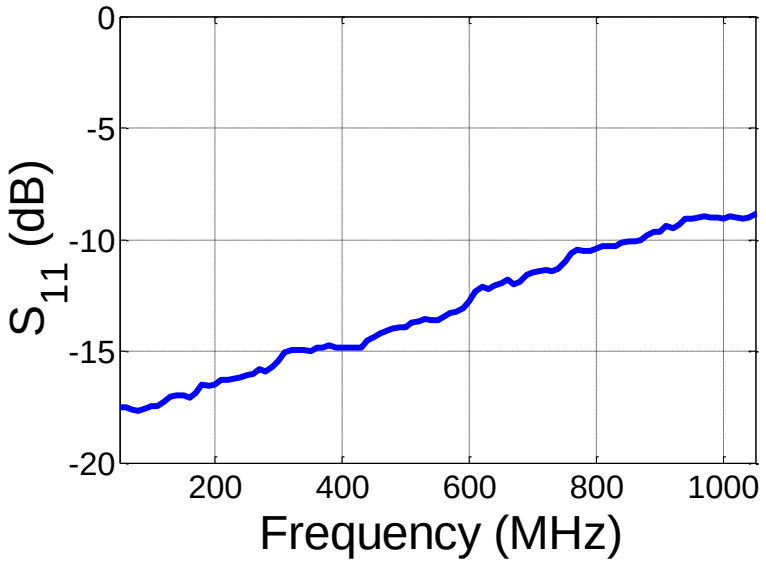

Figure 3.18: Measured S_{11} of the receiver

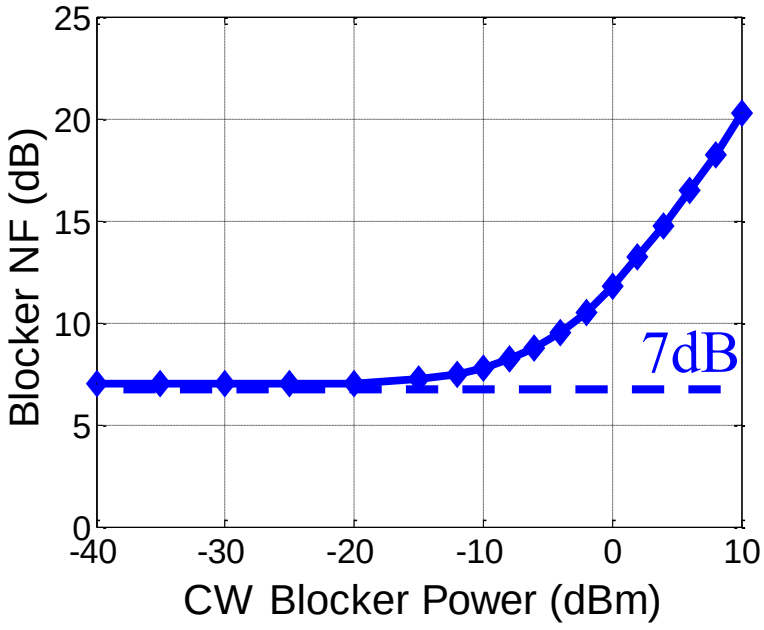

Figure 3.19: Measured blocker noise figure of the receiver

was 7dB, and worsens by only 4.5dB when a 0dBm CW blocker was present at 30MHz offset as shown in Fig. 3.19. This is consistent with the simulated phase noise of the LO divider that was about -165dBc/Hz at the blocker offset.

Table 3.1 compares this work with recent designs. This work maintains the high linearity of the prior receiver front-end detailed in Chapter 2, especially with respect to close-in blockers, while achieving sharper filtering and higher suppression than prior art. Good S_{11} is achieved while not degrading the NF.

Metric	[18]	[14]	[21]	[26]	This Work
Architecture	N-path	N-path + DT filtering	Mixer-first with Noise Cancelling	FA	FA with Time Interleaving
Technology	65nm	40nm	40nm	65nm	65nm
RF Frequency (GHz)	0.1-1.2	0.1-0.7	0.08-2.7	0.1-1	0.1-1
RF Input	Differential	Differential	Single-ended	Single-ended	Differential
BW (MHz)⁺	8	6.4-9.6	4	2.5-40	2.5-40
Stop-band Rejection (Transition BW)	59dB (12xBW)	>70dB (~8.5xBW)	NA	>35dB (2.5xBW) >50dB (6.5xBW)	>45dB (1.7xBW) >70dB (4xBW)
In-band IIP_3 (dBm)	-12	NA	-20	+1	+8
Out-of-band IIP_3 (dBm)	+26 (Δf=6.25xBW)	+24 (Δf=4.7xBW)	+13.5 (Δf=20xBW)	+17 (Δf=1.2xBW)	+21 (Δf=1.2xBW)
Out-of-band IIP_2 (dBm)	NA	NA	+55	+60	+64
$B_{1dB,CP}$ (dBm)	+7 (Δf=6.25xBW)	+14.7 (Δf=4.7xBW)	-2 (Δf=20xBW)	+0.7 (Δf=2xBW) +8 (Δf=4xBW)	+9.5 (Δf=2xBW) +13 (Δf=4xBW)
S_{11} (dB)	-5 to -8	<-10	<-8.8	<-10	<-9
Gain (dB)	25	40	72	18.9	23
NF (dB)	2.8	6.8-9.7	1.9	6.5	7*
Supply Voltage (V)	1.2	1.2/1.6	1.2/2.5	1.2/1	1.2/1
Power Consumption	15-48mA	59-105mW	27-60mA	56-62mA	64-84mA**
Active Area (mm^2)	0.27	2.03	1.2	2	2.3

⁺RF bandwidth (twice the baseband bandwidth).

*Excludes balun loss

**Varies with f_{LO}. Power consumption = 73mA for f_{LO} = 0.5GHz.

Table 3.1: Performance summary and comparison with prior art

CHAPTER 4

LPTV Circuit Analysis Using Conversion Matrices

4.1 Introduction

As we saw in Chapters 2 and 3, LPTV circuits are excellent candidtes for reconfigurable receiver front-ends. In fact most candidates for reconfigurable receivers such as N-path filters [23], mixer-first receivers [19] and dscrete-time analog filters [11] are all LPTV in nature. Analysis of such circuits, however, poses a formidable challenge. Generally, the periodically time-varying nature of such circuits (due to the presence of clock-driven switching elements) leads to frequency translation of the circuit's voltages and currents, and so traditional Laplace or Fourier domain linear time invariant (LTI) circuit analysis techniques have limited applicability.

Several techniques to analyze LPTV circuits have been reported. Since the circuit is linear, we can still use the impulse response to characterize it. However, due to the time-varying nature of the circuit, the impulse response is also time-varying, and hence depends on both the time t and the delay τ, and so is represented by $h(t,\tau)$. Thus, the output, $y(t)$, is related to the input, $u(t)$, by the convolution

$$y(t) = \int_{-\infty}^{\infty} u(t-\tau)h(t,\tau)d\tau. \tag{4.1}$$

Since the time-variation is periodic, the impulse response $h(t,\tau)$ is periodic in t by the fundamental period of the LPTV system, $T_p = 2\pi/\omega_p$. Hence, it can be expanded as a Fourier series as $h(t,\tau) = \sum_{n=-\infty}^{\infty} h_n(\tau)e^{-jn\omega_p t}$. Substituting for $h(t,\tau)$ in (4.1), then taking the Fourier transform (in t) and simplifying gives

$$\begin{aligned} Y(\omega) &= \sum_{n=-\infty}^{\infty} \widetilde{H}_n(\omega - n\omega_p) U(\omega - n\omega_p) \\ &= \sum_{n=-\infty}^{\infty} H_n(\omega) U(\omega - n\omega_p), \end{aligned} \tag{4.2}$$

where $U(\omega)$ and $Y(\omega)$ are the Fourier transforms of the input and output respectively, $\widetilde{H}_n(\omega)$ is the Fourier transform of $h_n(t)$, and the set of transfer functions, $H_n(\omega) = \widetilde{H}_n(\omega - n\omega_p)$, are known as the "*harmonic transfer functions*" (HTFs). Note that the HTFs are just recentered $\widetilde{H}_n(\omega)$ (by convention). Now, finding the HTFs becomes the goal of the circuit analysis [27, 28, 29, 30, 31]. Analogously in LTI systems only a single function, $H_0(\omega)$, which is the transfer function, is required.

Many works start by applying Kirchhoff's laws in the time domain, followed by a transformation to the Fourier domain. For example, [20, 32] follow this strategy to derive the characteristics of 25% duty-cycle, current-driven passive mixer-based receivers, for which the operation of switches is modeled as a multiplication of signal currents by a square wave of the appropriate duty cycle. The work in [19] studies a mixer-first receiver and gives expressions for input impedance and matching requirements using a similar charge balance based approach. Generalized approaches to solve for $H_n(\omega)$, on the other hand, assume relations of the form of (4.2) between the input and every node in the circuit, substitute them in Kirchhoff's voltage and current law equations in Laplace (or Fourier) domain, and solve the resultant set of linear equations. Only a truncated set of frequency translations in (4.2) are considered with the hope of making the analysis problem tractable [30, 33].

The works in [28, 29, 31], on the other hand, model the operation of LPTV circuits using a state-space-based approach. The LPTV circuit is treated as periodically moving through a set of states, in each of which the circuit operates as an LTI circuit. The final conditions of one state serves as the initial conditions of the next state, the result being a set of coupled LTI analysis problems that when solved gives $H_n(\omega)$. This approach work well when the LPTV circuit only has a few states, for example, a few switches being turned ON or OFF, and has been successfully applied in studying N-path filters [16]. However, the consideration of even simple circuit non-idealities such as non-zero rise/fall times and parasitic elements

rapidly increases the number of states and makes such analysis intractable.

This chapter highlights an alternative method of analysis that uses the theory of conversion matrices. Conversion matrices have been extensively studied in literature in the area of computer simulation of complex time-varying circuits [34], and its use has even been extended to non-linear circuits [35, 36]. They have also been proven useful in studying noise in large RF circuits [37]. We show that traditional LTI analysis methods can be extended to LPTV circuits by using conversion matrices. We show that analogues to LTI circuit relations and laws, such as, Ohm's law, Kirchhoff's laws, impedance combination rules, etc. exist for LPTV components and circuits based on conversion matrices. Such analogues can hence be used to analyze LPTV circuits as well.

4.2 Conversion Matrices

Consider, a time domain signal, denoted by $x(t)$, and its Fourier transform, $X(\omega)$. Let us define the k^{th} "*frequency slice*" of $x(t)$ as a band of $X(\omega)$ of width ω_p centered at $k\omega_p$ relocated to DC, where k is an integer and ω_p is a positive real constant:

$$X_k(\omega) = \begin{cases} X(\omega + k\omega_p), & \omega\epsilon[-\frac{1}{2}\omega_p, \frac{1}{2}\omega_p) \\ 0, & \text{elsewhere.} \end{cases} \tag{4.3}$$

Note that $X(\omega)$ is simply the sum of its frequency slices with appropriate frequency shifts:

$$X(\omega) = \sum_{k=-K}^{K} X_k(\omega - k\omega_p), \tag{4.4}$$

where K is infinite in general, but a finite K is sufficient when $x(t)$ is band-limited or when it is sufficient to approximate $x(t)$ with a bandlimited version of the same. The "*frequency vector*", $\underline{X}(\omega)$, of $x(t)$ is a column vector of the frequency slices of $x(t)$ for $-K \leq k \leq K$:

$$\underline{X}(\omega) = [\ X_{-K}(\omega) \quad ... \quad X_0(\omega) \quad ... \quad X_K(\omega)\ ]^T. \tag{4.5}$$

Let us assume that $U(\omega)$ and $Y(\omega)$ in (4.2) are band-limited to $\omega\epsilon\left(-\left(K+\frac{1}{2}\right)\omega_p, \left(K+\frac{1}{2}\right)\omega_p\right]$,

where $K \to \infty$ is a large positive integer. Then defining frequency vectors, $\underline{U}(\omega)$ and $\underline{Y}(\omega)$ for the input and output of the LPTV system respectively using (4.5), it can be shown that (4.2) can be expressed as the matrix relation $\underline{Y}(\omega) = \mathbb{H}(\omega)\underline{U}(\omega)$, $\omega\epsilon[-\frac{1}{2}\omega_p, \frac{1}{2}\omega_p)$. The $(2K+1) \times (2K+1)$ matrix, $\mathbb{H}(\omega)$, given by

$$\mathbb{H}(\omega) = \begin{bmatrix} H_{-K,-K}(\omega) & \cdots & \cdots & H_{-K,0}(\omega) & \cdots & \cdots & H_{-K,K}(\omega) \\ \vdots & \ddots & \vdots & \vdots & \vdots & \iddots & \vdots \\ \vdots & \cdots & H_{-1,-1}(\omega) & H_{-1,0}(\omega) & H_{-1,1}(\omega) & \cdots & \vdots \\ H_{0,-K}(\omega) & \cdots & H_{0,-1}(\omega) & H_{0,0}(\omega) & H_{0,1}(\omega) & \cdots & H_{0,K}(\omega) \\ \vdots & \cdots & H_{1,-1}(\omega) & H_{1,0}(\omega) & H_{1,1}(\omega) & \cdots & \vdots \\ \vdots & \iddots & \vdots & \vdots & \vdots & \ddots & \vdots \\ H_{K,-K}(\omega) & \cdots & \cdots & H_{K,0}(\omega) & \cdots & \cdots & H_{K,K}(\omega) \end{bmatrix} \tag{4.6}$$

is referred to as the conversion matrix (or the "*harmonic transfer matrix*" [30]) (of the LPTV system), and its elements are given by $H_{i,j}(\omega) = H_{i-j}(\omega + i\omega_p)$, i.e., just frequency shifted HTFs. It should be noted that $H_{i,j}(\omega)$ is the transfer functiion from the j^{th} frequency slice of the input, $u(t)$, to the i^{th} frequency slice of the output, $y(t)$.

By itself, (4.6) is just the matrix form of (4.2), and does not give any extra information. Nevertheless, we will show that for simple switching components the HTFs, and hence $\mathbb{H}(\omega)$ can be easily derived [34].

4.2.1 Basic LPTV Components

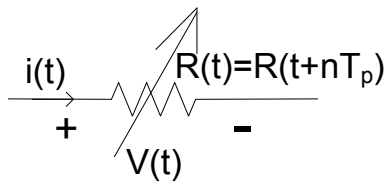

Figure 4.1: An LPTV resistor

Consider a linear periodically time varying resistor, $R(t)$, with period of variation, T_p as

shown in Fig. 4.1. By Ohm's law, the voltage, $v(t)$, and the current, $i(t)$, are related as $v(t) = R(t)i(t)$. Hence the Fourier transforms of $v(t)$ and $i(t)$ are related by a convolution:

$$V(\omega) = \int_{-\infty}^{\infty} I(\theta)R(\omega - \theta)d\theta \ . \tag{4.7}$$

where $R(\omega)$ is the Fourier transform of $R(t)$. Given that $R(t)$ varies in a periodic fashion with period T_p, $R(\omega)$ can be shown to be a set of impulses at $\omega = m\omega_p = 2\pi\frac{m}{T_p}$ with amplitudes R_m, where m is an integer, and R_m is the coefficient of $e^{jm\omega_p t}$ in the Fourier series expansion of $R(t)$:

$$R(\omega) = \sum_{m=-\infty}^{\infty} R_m \delta(\omega - m\omega_p) \ . \tag{4.8}$$

Consequently, the convolution in (4.7) can be replaced with a summation:

$$V(\omega) = \sum_{m=-\infty}^{\infty} I(\omega - m\omega_p)R_m \ . \tag{4.9}$$

Essentially, the Fourier transform of the current is translated in the frequency domain by integer multiples of ω_p, weighed by the Fourier series coefficients of $R(t)$ and summed. Assuming that all the voltages and currents in the circuit are bandlimited to within the frequency range $\left[-\left(K + \frac{1}{2}\right)\omega_p, \left(K + \frac{1}{2}\right)\omega_p\right]$, where K is a positive integer, it can be shown from (4.9) that the k^{th} frequency slice of $V(t)$ (defined as in (4.3)) is a weighted linear combination of the $2K + 1$ frequency slices of $i(t)$, weighed by the Fourier series coefficients of $R(t)$:

$$V_k(\omega) = \sum_{m=-K}^{K} I_{-m}(\omega)R_{m+k}, \ \forall\, k \,\epsilon\, \mathbb{Z}, \ |k| \leq K \ . \tag{4.10}$$

This is illustrated pictorially in Fig. 4.2. Note that the gaps in $I(\omega)$ and $V(\omega)$ seen in the figure are only to clarify the illustration and are not real.

The $2K + 1$ equations (for the $2K + 1$ frequency slices respectively) from (4.10) can be compactly represented using the frequency vectors of $V(t)$ and $i(t)$ as

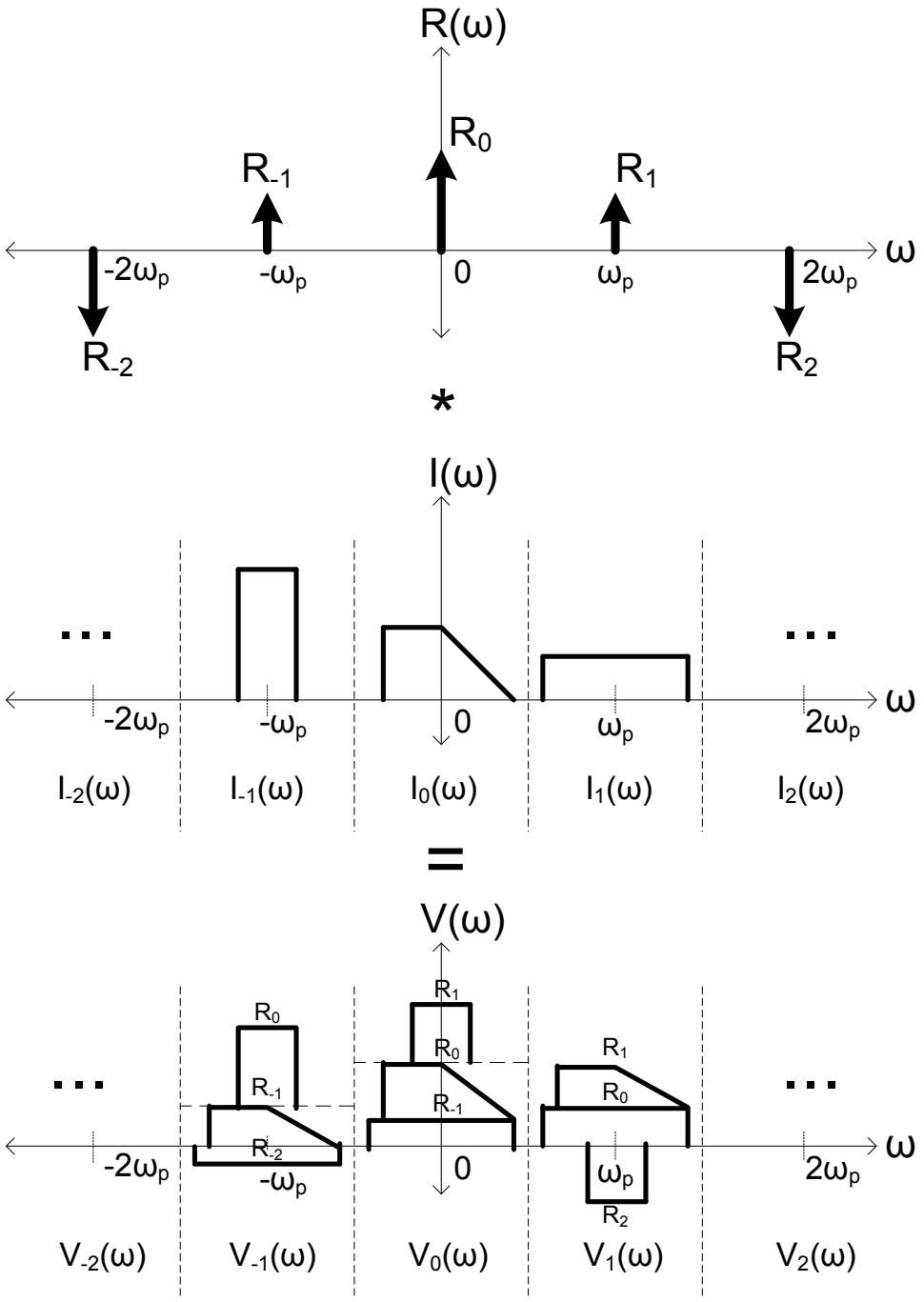

Figure 4.2: Voltage output of an LPTV resistor

$$\underline{V}(\omega) = \mathbb{R}\underline{I}(\omega), \text{ where} \tag{4.11}$$

$$\mathbb{R} = \begin{bmatrix} R_0 & \cdots & R_{-K} & \cdots & R_{-2K} \\ \vdots & \vdots & \vdots & \vdots & \vdots \\ R_K & \cdots & R_0 & \cdots & R_{-K} \\ \vdots & \vdots & \vdots & \vdots & \vdots \\ R_{2K} & \cdots & R_K & \cdots & R_0 \end{bmatrix}_{(2K+1)\times(2K+1)} .$$

The above equation can be pictorially represented by a frequency-domain equivalent circuit shown in Fig. 4.3. Accordingly, the matrix $\mathbb{R}$ is the conversion matrix of the LPTV resistor, $R(t)$. It contains only coefficients of the Fourier series expansion of $R(t)$ and for every value of K, it is a Toeplitz matrix with complex entries in general. Furthermore, since $R(t)$ is real, it will exhibit Hermitian symmetry. Note that if $R(t) = R_0$, a constant, then the LPTV resistance reduces to $\mathbb{R} = R_0\mathbb{I}$, where $\mathbb{I}$ is an identity matrix of the appropriate size. As expected, this would result in no frequency translations between the current and the voltage.

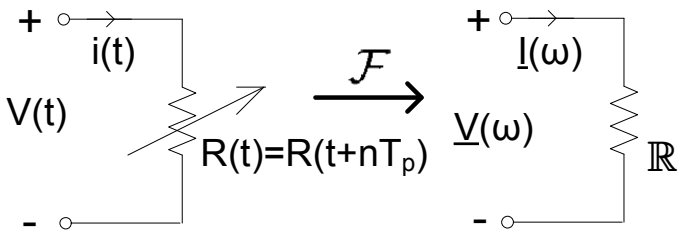

Figure 4.3: Frequency-domain equivalent circuit of LPTV resistor

Consider the example of a transistor switch turned ON and OFF by a clock signal of period T_p, shown in Fig. 4.4. This is a common component in many mixer and N-path circuits. For simplicity, assume that the clock signal is ideal with 50% duty cycle and zero transition times and that the transistor is a resistor of value R_{on} when ON and R_{off} when OFF, as shown in Fig. 4.4. The Fourier series coefficients of $R(t)$ can be shown to be $R_m = \frac{1}{m\pi}\left(R_{off} - R_{on}\right) sin\left(\frac{m\pi}{2}\right)$, and the DC component $R_0 = \frac{1}{2}\left(R_{on} + R_{off}\right)$. The LPTV resistance, $\mathbb{R}$, can now be readily found. For example, for $K = 1$,

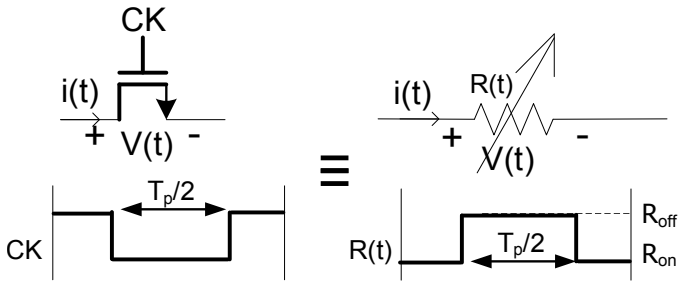

Figure 4.4: A switch driven by a periodic clock is an LPTV resistor

$$\mathbb{R} = \begin{bmatrix} \frac{1}{2}(R_{on}+R_{off}) & \frac{1}{\pi}(R_{off}-R_{on}) & 0 \\ \frac{1}{\pi}(R_{off}-R_{on}) & \frac{1}{2}(R_{on}+R_{off}) & \frac{1}{\pi}(R_{off}-R_{on}) \\ 0 & \frac{1}{\pi}(R_{off}-R_{on}) & \frac{1}{2}(R_{on}+R_{off}) \end{bmatrix}.$$

Consider the case where a constant current, i.e., $I(\omega) = I_0\delta(\omega)$ is driven through this switch. So, $\underline{I}(\omega) = [\ 0 \quad I_0\delta(\omega) \quad 0\ ]^T$ is the frequency vector of $i(t)$ and the frequency vector of $V(t)$ can be calculated using (4.11), which can be combined to form $V(\omega)$ as described in (4.4). Note that if a voltage (rather than a current) were applied, the resultant current frequency vector can be calculated in two ways. The transistor switch could be modeled as an LPTV conductance, $G(t)$, and proceeding analogously it can be shown that $\underline{I}(\omega) = \mathbb{G}\underline{V}(\omega)$ where $\mathbb{G}$ is another constant matrix, corresponding to the conversion matrix of the LPTV conductance. Else, (4.11) could simply be inverted i.e., $\underline{I}(\omega) = \mathbb{R}^{-1}\underline{V}(\omega)$. It is expected that the Hermitian symmetric Toeplitz matrix, $\mathbb{R}$, would be invertible for most practical scenarios, where $R(t) > 0$.

Note that the choice $K = 1$ in the above example, of course, ignores all harmonics and retains only the DC and fundamental terms. A small K is used for the sake of illustration but large values of K can be used. The relation between the voltage and current frequency vectors, (4.11), retains its form for any value of K. The sizes of the vectors and matrices simply increase with K. The added complexity is only in evaluating a larger LPTV resistance matrix, $\mathbb{R}$, or its inverse and no additional tedious algebra.

The algebraic similarity of $\underline{V}(\omega) = \mathbb{R}\underline{I}(\omega)$ or $\underline{I}(\omega) = \mathbb{G}\underline{V}(\omega)$ to traditional LTI circuit equations is not a coincidence. Similar relations can be found for every other linear period-

ically varying component, and as will be shown, they provide a very convenient means of extending many LTI theorems and analysis techniques to LPTV circuits. For example, consider a capacitor whose capacitance, $C(t)$, is varied periodically with a period T_p. Now the voltage and the current across the capacitor are related in the time and frequency domains by the following relations:

$$i(t) = C(t)\frac{dV(t)}{dt} \overset{\mathcal{F}}{\longleftrightarrow} I(\omega) = C(\omega) * j\omega V(\omega), \tag{4.12}$$

where $*$ is the convolution operator. Proceeding as in the resistance case, assuming that the voltage and current are bandlimited, and using the Fourier series expansion of $C(t)$, it can be shown that the k^{th} frequency slice of $V(t)$ is

$$I_k(\omega) = \sum_{m=-K}^{K} j(\omega - m\omega_p)V_{-m}(\omega)C_{m+k}, \tag{4.13}$$

where C_k is the coefficient of $e^{jk\omega_p t}$ in the Fourier series expansion of $C(t)$. In terms of the frequency slice vectors, it follows that

$$\underline{I}(\omega) = j\mathbb{C}\mathbf{\Omega}(\omega)\underline{V}(\omega), \tag{4.14}$$

where $\mathbf{\Omega}(\omega) = diag\ \{[\omega - K\omega_p \ \cdots \ \omega \ \cdots \ \omega + K\omega_p]\}$, and $\mathbb{C}$ is of the same structure as $\mathbb{R}$ in (4.11). Again, the relation $\underline{I}(\omega) = j\mathbb{C}\mathbf{\Omega}(\omega)\underline{V}(\omega)$ is remarkably similar to the Fourier domain relation for a capacitor namely, $I(\omega) = jC\omega V(\omega)$, except that $\underline{V}(\omega)$ and $\underline{I}(\omega)$ are vectors of frequency slices, $\mathbb{C}$ is a frequency-independent, Hermitian symmetric Toeplitz matrix determined by the periodic variation of $C(t)$ and ω is replaced by a diagonal matrix $\mathbf{\Omega}(\omega)$ that has no component information. The matrix $\mathbb{C}$ is hence the conversion matrix of the LPTV capacitor. Similar relations can be obtained for all other LPTV elements, a subset of which is reported in Table 4.1.

Component	LTI Relation	LPTV Relation	Illustration
Resistor	$V(\omega) = R\,I(\omega)$ $I(\omega) = R^{-1}V(\omega)$	$\underline{V}(\omega) = \mathbb{R}\underline{I}(\omega)$ $\underline{I}(\omega) = \mathbb{R}^{-1}\underline{V}(\omega)$	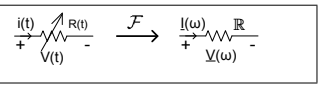
Capacitor	$I(\omega) = jC\omega V(\omega)$ $V(\omega) = -j\omega^{-1}C^{-1}I(\omega)$	$\underline{I}(\omega) = j\mathbb{C}\boldsymbol{\Omega}(\omega)\underline{V}(\omega)$ $\underline{V}(\omega) = -j\boldsymbol{\Omega}^{-1}(\omega)\mathbb{C}^{-1}\underline{I}(\omega)$	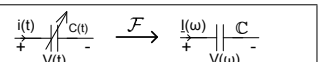
Inductor	$V(\omega) = jL\omega I(\omega)$ $I(\omega) = -j\omega^{-1}L^{-1}V(\omega)$	$\underline{V}(\omega) = j\mathbb{L}\boldsymbol{\Omega}(\omega)\underline{I}(\omega)$ $\underline{I}(\omega) = -j\boldsymbol{\Omega}^{-1}(\omega)\mathbb{L}^{-1}\underline{V}(\omega)$	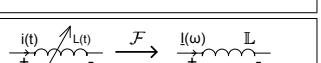
Controlled Source	$U_o(\omega) = \alpha U_i(\omega)$ $U_i(\omega) = \alpha^{-1}U_o(\omega)$	$\underline{U_o}(\omega) = \mathbb{A}\underline{U_i}(\omega)$ $\underline{U_i}(\omega) = \mathbb{A}^{-1}\underline{U_o}(\omega)$	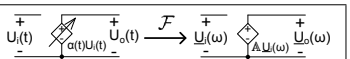
Series Combination	$V(\omega) = V_1(\omega) + V_2(\omega)$ $= (Z_1(\omega) + Z_2(\omega))\,I(\omega)$	$\underline{V}(\omega) = \underline{V_1}(\omega) + \underline{V_2}(\omega)$ $= (\mathbb{Z}_1(\omega) + \mathbb{Z}_2(\omega))\,\underline{I}(\omega)$	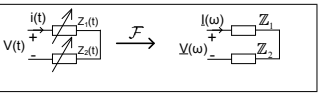
Parallel Combination	$I(\omega) = I_1(\omega) + I_2(\omega)$ $= (Y_1(\omega) + Y_2(\omega))\,I_1(\omega)$	$\underline{I}(\omega) = \underline{I_1}(\omega) + \underline{I_2}(\omega)$ $= (\mathbb{Y}_1(\omega) + \mathbb{Y}_2(\omega))\,\underline{V}(\omega)$	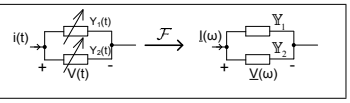

Table 4.1: Conversion matrix relations for basic LPTV components

4.2.2 Basic Circuit Theorems

We will now show that LTI circuit laws and theorems such as Kirchhoff's laws, series and parallel combinations etc. can also be readily extended to directly work with voltage and current frequency vectors. This will lead to a simplified analysis techniques for arbitrary LPTV circuits.

Consider Kirchhoff's current law (KCL) applied to a node connected to M branches, each carrying a current, $i_m(t),\ m = 1, 2, ...M$:

$$\sum_{m=1}^{M} i_m(t) = 0 \overset{\mathcal{F}}{\longleftrightarrow} \sum_{m=1}^{M} I_m(\omega) = 0. \tag{4.15}$$

Since the 2^{nd} equation in (4.15) is true for all ω, it follows that it is true for every frequency slice of width ω_p centered at $k\omega_p$:

$$\sum_{m=1}^{M} I_m(k\omega_p + \omega) = \sum_{m=1}^{M} I_{m,k}(\omega) = 0,\ \forall\, k\,\epsilon\,\mathbb{Z},\ -\frac{1}{2}\omega_p \leq \omega < \frac{1}{2}\omega_p, \tag{4.16}$$

where $I_{m,k}(\omega)$ is the k^{th} frequency slice of the m^{th} branch current. In other words, KCL is valid per frequency slice and all the per-slice equations in (4.16) can be compactly represented

as

$$\sum_{m=1}^{M} \underline{I_m}(\omega) = 0, \tag{4.17}$$

where $\underline{I_m}(\omega)$ is the LPTV vector representation of the m^{th} branch current. Note that (4.17) is valid, independent of how many slices $(2K+1)$ are considered in the LPTV vector definition, and is the conversion matrix extension of KCL. Proceeding in an exactly same manner, Kirchhoff's voltage law (KVL) can also be shown to hold for voltage frequency slice vectors. Similarly, extensions to the series and parallel impedance combination rules and other LTI circuit theorems such as superposition, duality, Thevenin's and Norton's theorems can also be derived, but are not proved here for the sake of brevity.

4.2.3 Circuit Analysis Using Conversion Matrices

We now show how the aforementioned extension rules can be used to analyze LPTV circuits. Consider the simple LPTV circuit shown in Fig. 4.5(a) wherein a voltage source drops its potential across a series combination of a constant load resistor and a transistor switch that is periodically turned ON and OFF as shown in Fig. 4.4.

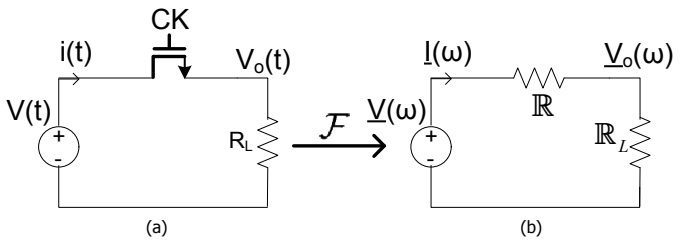

Figure 4.5: A simple switching circuit

As mentioned before, the transistor switch can be modeled as an LPTV resistor with LPTV resistance, $\mathbb{R}$, and a Fourier domain LPTV equivalent for the entire circuit can be readily derived, as shown in Fig. 4.5(b), where $\mathbb{R}_{\mathbb{L}} = R_L\mathbb{I}$ where $\mathbb{I}$ is an identity matrix. An expression for the frequency vector of the output voltage can be deduced readily from Fig. 4.5(b):

$$\underline{V_o}(\omega) = \mathbb{R}_{\mathbb{L}} \underline{I}(\omega) = \mathbb{R}_{\mathbb{L}} \left[\mathbb{R} + \mathbb{R}_L\right]^{-1} \underline{V}(\omega), \tag{4.18}$$

where the LPTV Ohm's law is applied for the load, then the LPTV series impedance combination rule is used, followed finally by LPTV Ohm's law on the series combination. Notice that the resulting expression is simply a matrix version of the familiar voltage divider rule. For given component values, the expression can be evaluated numerically to find the response of the circuit. For example, for $R_{on} = 0\Omega$, $R_{off} = 10\text{k}\Omega$, and $R_L = 50\Omega$, and for the case of an input that is bandlimited to only one frequency slice at DC, the calculated magnitude of $V_o(\omega)$ is plotted in Fig. 4.6. The plot only shows 21 frequency slices of $V_o(t)$ for the sake of brevity, but 1001 frequency slices ($K = 500$) were considered. The Fourier transform of the input and the Fourier transform of the calculated output are also plotted. Note that theoretically calculated frequency slices centered at DC and odd harmonics of the switching frequency, ω_p, show excellent agreement. Those at even harmonics are not exactly zero as expected, but are very small. It can be shown that they approach zero as the number of frequency slices is increased.

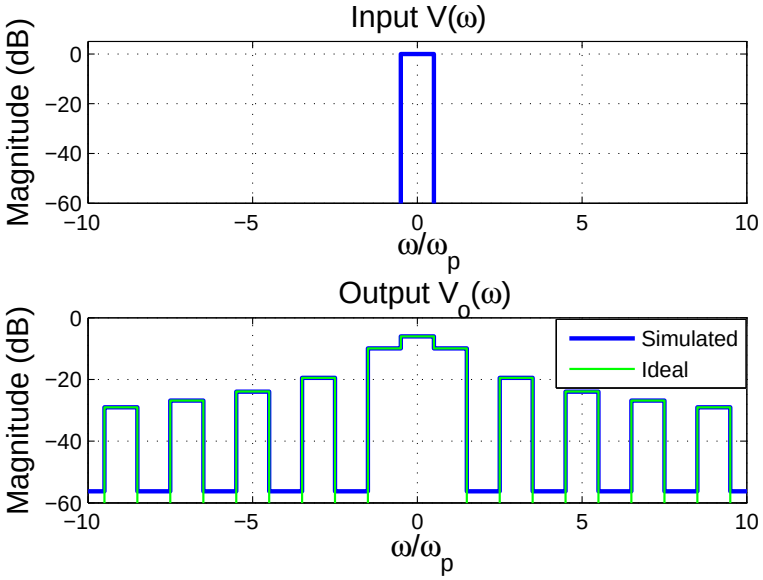

Figure 4.6: Response of the circuit in Fig. 4.5 to an input only in the frequency slice around DC

This example illustrates the potential of the proposed technique. Readers familiar with

basic circuit laws can write equations analogous to LTI circuits for LPTV circuits and manipulate them algebraically to derive desired results, as long as they are aware that the underlying circuit relations are vector-matrix relations. When applied to a general LPTV circuit, the LPTV analysis technique will result in closed form expressions that relate the frequency vector of some input, $u(t)$, and some output, $y(t)$: $\underline{Y}(\omega) = \mathbb{H}(\omega)\underline{U}(\omega)$, $\omega\epsilon[-\frac{1}{2}\omega_p, \frac{1}{2}\omega_p)$ as shown in (4.6). The $(2K+1)\times(2K+1)$ matrix, $\mathbb{H}(\omega)$, will be the conversion matrix of the considered LPTV circuit. Any element, $H_{i,j}(\omega)$, of the matrix is the transfer function from the frequency slice around the frequency, $j\omega_p$, of the input to the frequency slice around the frequency, $i\omega_p$, of the output as shown in (4.6). For example, $H_{0,0}(\omega)$ is the transfer function from the input's DC slice to the output's DC slice.

Note that the evaluation of resultant expressions, for example, (4.18) will typically involve multiple matrix inversions that can be performed numerically given component LPTV matrices. In certain special cases, symbolic (as opposed to numerical) inversion may also be possible considering that the component matrices are Toeplitz matrices with Hermitian symmetry. Another important benefit of the proposed approach is its ability in modeling non-idealities in component variations. For example, considering non-zero rise/fall times and duty cycle errors in the clock driving the transistor switch is as easy as changing the conversion matrices of the LPTV components such as $\mathbb{R}$.

4.2.4 Number of Frequency Slices

The aforementioned extension rules, the system conversion matrix, $\mathbb{H}(\omega)$, and any closed form expressions derived from the proposed analysis, for example, (4.18), retain their symbolic form independent of the number of frequency slices considered. However, their values depend on K. If it is known that every voltage and current in a given circuit are bandlimited, simply choosing a large enough K suffices. However, in many circuits, this may not be the case. Furthermore, signals that are not bandlimited, for example, white noise, may be present.

The proposed technique still provides an engineering solution in such situations in the sense that the solutions converge to the "*true*" solution as K approaches infinity. An outline

of the proof for the aforementioned example is offered along with numerical verification of convergence behavior.

In the example in Fig. 4.5, note that $\mathbb{X} = \mathbb{R} + \mathbb{R}_L$ is a $(2K+1) \times (2K+1)$ matrix, and to highlight the dependence on K explicitly, let us denote it as $\mathbb{X}_K$. Consider the sequence of matrices, $\{\mathbb{X}_K\}$. Now, each $\mathbb{X}_K$ is a Hermitian Toeplitz matrix since $\mathbb{R}$ is Hermitian Toeplitz matrix, and $\mathbb{R}_\mathbb{L}$ is an identity matrix scaled by R_L. Its elements can be shown to be the Fourier series coefficients of the periodic function, $x(t) \triangleq R_L + R(t) > 0$. It is well known (Lemma 4.5 in [38]) that if the elements of $\mathbb{X}_K$ are the Fourier series coefficients of a periodic function, $x(t) > 0$, that are absolutely summable, then (a) $\mathbb{X}_K$ is invertible, and (b) the sequence of inverses, $\left\{\mathbb{X}_K^{-1}\right\}$, is asymptotically equivalent to a convergent sequence of (inverses of) circulant matrices. Consequently, $\left\{\mathbb{X}_K^{-1}\right\}$ will converge and (4.18) will result in the solution as K approaches infinity.

The convergence in the case of the example in Fig. 4.5 is illustrated numerically in Fig. 4.7. The magnitude of $V_o(\omega)$ in four example frequency slices, centered at $\omega = 0$, ω_p, $2\omega_p$, and $9\omega_p$ are plotted as A_0, A_1, A_2, and A_9, respectively. As is evident, the DC component, the fundamental, and its odd harmonics converge; $K = 100$ seems to be sufficient. The even harmonics, which are expected to be completely absent ideally, are much smaller in magnitude and reduce steadily with increasing values of K.

We will now examine the use of the conversion matrix-based analysis technique for two common LPTV circuits – mixer-first receivers and N-path filters.

4.3 Mixer-First Receivers

Mixer-first receivers are promising candidates for widely programmable RF receiver front-ends. Figure 4.8(a) shows the schematic of a 4-path mixer-first receiver. Here, the RF input signal is downconverted by four switches that are controlled by clocks with 25% duty cycle with a period, T_p, as shown in the figure. The in-phase and quadrature-phase outputs are measured differentially between the nodes $V_{I+}(t)$ and $V_{I-}(t)$ and between the nodes $V_{Q+}(t)$ and $V_{Q-}(t)$ respectively. Its behavior can be readily analyzed using the conversion matrix

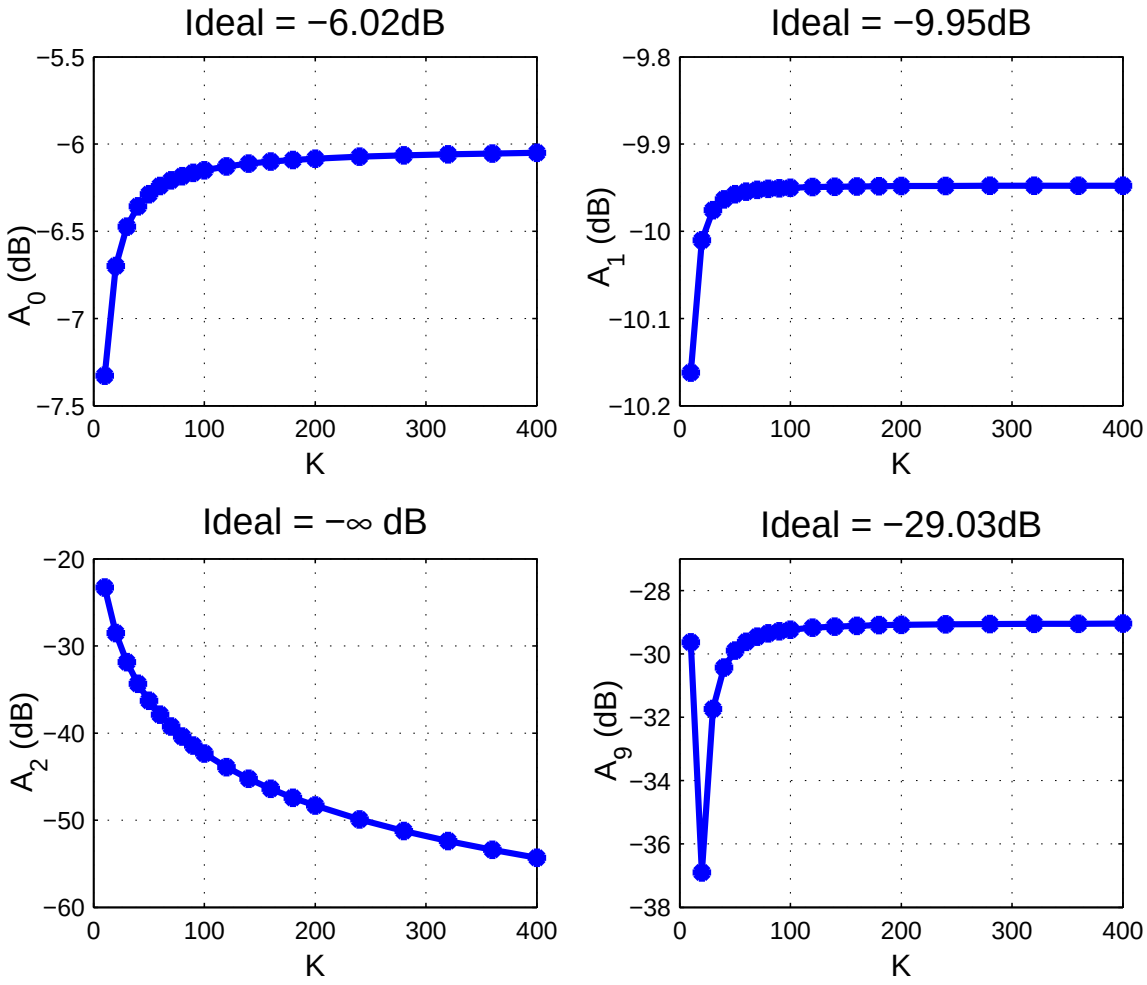

Figure 4.7: Convergence of output amplitudes with K

approach as shown below.

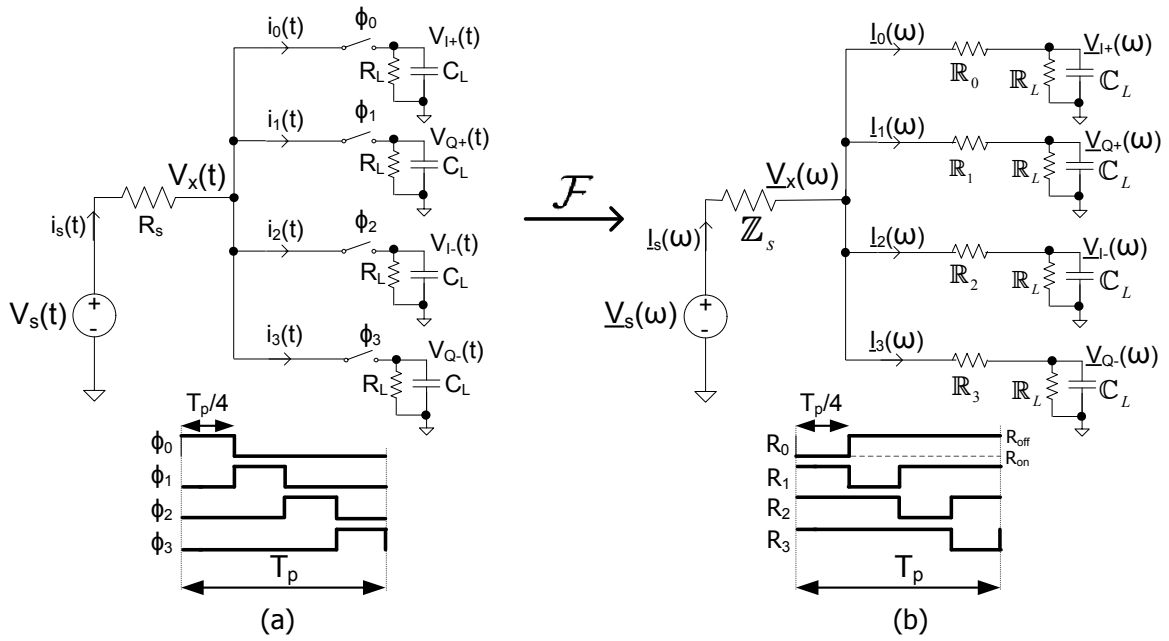

Figure 4.8: 4-path mixer-first receiver

Let $\mathbb{R}_n$ denote the conversion matrix of the LPTV resistance of the switch in the n^{th} branch. The resultant Fourier domain equivalent circuit is shown in Fig. 4.8(b) wherein the relevant node voltages and branch currents are labeled. It can be readily shown that the differential in-phase output voltage (its frequency vector, actually) is given by

$$\begin{aligned} \underline{V_I}(\omega) &= \mathbb{Z}_L \underline{I_0} - \mathbb{Z}_L \underline{I_2} \\ &= \mathbb{Z}_L \left[(\mathbb{R}_0 + \mathbb{Z}_L)^{-1} - (\mathbb{R}_2 + \mathbb{Z}_L)^{-1} \right] \underline{V_x}(\omega), \end{aligned} \tag{4.19}$$

where $\mathbb{Z}_L$ is the conversion matrix of the load impedance, i.e., $\mathbb{Z}_L = \left[R_L^{-1}\mathbb{I} + jC_L\mathbf{\Omega}(\omega) \right]^{-1}$, $\mathbb{I}$ being the identity matrix. Note that $\underline{V_x}$ can be obtained as a voltage divider between the conversion matrices of the source impedance, $\mathbb{Z}_s$, and the LPTV input impedance, $\mathbb{Z}_{in}$:

$$\underline{V_x}(\omega) = \mathbb{Z}_{in}(\omega) \left(\mathbb{Z}_s + \mathbb{Z}_{in}(\omega) \right)^{-1} \underline{V_s}(\omega), \tag{4.20}$$

where $\mathbb{Z}_s = R_s\mathbb{I}$. The conversion matrix of the LPTV input impedance can be shown, using series and parallel impedance combination rules, to be

$$\mathbb{Z}_{in}(\omega) = \left(\sum_{n=0}^{3} \left[\mathbb{R}_n + \mathbb{Z}_L \right]^{-1} \right)^{-1}, \tag{4.21}$$

The conversion matrix of the receiver, $\mathbb{H}(\omega)$, defined as $\underline{V_I}(\omega) = \mathbb{H}(\omega)\underline{V_s}(\omega)$, can be derived simply by substituting (4.21) in (4.20), and the result in (4.19). A similar expression can be found for the differential quadrature-phase output voltage. The components of $\mathbb{H}(\omega)$ give the required HTFs as shown in (4.6).

These expressions can be evaluated given numerical circuit components, as illustrated below for an example mixer-first receiver. Note that prior art [19, 20, 32] has already analyzed this circuit, but assuming ideal clocks i.e., no duty cycle errors, instantaneous clock transitions etc., arguably to render analysis complexity manageable. However, considering clock non-idealities is very easy in the proposed technique: only the LPTV resistance matrices, $\mathbb{R}_n$, needs to be altered according to the actual resistance variation, but the expressions derived above remain the same. To illustrate, an example case of resistance variation due to non-zero clock transition widths is considered here, characterized by the parameter β, as shown in Fig. 4.9. The ideal case is represented by $\beta = 0$.

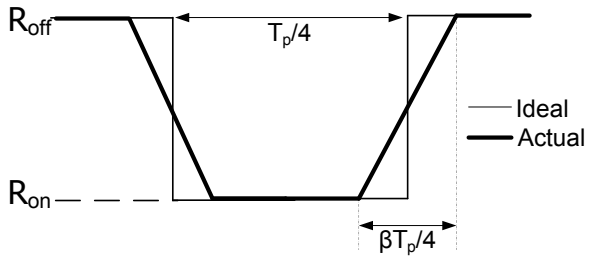

Figure 4.9: Non-ideal clock-edge model

Assuming an OFF resistance, R_{off}, an ON resistance, R_{on}, $\mathbb{R}_n$ can be found from the corresponding periodic resistance variation, $R_n(t)$ (ideally varying as shown in Fig. 4.8(b)). Then the coefficient of $e^{jm\omega_p t}$ in the Fourier series of $R_n(t)$ can be found as $R_{n,m} = R_{n,m,ideal} + \triangle R_{n,m}$, where

$$\begin{aligned} R_{n,m,ideal} &= \frac{1}{m\pi}\left(R_{off} - R_{on}\right) sin\left(\frac{3m\pi}{4}\right) exp\left(-\frac{j\pi mn}{2}\right), \\ \Delta R_{n,m} &= \frac{1}{m\pi}\left(R_{off} - R_{on}\right) sin\left(\frac{m\pi}{4}\right) exp\left(-\frac{j\pi mn}{2}\right) \left[1 - \frac{4}{m\pi\beta} sin\left(\frac{m\pi\beta}{4}\right)\right], \end{aligned}$$

with $R_{n,0,ideal} = \frac{3}{4}(R_{off} - R_{on}) + R_{on}$, and $\Delta R_{n,0} = 0$. Note that the error term, $\triangle R_{n,m}$, appears due to non-zero β.

In the following, let $R_{off} = 10\text{k}\Omega$, $R_{on} = 0\Omega$, $R_s = 50\Omega$, $R_L = \frac{\pi^2}{2}R_s$ and switching frequency $\omega_p = 2\pi/T_p$ be such that $\omega_p/\omega_{RC} = 50$, where $\omega_{RC} = 1/R_sC_L$. A value of $K = 1000$ was used in (4.6) for constructing all conversion matrices. For Cadence simulations, the switches were modeled as periodically varying resistors using Verilog-A.

4.3.1 Frequency Response

The frequency slice vector of the in-phase output, $\underline{V_I}(\omega)$, is calculated using (4.19)-(4.21), the slices combined to obtain $V_I(\omega)$ according to (4.4), and the magnitude of the result is plotted in Fig. 4.10. An input spanning the frequency slices centered around the fundamental switching frequency was used and ideal clock edges were assumed. Note that the downconverted output appears around DC and is shaped by the roll-off due to the capacitor at the output node, exactly as expected and predicted by prior art.

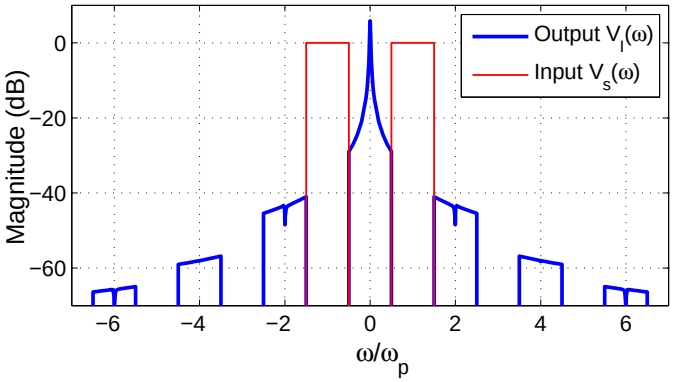

Figure 4.10: Receiver response to an input applied only in the frequency slices around $\pm\omega_p$

4.3.2 Downconversions

Mixer-first receivers are also known to downconvert frequency slices around odd harmonics of the switching frequency, $n\omega_p$, where n is an odd integer, to around DC. To confirm, the calculated magnitude of the function of HTFs, $H_n(\omega) + H_{-n}(\omega)$, which is the effective

transfer function from the input frequency slices around $\pm n\omega_p$ to output's DC slice, is plotted in Fig. 4.11 for odd integers n for the ideal clock case i.e., $\beta = 0$. The plots are in good agreement with prior art. The calculated effect of non-zero width clock transitions on the downconversion from $\pm\omega_p$ is plotted in Fig. 4.12 for two values of β. In the absence of prior art, the calculations are compared against Cadence SPECTRE PSS-PAC simulations, again showing excellent agreement.

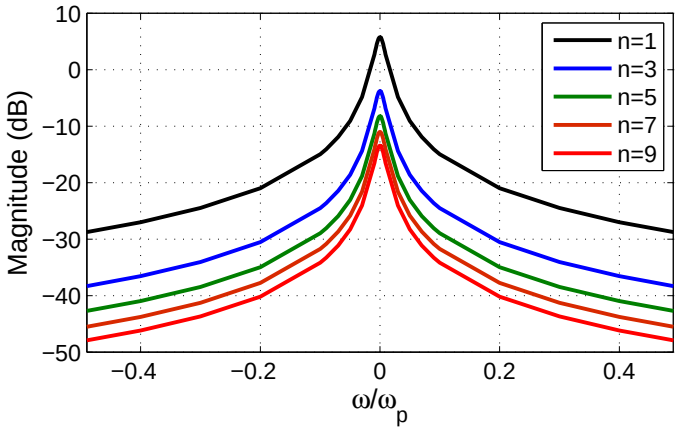

Figure 4.11: Receiver output around DC to an input applied only in the frequency slices around $\pm n\omega_p$ (as shown in Fig. 4.10)

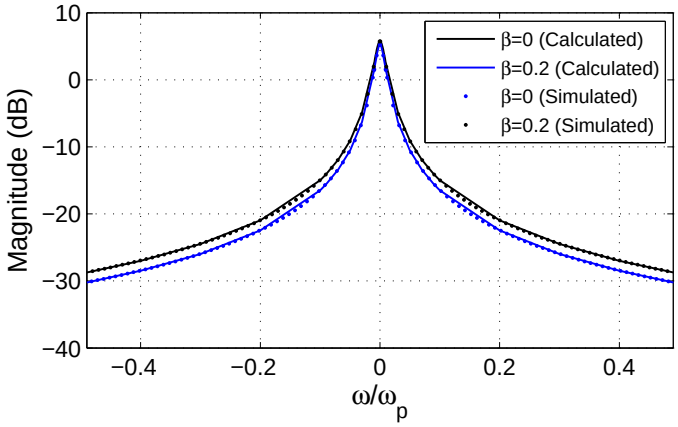

Figure 4.12: Receiver response around DC to an input applied only in the frequency slices around $\pm\omega_p$ in the case of imperfect clock edges

4.3.3 Noise Figure

Since the proposed technique calculates all HTFs, it is straightforward to calculate the noise figure degradation due to folding of noise from the source resistor. The double-sideband noise figure (DSB NF), considering up to M harmonics at an offset of ω from ω_p, is

$$NF(\omega) = \frac{\sum_{n=-M}^{M} |H_n(\omega)|^2}{|H_1(\omega)|^2 + |H_{-1}(\omega)|^2} \ . \tag{4.22}$$

Considering $\beta = 0$, and up to 51 harmonics of the switching frequency, the calculated noise figure is $1.2272 = 0.889dB$, and is flat across the band as is expected for noise from source resistor, comparing very well with predictions from prior art [21].

4.3.4 Input Impedance

The input impedance offered by the receiver is important for proper matching at the RF interface, especially when driven directly by the antenna. We showed how the conversion matrix for the input impedance matrix, $\mathbb{Z}_{in}(\omega)$, could be easily calculated in (4.21). Its diagonal entries, i.e., the HTF $Z_{in,0}(\omega)$, give the input impedance. The calculated values around the switching frequency are plotted in Fig. 4.13 for the ideal case. At exactly the switching frequency, the calculated input impedance is purely real and near 50Ω. This is in excellent agreement with prior art, which predicts a value of $\frac{2}{\pi^2}R_L$ (50Ω in this example) for ideal clocks and ideal switches, i.e., $R_{on} = 0$ and $R_{off} \to \infty$.

Fig. 4.14 plots the calculated effect of non-zero clock transition times on the input impedance, and compares it with values simulated using Cadence SPECTRE PSS-PAC simulations. Note that even a small transition width (e.g., $\beta = 0.01$) causes about 20% higher input impedance. As mentioned before, prior art has been unable to predict this effect, highlighting the value of the proposed analysis technique.

The effect of parasitic elements can also be easily included in the analysis. For example, suppose a parasitic capacitance, $C_p = \alpha C_L$, appears at the intermediate node, V_x, in Fig. 4.8(a), i.e., in parallel to receiver. To account for it, $\mathbb{Z}_{in}(\omega)$ in (4.20) just needs to be altered

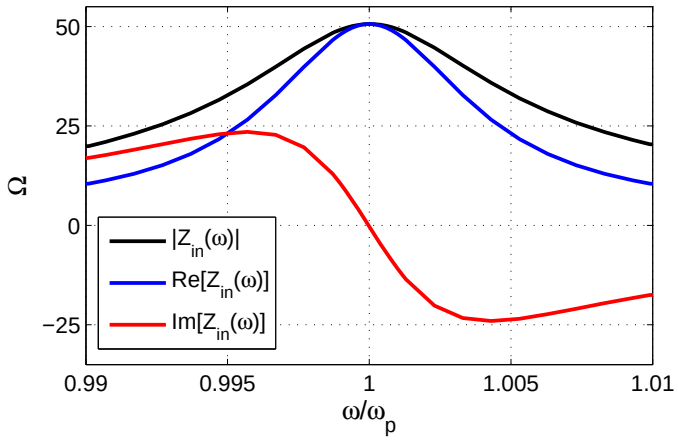

Figure 4.13: Receiver input impedance around the switching frequency, ω_p

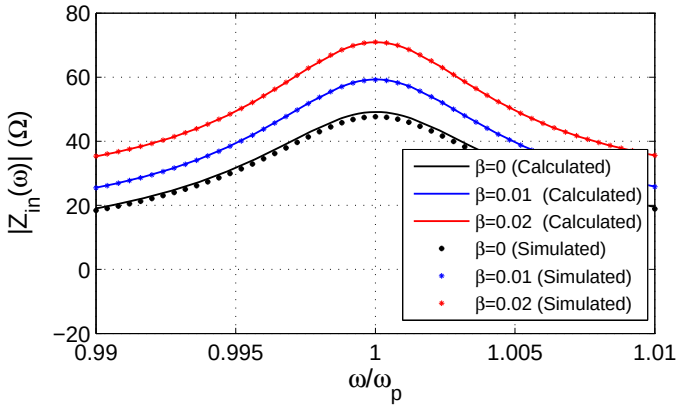

Figure 4.14: Receiver input impedance around the switching frequency, ω_p, in the case of imperfect clock edges

to

$$\mathbb{Z}_{in}(\omega) = \left(\mathbb{Y}_p + \sum_{n=0}^{3} [\mathbb{R}_n + \mathbb{Z}_L]^{-1} \right)^{-1}, \tag{4.23}$$

where $\mathbb{Y}_p = jC_p\mathbf{\Omega}(\omega)$. With this modification, the effects of C_p can be easily studied. For example, the effect of C_p on the receiver input impedance around ω_p is shown in Fig. 4.15, along with simulation results using Cadence SPECTRE PSS-PAC. Notice how a parasitic C_p of even 0.2% of the load capacitance, C_L, can reduce the input impedance by about 10%. A slight shift in the peak of the impedance curve can also be observed. Similarly, to consider a complex source impedance, only $\mathbb{Z}_s$ in (4.20) needs to be changed.

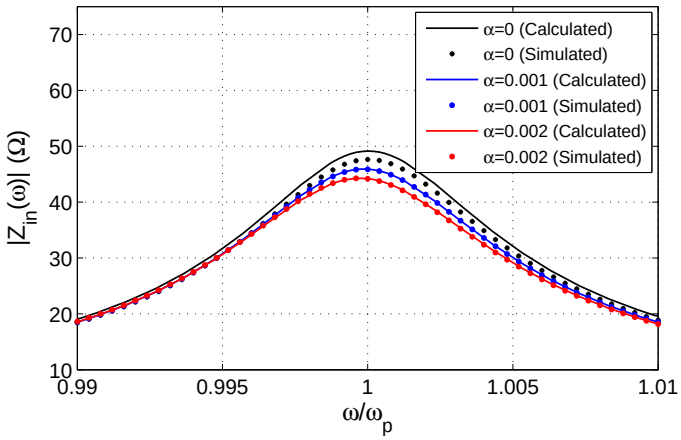

Figure 4.15: Receiver input impedance around the switching frequency, ω_p, with parasitic capacitance

4.4 *N*-Path Filters

N-path filters were first proposed in [23]. The concept is simple: if a high-frequency RF input signal is first downconverted to around DC, passed through a low-pass filter, and then upconverted back to RF, then the input effectively sees a band-pass filter response. A simple implementation of this concept, the differential band-pass *N*-path filter is shown in Fig. 4.16(a) [16] (the differential filter is preferred over the single-ended version as it rejects DC and even harmonics of the switching frequency). The differential RF voltage

input is connected though source resistors to a set of N parallel switched capacitor loads in succession, with the switches controlled by non-overlapping clocks with an ideal duty cycle of $\frac{1}{N}$, and a period, T_p, as shown in the figure. The number of paths, N, is even, and two paths are active at any one instant of time via the closing of two switches so that both ends of the differential input as connected to a load capacitor. The load capacitors, C, are chosen such that the bandwidth $2/NR_sC$ (the effective resistor seen by each capacitor is $NR_s/2$ due to the duty cycling) is much smaller than ω_p. The switches essentially downconvert and upconvert signals, while the resistor-capacitor combination behaves like a low-pass filter. The differential output voltage is then measured between the nodes $V_{o+}(t)$ and $V_{o-}(t)$ (the common nodes for the switches), and exhibits a band-pass response. This circuit can be easily analyzed using conversion matrices.

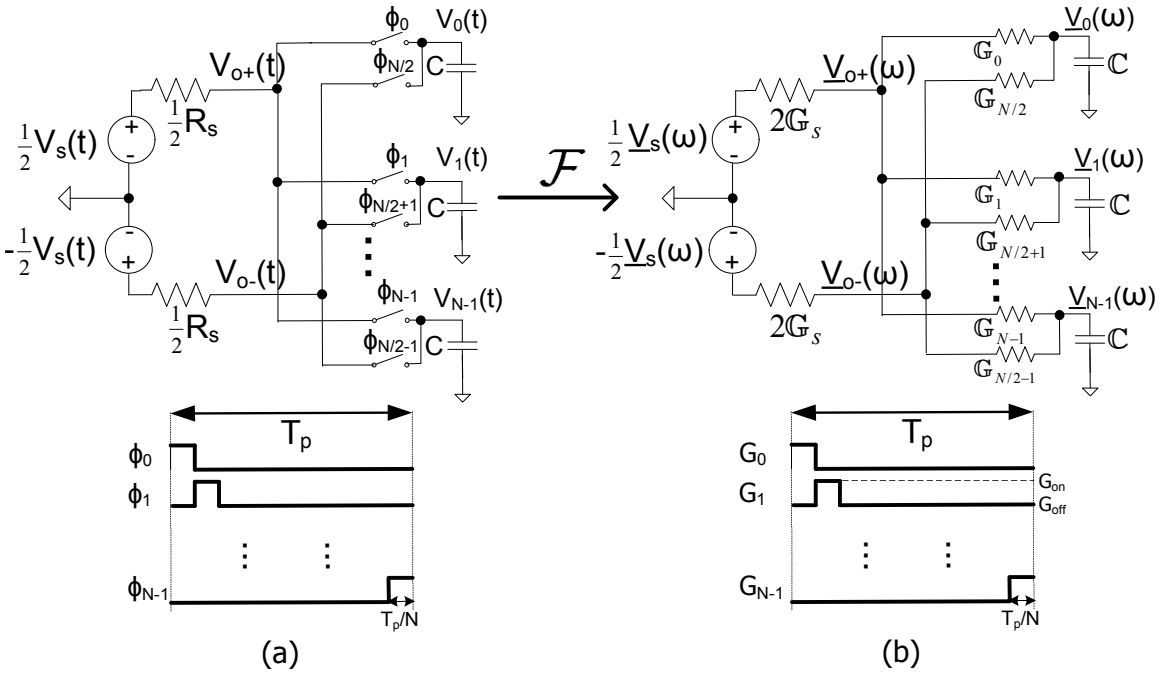

Figure 4.16: The differential band-pass N-path filter

Let $\mathbb{G}_i$ denote the conversion matrix of the LPTV conductance of the switch in the i^{th} branch, $\mathbb{G}_s = R_s^{-1}\mathbb{I}$ represent the source conductance, and $\mathbb{Y}_L = jC\mathbf{\Omega}(\omega)$ denote the LPTV capacitor admittance. The resultant Fourier domain equivalent circuit is shown in Fig. 4.16(b) wherein the relevant node voltages and branch currents are labeled. By applying KCL at the node in the i^{th} branch, its voltage, $\underline{V_i}$, is given by:

$$\underline{V_i}(\omega) = (\mathbb{G}_i + \mathbb{G}_j + \mathbb{Y}_L)^{-1} \left(\mathbb{G}_i \underline{V_{o+}}(\omega) + \mathbb{G}_j \underline{V_{o-}}(\omega) \right), \tag{4.24}$$

where $j = \left(i + \frac{N}{2}\right) \bmod N$. Similarly, applying KCL at the positive terminal of the differential output, i.e., $\underline{V_{o+}}$, gives

$$\underline{V_{o+}}(\omega) = \left(2\mathbb{G}_s + \sum_{i=0}^{N-1} \mathbb{G}_i \right)^{-1} \left[\mathbb{G}_s \underline{V_s}(\omega) + \sum_{i=0}^{\frac{N}{2}-1} \left(\mathbb{G}_i \underline{V_i}(\omega) + \mathbb{G}_j \underline{V_j}(\omega) \right) \right]. \tag{4.25}$$

The voltage at the negative terminal of the output, $\underline{V_{o-}}$, can be obtained in exactly the same manner. Hence, the total output differential voltage, $\underline{V_o} = \underline{V_{o+}} - \underline{V_{o-}}$, is given by

$$\begin{aligned} \underline{V_{o+}}(\omega) - \underline{V_{o-}}(\omega) \quad = \quad & \left(2\mathbb{G}_s + \sum_{i=0}^{N-1} \mathbb{G}_i \right)^{-1} \left[2\mathbb{G}_s \underline{V_s}(\omega) + \right. \\ & \left. \sum_{i=0}^{\frac{N}{2}-1} (\mathbb{G}_i - \mathbb{G}_j) \left(\underline{V_i}(\omega) - \underline{V_j}(\omega) \right) \right]. \end{aligned}$$

Substituting the value of $\underline{V_i}(\omega) - \underline{V_j}(\omega)$ (with expressions for $\underline{V_i}$ and $\underline{V_j}$ obtained using (4.24)), and simplifying, the final output is given by

$$\begin{aligned} \underline{V_o}(\omega) = \quad & 2 \left[2\mathbb{G}_s + \sum_{i=0}^{N-1} \mathbb{G}_i - \sum_{i=0}^{\frac{N}{2}-1} \left\{ (\mathbb{G}_i - \mathbb{G}_j) \right. \right. \\ & \left. \left. (\mathbb{G}_i + \mathbb{G}_j + \mathbb{Y}_L)^{-1} (\mathbb{G}_i - \mathbb{G}_j) \right\} \right]^{-1} \mathbb{G}_s \underline{V_s}(\omega). \end{aligned} \tag{4.26}$$

Thus, the LPTV transfer function, $\mathbb{H}(\omega)$, defined as $\underline{V_o}(\omega) = \mathbb{H}(\omega)\underline{V_s}(\omega)$ is obtained. The components of $\mathbb{H}(\omega)$ give the required HTFs $\{H_n(\omega)\}$ as shown in (4.6).

These expressions can be evaluated given numerical circuit components, as illustrated below for an example filter. Note that these expressions are completely general, and do not put any restrictions, such as ideal or non-overlapping clocks. Considering clock non-idealities is very easy in the proposed technique: only the LPTV conductance matrices, $\mathbb{G}_i$, needs to be altered according to the actual resistance variation. To illustrate, consider the case of duty-cycle variation in the clocks. In the ideal case, all the clocks have a duty cycle of $\frac{1}{N}$, but suppose the actual duty cycle of the clocks is $\frac{1}{N}(1-\beta)$ ($\beta = 0$ being the ideal case). Note that a negative β implies that the clocks are overlapping. Assuming an OFF conductance, G_{off},

and an ON conductance, G_{on}, $\mathbb{G}_i$ can be found from the corresponding periodic conductance variation, $G_i(t)$ (shown in Fig. 4.16(b)). The coefficient of $e^{jm\omega_p t}$ in the Fourier series of $G_i(t)$ is

$$G_{i,m} = \frac{1}{m\pi}\left(G_{on} - G_{off}\right) sin\left(\frac{(1-\beta)m\pi}{N}\right) exp\left(-j\frac{2\pi im}{N}\right), \tag{4.27}$$

with $G_{i,0} = \frac{1-\beta}{N}(G_{on} - G_{off}) + G_{off}$.

In the following, let $G_{on}/G_{off} = 10^5$, and switching frequency $\omega_p = 2\pi/T_p$ be such that $\omega_p/\omega_{RC} = 31.4$ (similar to [16] for direct comparison), where $\omega_{RC} = 2/NR_sC$. A value of $K = 2000$ was used in (4.6) for constructing all conversion matrices. All simulation results are from Cadence SPECTRE PSS-PAC simulations, where the switches were modeled as periodically varying conductors using Verilog-A (unless specified).

4.4.1 Frequency Response

The HTFs, $\{H_n(\omega)\}$, give the frequency response of the circuit, and can be easily obtained from the entries of $\mathbb{H}(\omega)$. Thus, the magnitudes of the HTFs of a differential 4-path filter with ideal clock edges and extremely small switch resistance ($G_{on}R_s/2 = 10^3$) were calculated, and are shown in Fig. 4.17. These compare very well with results from prior art [16].

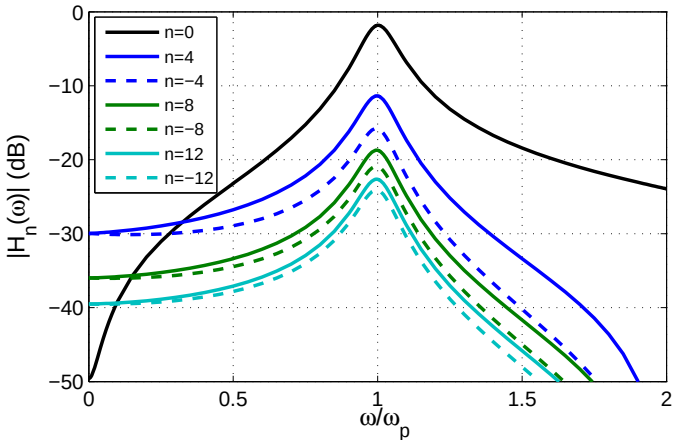

Figure 4.17: Magnitude of HTFs $\{H_n(\omega)\}$ for a 4-path filter around the switching frequency

These responses (except $H_o(\omega)$) can be regarded as folding responses of the filter, while

$H_0(\omega)$ represents the filter response. This occurs as the output is essentially "sampled" with a sampling period of T_p/N. Hence, inputs at frequencies $kN\omega_p + \omega$ (k is an integer) fold on top of each other due to aliasing. Thus to reduce this folding, N has to be increased (ideally to infinity). However, this comes at the cost of reduced filtering of the harmonics, i.e., harmonic rejection, in $H_0(\omega)$. To confirm, the calculated magnitude of $H_0(\omega)$ is plotted in Fig. 4.18 for $N = 4$ and 8. The values are again in excellent agreement with prior art [16].

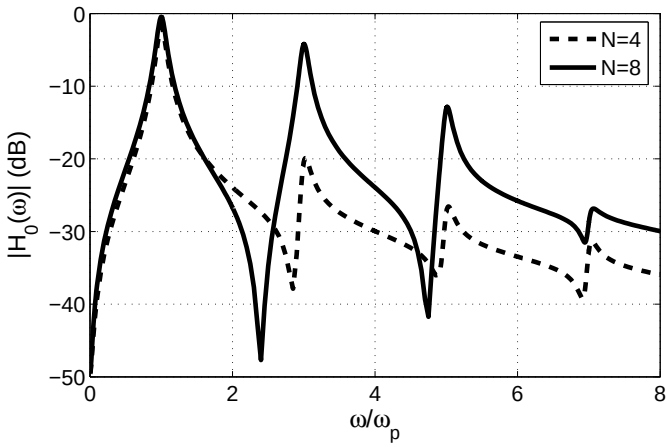

Figure 4.18: Magnitude of $H_0(\omega)$ for $N = 8$ vs. $N = 4$

4.4.2 Impact of Non-Idealities

4.4.2.1 Switch ON Resistance

It is well known that the switch ON resistance, $1/G_{on}$, limits filter attenuation [16]. This can be simply understood as follows: far from the filter center frequency, the capacitors have zero impedance. Hence the maximum attenuation is $\approx -20\log_{10}\left[(1/G_{on})\,/\,(1/G_{on} + R_s/2)\right] = 20\log_{10}\left[1 + G_{on}R_s/2\right]$. The calculated filter response, $H_0(\omega)$, plotted in Fig. 4.19 agrees with this intuition, and matches with simulation results.

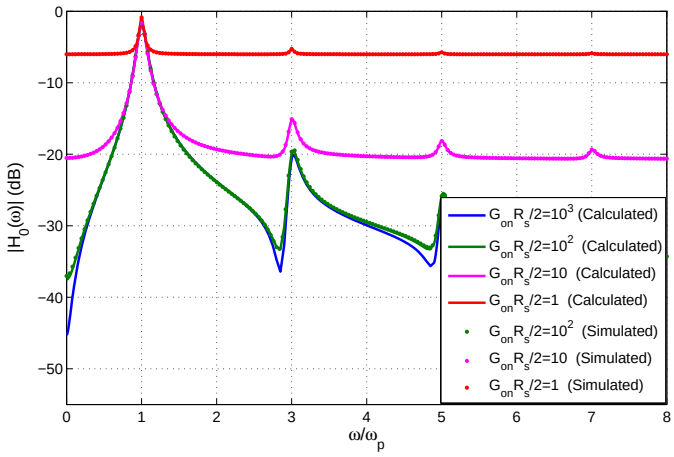

Figure 4.19: Magnitude of $H_0(\omega)$ for varying switch G_{on}

4.4.2.2 Non-ideal Duty Cycle Clocks

The effect of non-ideal duty cycle clocks (which may even introduce clock overlaps) on $H_0(\omega)$ can be easily studied by using non-zero values of β. Fig. 4.20 shows the calculated $H_0(\omega)$ for two values of β, alongside simulation results from verifying them. For $\beta = 0.2$, i.e., the case where all the switches are OFF for a certain period of time, the filtering response still retains a few peaks, but filter attenuation reduces to about 15dB. In the case of $\beta = -0.2$, i.e., overlapping clocks, the filtering response has completely degraded. This is a well known empirical result and occurs due to charge sharing between the load capacitors, but was not predicted by prior art.

It's also interesting to see how the extent of degradation in $H_0(\omega)$ in case of overlapping clocks actually depends on the switch ON resistance. Fig. 4.21 shows the calculated and simulated $H_0(\omega)$ for various values of switch ON conductance, G_{on}. It can be readily noted that the degradation is worse for higher values of G_{on}. This is intuitive as higher switch ON resistance reduces the extent of charge sharing between load capacitors. Of course, this comes at the expense of lower filter attenuation due to lower G_{on} as seen in Fig. 4.19. Again, this was not predicted in prior art, and was only known from simulations [16].

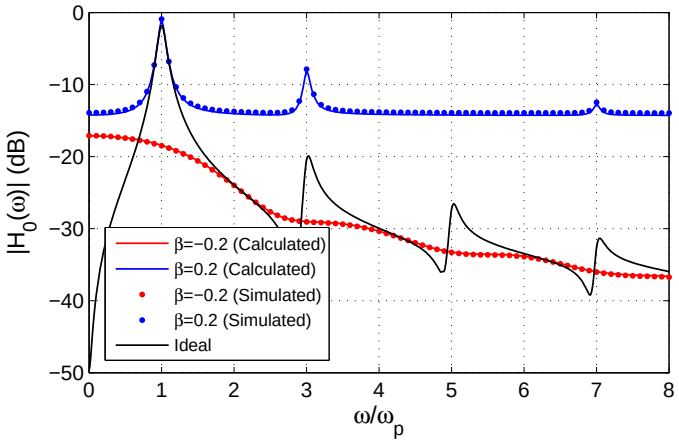

Figure 4.20: Magnitude of $H_0(\omega)$ for a 4-path filter in the case of imperfect duty-cycle clocks

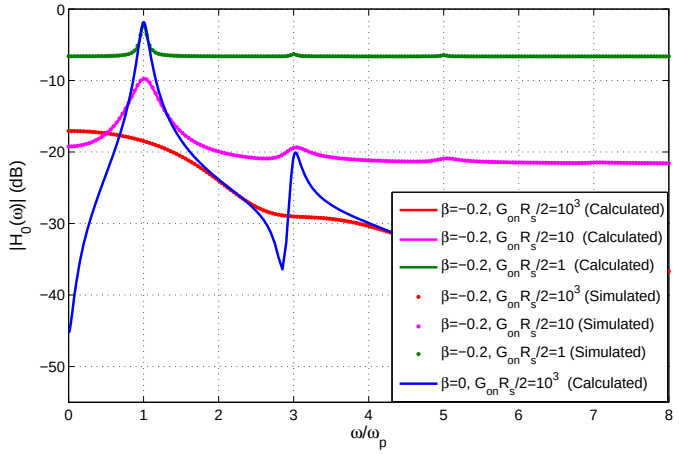

Figure 4.21: Magnitude of $H_0(\omega)$ with overlapping clocks and varying switch G_{on}

4.4.2.3 Switch Parasitic Capacitance

We can also consider parasitic elements. For example, if the switches introduce parasitic capacitors C_p at nodes V_{o+} and V_{o-} in the circuit, the final output can be easily shown to be

$$\begin{aligned}\underline{V_o}(\omega) = \quad & 2\Bigg[2\mathbb{G}_s + \mathbb{Y}_p + \sum_{i=0}^{N-1}\mathbb{G}_i - \sum_{i=0}^{\frac{N}{2}-1}\Big\{(\mathbb{G}_i - \mathbb{G}_j) \\ & (\mathbb{G}_i + \mathbb{G}_j + \mathbb{Y}_L)^{-1}(\mathbb{G}_i - \mathbb{G}_j)\Big\}\Bigg]^{-1}\mathbb{G}_s\underline{V_s}(\omega),\end{aligned} \tag{4.28}$$

where $\mathbb{Y}_p = jC_p\mathbf{\Omega}(\omega)$. Note that (4.28) is exactly the same as (4.26) with the exception of the presence of $\mathbb{Y}_p$. If we denote $C_p = \alpha C$, then the calculated and simulated filter responses are shown in Fig. 4.22. Notice that the filter gain and center frequency has degraded when C_p is just 10% of the load capacitance, C. This is an important result that is yet to be mentioned in prior art (and in fact limits the sizes of switches that can be used, and hence G_{on}).

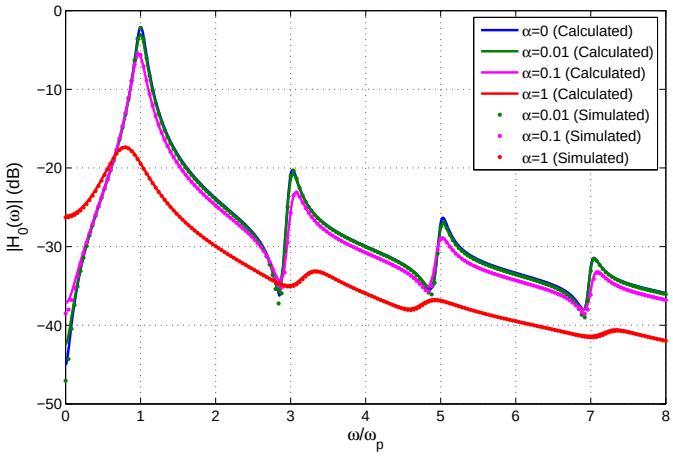

Figure 4.22: Magnitude of $H_0(\omega)$ with parasitic capacitors

4.4.3 Practical Switches

Finally, the switches were also implemented (in schematic) using TSMC 65-nm CMOS process as transmission gates consisting of a PMOS and an NMOS transistor with $w/L = 0.5\mu$m/60nm, and M fingers each, biased at $V_{dd}/2$, and driving $C = 50$pF. They are driven

by non-overlapping clocks operating at 500MHz with linear rising/falling edges lasting 50ps each and swinging from 0 to $V_{dd} = 1.2$V. For calculations, the switch parasitics and conductance variations were obtained from simulations (their Fourier coefficients were calculated using FFTs). The simulated and calculated results for various values of M are shown in Fig. 4.23, and clearly show the trade-off between filter attenuation and gain at center frequency due to G_{on} and C_p, respectively.

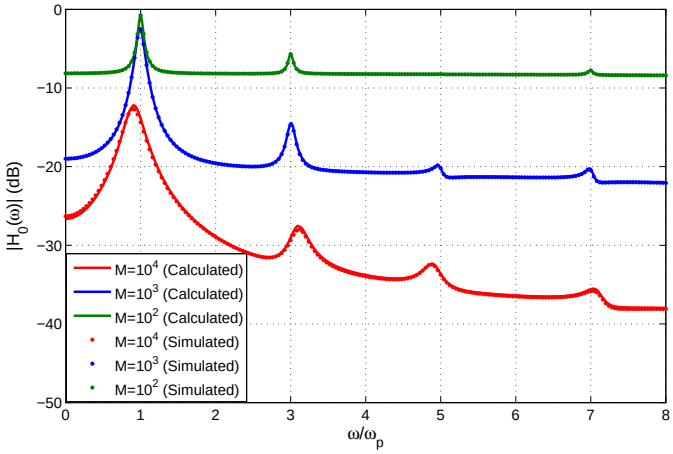

Figure 4.23: Magnitude of $H_0(\omega)$ with practical switches

CHAPTER 5

Impedance Matching in LPTV Circuits

5.1 Introduction

LPTV circuits such as N-path filters, mixer-first receivers and the FA-based receiver front-ends in Chapters 2 and 3 are excellent candidates for reconfigurable receivers. To maximize receiver programmability, such LPTV circuits are being pushed ever-closer to the antenna interface [14, 18, 19]. In fact, the mixer-first receiver topology directly connects the antenna input to a passive mixer, and achieves high linearity due to the high-Q band-pass impedance realized by the frequency-translation of the baseband input impedance to RF [19]. Hence it is important to understand how these circuits interact with the antenna.

In conventional LTI receivers, antenna interactions can be characterized using its S_{11} alone. This is because incident and reflected waveforms at the receiver input will be at the same frequency due to its LTI nature. However in LPTV circuits this is not the case due to the inherent frequency translations. Hence a traditional LTI S_{11} measurement may not be sufficient. However, in most works it is assumed that matching the input impedance of the LPTV circuit to the antenna impedance (usually 50Ω) is sufficient (similar to LTI circuits) [14, 19]. Further, the S_{11} itself is not generally derived. Thus, a more general framework to characterize antenna interactions is necessay to ensure that such assumptions are valid.

Chapter 4 showed that conversion matrices allow systematic analysis of LPTV circuits compared to other methods. Hence it can be easily applied to study the interaction of LPTV receiver front-ends with the antenna. This chapter develops a general framework to characterize antenna interactions based on conversion matrices.

5.2 S_{11} in an LPTV System

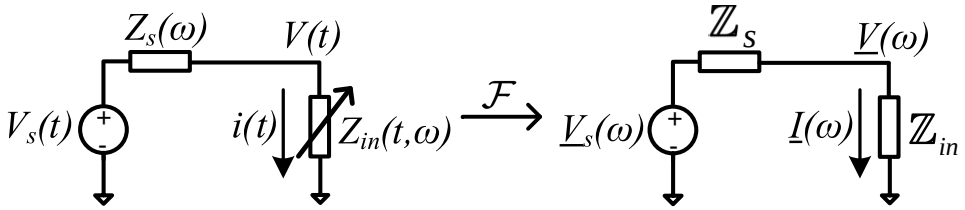

Figure 5.1: Input interface of a general LPTV circuit with time-varying input impedances, and its frequency-domain equivalent circuit

Consider an LPTV system shown in Fig. 5.1 where the source $V_s(t)$, with an LTI impedance, $Z_s(\omega)$, is terminated in a circuit whose frequency-dependent impedence is periodically time-varying, i.e., $Z_{in}(t,\omega) = Z_{in}(t+T_s,\omega)$. The conversion matrix method can be easily applied to analyze this LPTV circuit using the frequency-domain equivalent circuit shown in Fig. 5.1. The source and input impedances are represented by their conversion matrix equivalents, $\mathbb{Z}_s(\omega)$ and $\mathbb{Z}_{in}(\omega)$, respectively, with $\mathbb{Z}_s(\omega)$ being a diagonal matrix due to its time-invariant nature. Note that the source impedance is usually considered to be a resistor, R_s, and so $\mathbb{Z}_s(\omega) = R_s\mathbb{I}$, where $\mathbb{I}$ is the identity matrix. The frequency vectors of the voltage, $V(t)$, and current, $i(t)$, across the load can then be derived as:

$$\begin{aligned} \underline{V}(\omega) &= \mathbb{Z}_{in}(\omega)[\mathbb{Z}_s(\omega) + \mathbb{Z}_{in}(\omega)]^{-1}\underline{V_s}(\omega), \\ \underline{I}(\omega) &= [\mathbb{Z}_s(\omega) + \mathbb{Z}_{in}(\omega)]^{-1}\underline{V_s}(\omega). \end{aligned} \tag{5.1}$$

Now the voltage and current delivered across the load can be conventionally represented as

$$\begin{aligned} V(t) &= V_I(t) + V_R(t), \\ i(t) &= i_I(t) - i_R(t), \end{aligned} \tag{5.2}$$

where $V_I(t)$ and $V_R(t)$ are the incident and reflected voltages, respectively, while $i_I(t)$ and $i_R(t)$ are the incident and reflected currents, respectively. Further, the Fourier transforms of the incident waveforms, $V_I(t)$ and $i_I(t)$, are related by the relation $V_I(\omega) = Z_s(\omega)I_I(\omega)$, and similarly $V_R(\omega) = Z_s(\omega)I_R(\omega)$ for the reflected waveforms. Thus the relations in (5.2) can be written in terms of the frequencyvectors of the incident and reflected voltages as

$$\begin{aligned} \underline{V}(\omega) &= \underline{V_I}(\omega) + \underline{V_R}(\omega), \\ \underline{I}(\omega) &= \mathbb{Z}_s^{-1}(\omega)\left[\underline{V_I}(\omega) - \underline{V_R}(\omega)\right]. \end{aligned} \tag{5.3}$$

Then substituting (5.1) in (5.3) and simplifying gives

$$\underline{V_R}(\omega) = \left[\mathbb{Z}_{in}(\omega) - \mathbb{Z}_s(\omega)\right]\left[\mathbb{Z}_{in}(\omega) + \mathbb{Z}_s(\omega)\right]^{-1}\underline{V_I}(\omega). \tag{5.4}$$

Let us define $\underline{V_R}(\omega) = \mathbb{S}_{11}(\omega)\underline{V_I}(\omega)$ (analagous to the LTI case, where $V_R(\omega) = S_{11}(\omega)V_I(\omega)$). Then we get

$$\mathbb{S}_{11}(\omega) = \left[\mathbb{Z}_{in}(\omega) - \mathbb{Z}_s(\omega)\right]\left[\mathbb{Z}_{in}(\omega) + \mathbb{Z}_s(\omega)\right]^{-1}. \tag{5.5}$$

The matrix, $\mathbb{S}_{11}(\omega)$, that relates the frequency vector of the reflected wave to the incident wave can be said to be the conversion matrix corresponding to the "*LPTV reflection coefficient*". Let us express $\mathbb{S}_{11}(\omega)$ in the general form of a conversion matrix like in (4.6)

$$\mathbb{S}_{11}(\omega) = \begin{bmatrix} \gamma_{-K,-K}(\omega) & \cdots & \gamma_{-K,0}(\omega) & \cdots & \gamma_{-K,K}(\omega) \\ \vdots & \ddots & \vdots & \iddots & \vdots \\ \gamma_{0,-K}(\omega) & \cdots & \gamma_{0,0}(\omega) & \cdots & \gamma_{0,K}(\omega) \\ \vdots & \iddots & \vdots & \ddots & \vdots \\ \gamma_{K,-K}(\omega) & \cdots & \gamma_{K,0}(\omega) & \cdots & \gamma_{K,K}(\omega) \end{bmatrix}. \tag{5.6}$$

Each element $\gamma_{i,j}(\omega)$ in $\mathbb{S}_{11}(\omega)$ relates the reflected wave generated at a frequency of $(j\omega_p+\omega)$ due to an incident wave at a frequency of $(i\omega_p+\omega)$, ω_p being the fundamental frequency of the system. In an LTI system, $\gamma_{i,j}(\omega) = 0$ when $i \neq j$ because there is no frequency translation possible. Hence, $\mathbb{S}_{11}(\omega)$ is diagonal, which is expected since $\mathbb{Z}_{in}(\omega)$ is also diagonal for LTI system. In an LPTV circuit this is not true in general, implying that an incident wave can potentially create reflections at both its own frequency, as well as around harmonics of the fundamental frequency of the LPTV system.

In an receiver, one is generally interested in the amount of re-radiation of the in-band incident wave. While the S_{11} in the LTI sense (corresponding to terms of the form $\gamma_{i,i}(\omega)$ in

(5.6)) may need to be minimized to fulfill requirements similar to LTI receivers, reflections at non-input frequencies could be more problematic, since they are re-radiated at the antenna to frequencies other than the receiver's operating channel (possibly causing unwanted interference to other wireless systems). We can use the non-diagonal terms in $\mathbb{S}_{11}(\omega)$ to evaluate the amount of re-radiation.

In most LPTV receiver front-ends, such as N-path filters and mixer-first receivers, the fundamental frequency, ω_p, is the same as the LO frequency of the receiver. Hence, the in-band incident signal is expected to be around frequencies of $\pm\omega_p$. Thus for computing re-radiation, the components of interest in $\mathbb{S}_{11}(\omega)$ are of the those of the form $\gamma_{i,1}(\omega)$ and $\gamma_{i,-1}(\omega)$. For example, the total fraction of the in-band incident power at a frequency, $\omega_p+\omega$, reflected back to the antenna is given by $\sum_{i=-K}^{K} |\gamma_{i,1}(\omega)|^2$, with $|\gamma_{1,1}(\omega)|^2$ being the fraction of in-band reflected power.

We will now use the above results to discuss impedance matching in a few typical LPTV receiver front-ends.

5.3 FA-Based Receiver Front-Ends

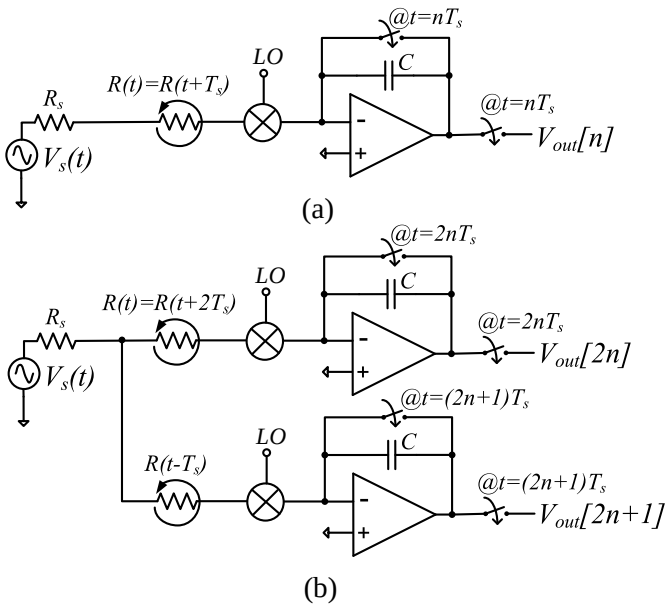

Figure 5.2: FA-based receiver front-ends

In the FA-based receiver front-ends discussed in Chapters 2 and 3 (shown in 5.2), the input impedance is simply a periodically time-varying resistance $R_{in}(t)$. For example, in case of the time-interleaved FA-based receiver front-end shown in Fig. 5.2(b), $R_{in}(t) = R(t)||R(t-T_s)$. Thus the ideal input impedance is simply given by the conversion matrix of $R_{in}(t)$, i.e., $\mathbb{R}_{in}$. Hence $\mathbb{S}_{11}(\omega)$ is simply given by

$$\mathbb{S}_{11}(\omega) = [\mathbb{R}_{in} - R_s\mathbb{I}]\,[\mathbb{R}_{in} + R_s\mathbb{I}]^{-1}, \tag{5.7}$$

where R_s is the source impedance. Note that $\mathbb{R}_{in}$ is a Hermitian Toeplitz matrix (since $R_{in}(t)$ is simply an LPTV resistance). While the matrix $\mathbb{S}_{11}(\omega)$ in (5.7) is a $(2K+1)\times(2K+1)$ matrix, with K chosen to be large enough to get accurate results, the result converges to the true solution as $K \to \infty$.

While the converged result cannot be easily obtained for an arbitrary LPTV circuit, it can be obtained for (5.7). Let $\mathbb{X}_K = \mathbb{R}_{in} + R_s\mathbb{I}$ denote a $(2K+1)\times(2K+1)$ matrix. Considering the sequence of matrices, $\{\mathbb{X}_K\}$, it is easy to see that each matrix in the sequence, $\mathbb{X}_K$, is also Hermitian Toeplitz whose elements can also be shown to be the Fourier series coefficients of the periodic function, $x(t) = R_{in}(t) + R_s > 0$. Using Lemma 4.5 in [38] it can be shown that $\left\{\mathbb{X}_K^{-1}\right\}$ will converge to be the conversion matrix of $1/x(t)$. Further, using the same Lemma it can thus be proved that $[\mathbb{R}_{in} - R_s\mathbb{I}]\,[\mathbb{R}_{in} + R_s\mathbb{I}]^{-1}$ will also converge to be the conversion matrix of $[R_{in}(t) - R_s]\,[R_{in}(t) + R_s]^{-1}$ as $K \to \infty$. Hence $\mathbb{S}_{11}(\omega)$ in (5.7) converges to be the conversion matrix of

$$\Gamma(t) = \frac{R_{in}(t) - R_s}{R_{in}(t) + R_s}, \tag{5.8}$$

that is simply the time-varying input reflection coefficient of the circuit. Thus, the S_{11} of the circuit is simply given by the diagonal elements of $\mathbb{S}_{11}(\omega)$, i.e., $mean\,[\Gamma(t)]$, and so

$$S_{11,ideal} = mean\left[\frac{R(t) - R_s}{R(t) + R_s}\right], \tag{5.9}$$

that is exactly as noted in (2.10).

Presence of parasitics can also be easily considered. For example, consider a parasitic capacitance, C_p at the input of the receiver. Then the input impedance expression simply changes to

$$\mathbb{Z}_{in}(\omega) = \left(\mathbb{Y}_p + \mathbb{R}_{in}^{-1}\right)^{-1},$$

where $\mathbb{Y}_L(\omega) = jC_p\mathbf{\Omega}(\omega)$ is the admittance conversion matrix of C_p. Hence the S_{11} becomes frequency dependent. Figure 5.3(a) shows the effect of C_p on the S_{11} of the receiver front-end when the resistance variation is designed to give a wideband $S_{11,ideal}$ = -20dB, calculated for $K = 1000$. It can be seen that the ideal S_{11} remains -20dB regardless of frequency as shown by calculations as well as Sprectre RF PSS-PSP simulations. With the presence of C_p, the S_{11} degrades it higher frequencies. Further, comparison with the measured S_{11} in Fig. 3.18 with the estimated C_p = 2pF in Fig. 5.3(b) shows that the calculations matches well with measurements.

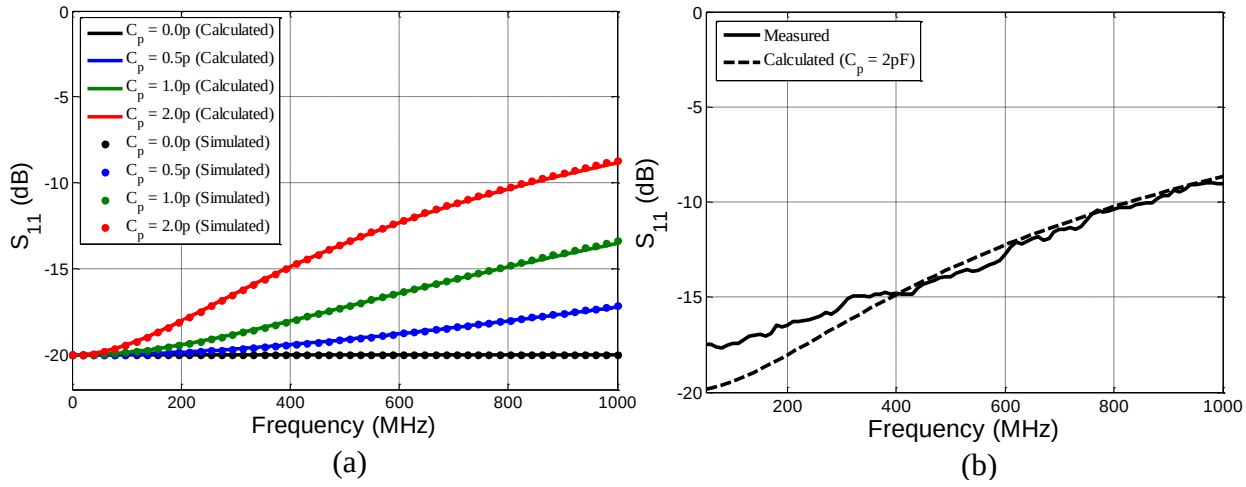

Figure 5.3: a) Wideband S_{11} of the FA-based receiver front-ends with the presence of parasitic capacitance at the antenna input, b) comparison of the measured S_{11} in Fig. 3.18 to calculations

While S_{11} is important, it is also necessary to quantify the total amount of reflected power from the antenna. For example, in the ideal case we showed that $\mathbb{S}_{11}(\omega)$ is simply the conversion matrix of the time-varying reflection coefficient, $\Gamma(t)$, as given by (5.8). Note

that since $R_{in}(t)$ is periodic with period of T_s, so is $\Gamma(t)$ and so it can be expanded as

$$\Gamma(t) = \sum_{n=-\infty}^{\infty} \gamma_n \exp\left(j\frac{2n\pi}{T_s}\right). \tag{5.10}$$

Hence the components of $\mathbb{S}_{11}(\omega)$ in (5.6) are given by $\gamma_{i,j}(\omega) = \gamma_{j-i}$, i.e., the Fourier series coefficients of $\Gamma(t)$. Thus, for an in-band incident wave, the total fraction of power reflected can be found to be $\sum_{n=-\infty}^{\infty} |\gamma_n|^2 = mean\left[|\Gamma(t)|^2\right]$ (by Parseval's theorem). In case of the resistance variation in Fig. 3.4, this is about -8.2dB. Note that an additional constraint on $mean\left[|\Gamma(t)|^2\right]$ can be added to the FA filter design routine if the fraction needs to be improved (possibly at the cost of stop-band suppression, A_{stop}).

5.4 Mixer-First Receivers

Let us consider the 4-path mixer-first receiver shown in Fig. 4.8. The input impedance was found to be in (4.23) as

$$\mathbb{Z}_{in}(\omega) = \left(\mathbb{Y}_p + \sum_{n=0}^{3} \left[\mathbb{R}_n + \mathbb{Z}_L\right]^{-1}\right)^{-1} \tag{5.11}$$

that includes a parasitic capacitance, $C_p = \alpha C_L$, at the receiver input. Then the $\mathbb{S}_{11}(\omega)$ matrix can be found simply using (5.5). Figure 5.4 shows the input impedance obtained, and the corresponding calculated S_{11} (for $K = 1000$) around the LO frequency with R_s=50Ω, R_{on}=0Ω, R_{off}=10kΩ, $R_L = (\pi^2/2)\,R_s$ and switching frequency $\omega_p = 2\pi/T_p$ such that $\omega_p/\omega_{RC} = 50$, where $\omega_{RC} = 1/R_sC_L$. It is seen that when $\alpha = 0$ the input impedance is about 50Ω at the center frequency as expected. The calculated S_{11}, given by the diagonal entries of $\mathbb{S}_{11}(\omega)$ (specifically $\gamma_{1,1}(\omega)$ for S_{11} around the LO frequency), is only -18dB (verified using Spectre RF PSS-PSP simulations) indicating that simply setting input impedance to 50Ω does not guarantee perfect impedance matching in an LPTV circuit.

The input impedance is disturbed by the presence of parasitic capacitance at the antenna caused due to the mixer switches. This is because the switches have to be made large to reduce its ON resistance that directly limits the out-of-band rejection of the realized band-

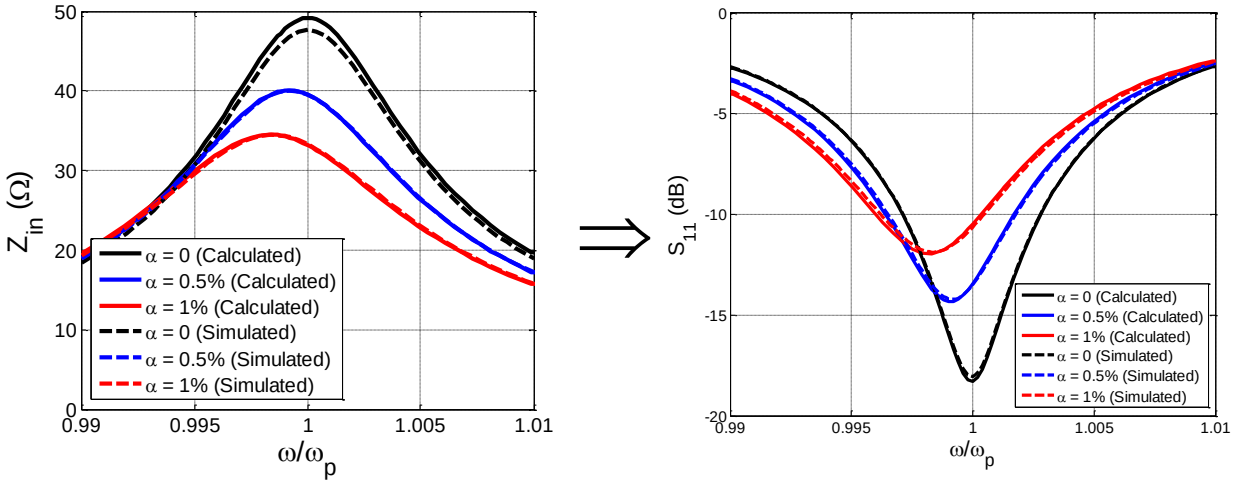

Figure 5.4: Input impedance and S_{11} around the LO frequency in a mixer-first receiver with parasitic capacitance at the antenna input

pass filter [19]. Hence it can be seen from the results shown in Fig. 5.4 that the S_{11} degrades as well. Further, the narrowband where the S_{11} is acceptable shifts away from the center. Hence, the switch sizes have to be limited to manage this effect.

As noted before, the in-band S_{11} is not enough to calculate the total reflected power. For that, the non-diagonal terms of the matrix, $\mathbb{S}_{11}(\omega)$, have to be considered as described previously. Figure 5.5 shows the calculated fraction of power reflected for an in-band input incident wave (without any parasitic capacitance), where $|\gamma_{i,1}(\Delta\omega)|^2$ is the fraction of the incident power reflected to the frequency, $i\omega_p + \Delta\omega$, when the incident wave is at the frequency, $\omega_p + \Delta\omega$. Figure 5.5 also shows the total input power reflected that is found by summing the reflected powers at all frequencies (frequencies up to $\pm 50\omega_p$ are considered).

It can be seen that a non-negligible fraction of power is reflected when $i = 4k + 1$, k being an integer, meaning that reflections are present at frequency offsets of $4\omega_p$ and its multiples from the input. In general, reflections are present at frequency offsets of $N\omega_p$ and its multiples with the use of an N-path mixer. Looking at Fig. 5.5, it can also be noted that the total fraction of reflected power is about -7.3dB when the incident wave is at the LO frequency. This is significant, and needs to be considered when designing systems using mixer-first receivers that employ impedance matching with the structure in Fig. 4.8.

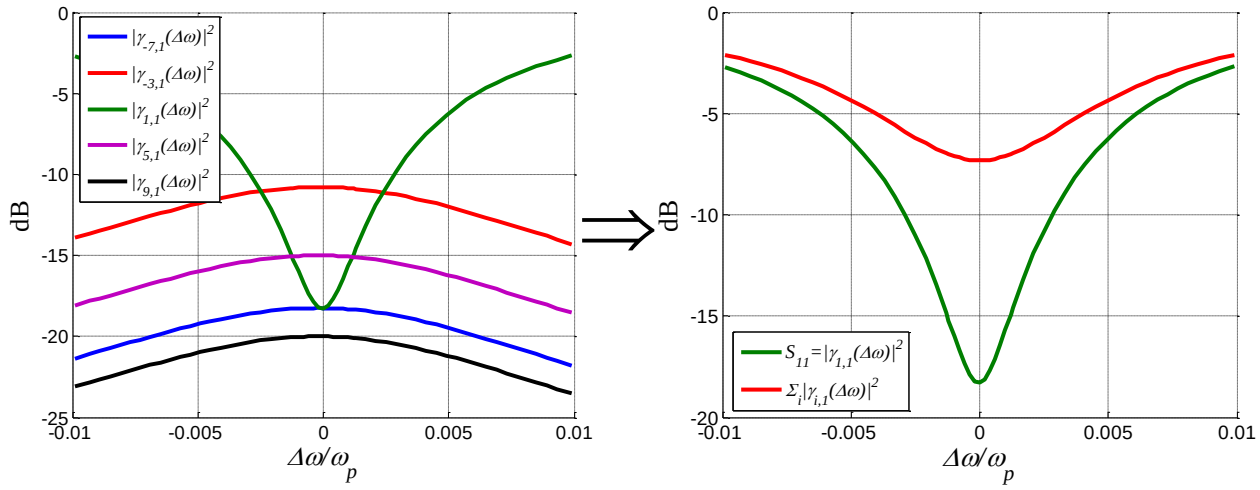

Figure 5.5: Calculated fraction of input power reflected to LO harmonics, and the total fraction of power reflected (considering up to 50 harmonics) for an incident wave around the LO frequency in a mixer-first receiver

5.5 Switched-Capacitor Receiver Front-Ends

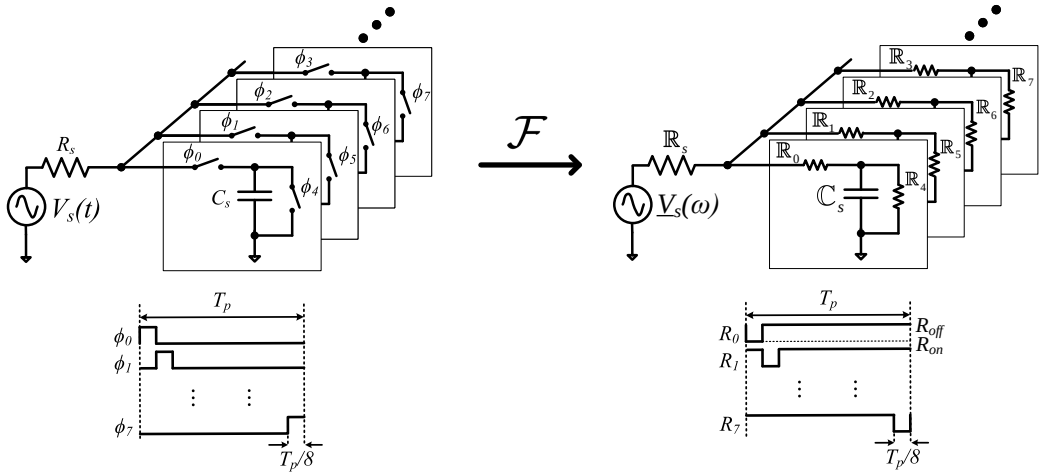

Figure 5.6: A simple 8-path receiver front-end with switched-capacitors for impedance matching, and its frequency-domain conversion matrix equivalent circuit

An alternative method proposed to achieve impedance matching with LPTV circuits is the switched-capacitor impedance matching technique [14]. By charging and discharging load capacitors, C_s, in N paths, where each path is turned on $1/N^{th}$ of the LO period,

T_p, a switched-capacitor resistance is achieved at the input that is matched to the source impedance, R_s. Figure 5.6 shows an 8-path example that was implemented in [14]. It was shown that a wideband match is achieved in this circuit for $C_s \approx 0.63/f_s R_s$, where $f_s = 8/T_p$. The conversion matrix approach can easily be applied to this circuit as well with the frequency-domain conversion matrix equivalent circuit shown in Fig. 5.6. By inspection, the input impedance of the circuit can be derived using series and parallel combination of impedances as

$$\mathbb{Z}_{in}(\omega) = \left(\sum_{i=0}^{N-1} \left[\mathbb{R}_i + \left\{ \mathbb{Y}_s(\omega) + \mathbb{R}_j^{-1} \right\}^{-1} \right]^{-1} \right)^{-1}, \tag{5.12}$$

where $\mathbb{R}_i$ and $\mathbb{R}_j$ are the conversion matrices of the i^{th} paths input-switch and the reset-switch resistances respectively with $j = \left(i + \frac{N}{2}\right) \bmod N$, and $\mathbb{Y}_s(\omega) = jC_s\mathbf{\Omega}(\omega)$ is the admittance of the load capacitor, C_s. Hence using (5.12), $\mathbb{S}_{11}(\omega)$ can be easily calculated. Figure 5.7 shows the calculated input impedance and S_{11} of the circuit (for $K = 1000$) with R_s=50Ω, R_{on}=0.5Ω and R_{off}=50kΩ. The results compare very well with simulated results using Spectre RF and the results in [14]. Note that input impedance is not exactly 50Ω at DC, but achieved S_{11} is better than -25dB.

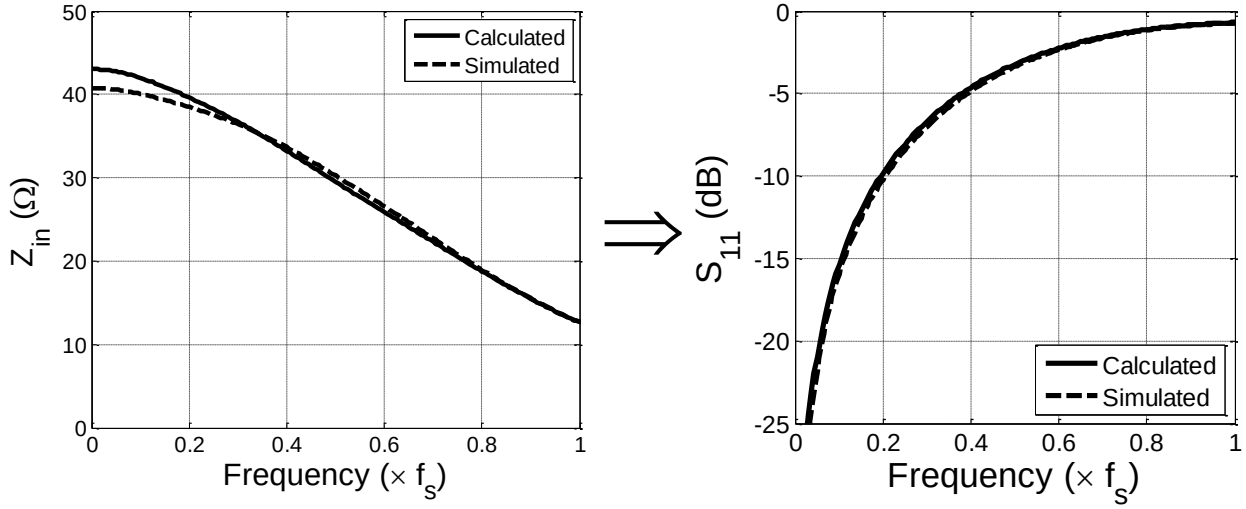

Figure 5.7: Input impedance and S_{11} of the switched-capacitor receiver front-end with switch R_{on}=0.5Ω

The analysis reveal the effect of non-zero switch resistances as well. For example, consider the case where the input and reset switches have ON resistances of $R_{on,1}$ and $R_{on,2}$, respectively. This can be simply included while constructing the $\mathbb{R}_i$ and $\mathbb{R}_j$ matrices in (5.12). Figure 5.8 shows that calculated S_{11} for practical values of $R_{on,1}$ and $R_{on,2}$. It can be noted that the results match very well with results from Sprectre RF simulations, as well as simulation results shown in [14]. While calculated results were not available for all cases in [14], they are easily available using the conversion matrix analysis technique.

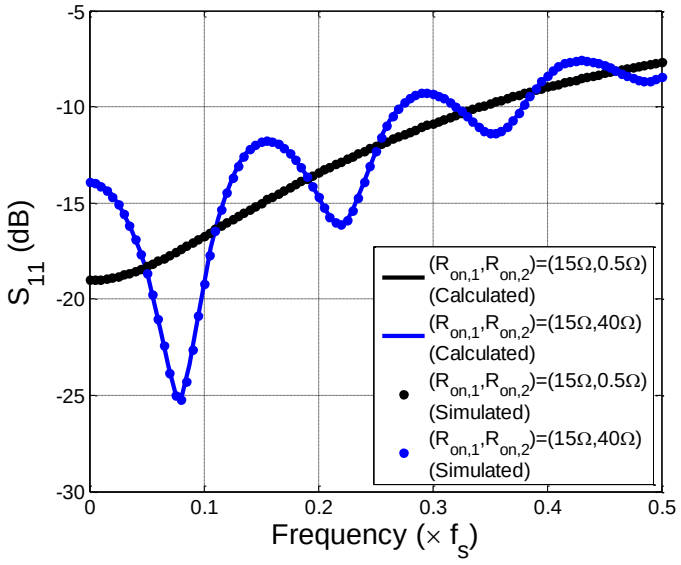

Figure 5.8: Effect of switch resistances on S_{11} of the switched-capacitor receiver front-end with input and reset switch ON resistances of $R_{on,1}$ and $R_{on,2}$, respectively

Finally, we can look at the non-diagonal terms of the matrix, $\mathbb{S}_{11}(\omega)$, to consider reflections to non-input frequencies. Figure 5.9 shows the calculated fraction of power reflected for an in-band input incident wave (with $R_{on,1} = R_{on,2} = 0.5\Omega$), where $|\gamma_{i,1}(\Delta\omega)|^2$ is the fraction of the incident power reflected to the frequency, $i\omega_p + \Delta\omega$, when the incident wave is at the frequency, $\omega_p + \Delta\omega$. Figure 5.9 also shows the total input power reflected that is found by summing the reflected powers at all frequencies (frequencies up to $\pm 50\omega_p$ are considered).

It can be seen that a non-negligible fraction of power is reflected when $i = 8k + 1$, k being an integer. Hence, reflections are present at frequency offsets of $8\omega_p$ and its multiples

from the input (which is expected since the receiver in Fig. 5.6 uses 8 paths). Looking at Fig. 5.9, it can be noted that the total fraction of reflected power is about -6.8dB when the incident wave is at the LO frequency. Again, this is a significant amount, and needs to be considered during system designs.

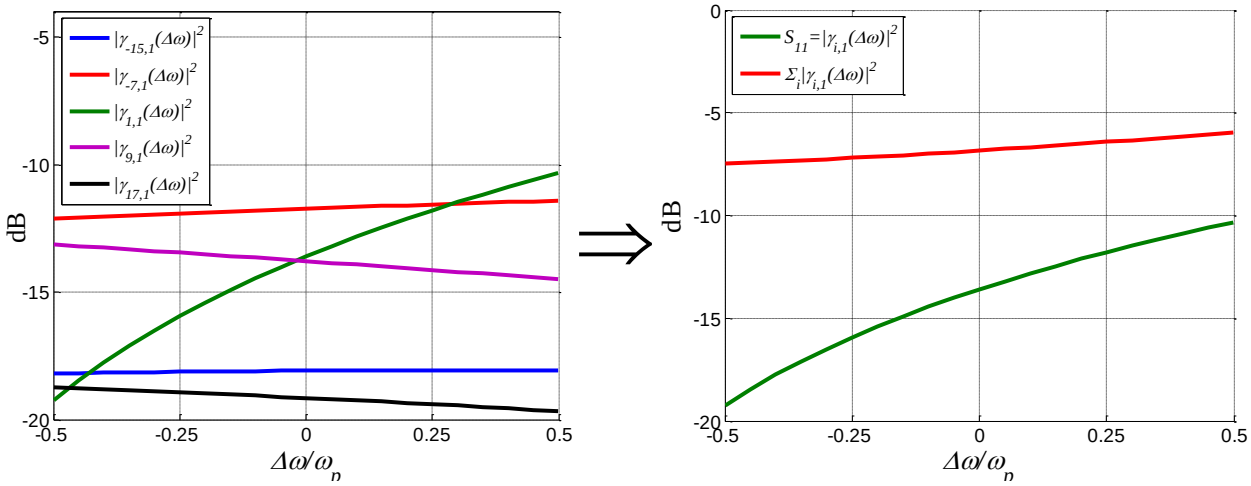

Figure 5.9: Calculated fraction of input power reflected to LO harmonics, and the total fraction of power reflected (considering up to 50 harmonics) for an incident wave around the LO frequency in a switched-capacitor receiver front-end

CHAPTER 6

Conclusion

6.1 Summary

This dissertation introduced a new approach based on linear, periodically time-varying circuits (LPTV) to realizing programmable receivers. Further an analysis technique based on the concept of conversion matrices was also developed to analyze general LPTV circuits.

Chapter 2 introduced a programmable receiver front-end based on the concept of Filtering-by-Aliasing (FA). Using a time-varying integrate-and-dump circuit with an LPTV resistor, a sharp programmable filtering response was achieved at RF by leveraging the FA technique. Furthermore, an additional S_{11} constraint was imposed to allow for impedance matching to the antenna. The implemented receiver achieved high close-in linearity with >17dBm of IIP_3 at only 1.2×BW frequency offset, while achieving a wideband impedance match with S_{11} better than -10dB throughout the LO range.

Chapter 3 detailed a time-interleaved Filtering-by-Aliasing receiver front-end. By using two time-interleaved integrate-and-dump circuits, sharper filtering is achieved, while simultaneously maintaining a good S_{11}. Techniques were introduced to mitigate important circuit parasitics, while requirements on matching between paths were also derived. The implemented prototype achieve a stop-band suppression of 70dB with a transition band of only 4×BW.

Chapter 4 developed a systematic approach to analyze LPTV circuits based on the concept of conversion matrices. The presented approach uses simple matrix-based extensions that allows LPTV circuits to be analyzed easily using familiar circuit theorems such as KVL and KCL, in a manner similar to LTI circuits. The approach is fairly straightforward and

can easily include circuit non-idealities and parasitics that were fairly difficult to incorporate in prior approaches. Example analysis of a mixer-first receiver and an N-path filter were also presented.

Finally, Chapter 5 described a conversion matrix-based approach to characterize impedance matching in general LPTV circuits. By simply computing the conversion matrix of the input impedance of an LPTV circuit, its S_{11} can be calculated similar to an LTI circuit. Further, reflected power at non-input frequencies could also be calculated. Example application to mixer-first receivers, switched-capacitor receiver front-ends and FA-based receiver front-ends agree well with simulations and prior-art.

6.2 Future Work

The noise figure of the implemented FA-based receiver front-ends is limited by the presence of up-front LPTV resistors. Future work could explore incorporating noise cancellation techniques similar to state-of-the-art mixer-first receivers [21] to improve the noise figure. Further improvements to filter stop-band suppression may also be necessary to realize a true SDR receiver, but currently the main limitation is the realized dynamic range of the RDACs during receiver operation. Perhaps approaches such as cascading multiple LPTV stages might prove useful is reducing dynamic range requirements. Automated RDAC calibration techniques will help as well, allowing higher RDAC accuracy during runtime.

Future work on the conversion matrix-based analysis technique could focus on deriving closed-form expressions for common LPTV circuits. A potential approach would be to analyze parasitics and non-idealities as small perturbations from the conversion matrices in the ideal case. This might allow for making simplifying assumptions that can result in closed-form expressions.

REFERENCES

[1] "Evolved universal terrestrial radio access (E-UTRA); physical channels and modulation (release 14)," *Tech. Rep. 36.211 (v14.2.0)*. 3rd Generation Partnership Project (3GPP), 2017.

[2] Flores, A. B.; Guerra, R. E.; Knightly, E. W.; Ecclesine, P.; Pandey, S., "IEEE 802.11af: a standard for TV white space spectrum sharing," *IEEE Communications Magazine*, vol. 51, no. 10, pp. 92-100, October 2013.

[3] Iera, A.; Floerkemeier, C.; Mitsugi, J.; Morabito, G., "The Internet of things [Guest Editorial]," *IEEE Wireless Communications*, vol. 17, no. 6, pp. 8-9, December 2010.

[4] Nekovee, M., "Cognitive Radio Access to TV White Spaces: Spectrum Opportunities, Commercial Applications and Remaining Technology Challenges," *New Frontiers in Dynamic Spectrum, 2010 IEEE Symposium on* , vol., no., pp.1,10, 6-9 April 2010.

[5] Mitola, J., "The software radio architecture," *IEEE Communications Magazine*, vol. 33, no. 5, pp. 26-38, May 1995.

[6] Murmann, B., "ADC Performance Survey 1997-2016," [Online]. Available: http://web.stanford.edu/ murmann/adcsurvey.html.

[7] Abidi, A.A., "The Path to the Software-Defined Radio Receiver," *Solid-State Circuits, IEEE Journal of*, vol.42, no.5, pp.954,966, May 2007.

[8] Rachid, M.; Pamarti, S.; Daneshrad, B., "Filtering by Aliasing," *in Signal Processing, IEEE Transactions on*, vol.61, no.9, pp.2319-2327, May1, 2013.

[9] Nguyen C. T. C., "Integrated Micromechanical Radio Front-Ends," *2008 International Symposium on VLSI Technology, Systems and Applications (VLSI-TSA)*, Hsinchu, 2008, pp. 3-4.

[10] Mirzaei, A.; Bagheri, R.; Chehrazi, S.; Abidi, A. A., "A second-order anti-aliasing prefilter for an SDR receiver," *Proceedings of the IEEE 2005 Custom Integrated Circuits Conference, 2005*, San Jose, CA, 2005, pp. 629-632.

[11] Bagheri, R. et al., "An 800-MHz6-GHz Software-Defined Wireless Receiver in 90-nm CMOS," *Solid-State Circuits, IEEE Journal of*, vol. 41, no. 12, pp. 2860-2876, Dec. 2006.

[12] Tohidian, M.; Madadi, I.; Staszewski, R. B., "3.8 A fully integrated highly reconfigurable discrete-time superheterodyne receiver," *2014 IEEE International Solid-State Circuits Conference Digest of Technical Papers (ISSCC)*, San Francisco, CA, 2014, pp. 1-3.

[13] Chen, R.; Hashemi, H., "A 0.5-to-3 GHz Software-Defined Radio Receiver Using Discrete-Time RF Signal Processing," *Solid-State Circuits, IEEE Journal of*, vol. 49, no. 5, pp. 1097-1111, May 2014.

[14] Xu, Y.; Kinget, P. R., "A Switched-Capacitor RF Front End With Embedded Programmable High-Order Filtering," *Solid-State Circuits, IEEE Journal of*, vol. 51, no. 5, pp. 1154-1167, May 2016.

[15] el Oualkadi, A.; El Kaamouchi, M.; Paillot, J.-M.; Vanhoenacker-Janvier, D.; Flandre, D., "Fully Integrated High-Q Switched Capacitor Bandpass Filter with Center Frequency and Bandwidth Tuning," *2007 IEEE Radio Frequency Integrated Circuits (RFIC) Symposium*, Honolulu, HI, 2007, pp. 681-684.

[16] Ghaffari, A.; Klumperink, E.A.M.; Soer, M. C M; Nauta, B., "Tunable High-Q N-Path Band-Pass Filters: Modeling and Verification," *Solid-State Circuits, IEEE Journal of*, vol.46, no.5, pp.998,1010, May 2011.

[17] Darvishi, M.; van der Zee, R.; Klumperink, E. A. M.; Nauta, B., "Widely Tunable 4th Order Switched G_m-C Band-Pass Filter Based on N-Path Filters," *Solid-State Circuits, IEEE Journal of*, vol. 47, no. 12, pp. 3105-3119, Dec. 2012.

[18] Darvishi, M.; van der Zee, R.; Nauta, B., "Design of Active N-Path Filters," *Solid-State Circuits, IEEE Journal of*, vol. 48, no. 12, pp. 2962-2976, Dec. 2013.

[19] Andrews, C.; Molnar, A.C.,, "Implications of Passive Mixer Transparency for Impedance Matching and Noise Figure in Passive Mixer-First Receivers," *Circuits and Systems I: Regular Papers, IEEE Transactions on* , vol.57, no.12, pp.3092,3103, Dec. 2010.

[20] Mirzaei, A.; Darabi, H.,, "Analysis of Imperfections on Performance of 4-Phase Passive-Mixer-Based High-Q Bandpass Filters in SAW-Less Receivers," *Circuits and Systems I: Regular Papers, IEEE Transactions on* , vol.58, no.5, pp.879,892, May 2011.

[21] Murphy, D. et al., "A Blocker-Tolerant, Noise-Cancelling Receiver Suitable for Wideband Wireless Applications," *Solid-State Circuits, IEEE Journal of*, vol.47, no.12, pp.2943-2963, Dec. 2012.

[22] Chen, R.; Hashemi, H., "19.3 Reconfigurable SDR receiver with enhanced front-end frequency selectivity suitable for intra-band and inter-band carrier aggregation," *2015 IEEE International Solid-State Circuits Conference Digest of Technical Papers (ISSCC)*, San Francisco, CA, 22-26 Feb. 2015, pp. 1-3.

[23] Franks, L. E.; Sandberg, I. W., "An alternative approach to the realization of network transfer functions: The N-path filter," *The Bell System Technical Journal*, vol. 39, no. 5, pp. 1321-1350, Sept. 1960.

[24] Sinha, N.; Rachid, M.; Pamarti, S., "An 8mW, 1GHz span, passive spectrum scanner with $>$ +31dBm out-of-band IIP3," *2016 IEEE Radio Frequency Integrated Circuits (RFIC) Symposium*, San Francisco, CA, 2016, pp. 278-281.

[25] Kaiser, J.; Schafer. R., "On the use of the I0-sinh window for spectrum analysis," *IEEE Transactions on Acoustics, Speech, and Signal Processing*, vol. 28, no. 1, pp. 105-107, February 1980.

[26] Hameed, S.; Sinha, N.; Rachid, M.; Pamarti, S., "A Programmable Receiver Front-End Achieving >17dBm IIP_3 at <1.25×BW Frequency Offset," *2016 IEEE International Solid-State Circuits Conference Digest of Technical Papers (ISSCC)*, pp.446,447, 31 Jan.-4 Feb. 2016.

[27] Zadeh, L. A., "Frequency Analysis of Variable Networks," *Proceedings of the IRE*, vol.38, no.3, pp.291,299, March 1950.

[28] Yuh S.; Frisch, I. T., "A General Theory of Commutated Networks," *Circuit Theory, IEEE Transactions on* , vol.16, no.4, pp.502,508, Nov 1969.

[29] Strom, T.; Signell, S., "Analysis of periodically switched linear circuits," *Circuits and Systems, IEEE Transactions on* , vol.24, no.10, pp.531,541, Oct 1977.

[30] Vanassche, P.; Gielen, G.; Sansen, W., "Symbolic modeling of periodically time-varying systems using harmonic transfer matrices," *Computer-Aided Design of Integrated Circuits and Systems, IEEE Transactions on*, vol.21, no.9, pp.1011,1024, Sep 2002.

[31] Soer, M. C M; Klumperink, E.A.M.; de Boer, P.-T.; van Vliet, F.E.; Nauta, B., "Unified Frequency-Domain Analysis of Switched-Series- *RC* Passive Mixers and Samplers," *Circuits and Systems I: Regular Papers, IEEE Transactions on*, vol.57, no.10, pp.2618,2631, Oct. 2010.

[32] Mirzaei, A.; Darabi, H.; Leete, J.C.; Yuyu Chang, "Analysis and Optimization of Direct-Conversion Receivers With 25% Duty-Cycle Current-Driven Passive Mixers," *Circuits and Systems I: Regular Papers, IEEE Transactions on* , vol.57, no.9, pp.2353,2366, Sept. 2010.

[33] Roychowdhury, J., "Reduced-order modeling of time-varying systems," *Circuits and Systems II: Analog and Digital Signal Processing, IEEE Transactions on*, vol.46, no.10, pp.1273,1288, Oct 1999.

[34] Maas, S. A. , *Nonlinear microwave and RF circuits*, 2nd Ed., Artech House, 2003.

[35] Chua, L.O.; Ng, C.Y., "Frequency-domain analysis of nonlinear systems: formulation of transfer functions," *Electronic Circuits and Systems, IEE Journal on*, vol.3, no.6, pp.257,269, November 1979.

[36] Kundert, K.S.; Sangiovanni-Vincentelli, A., "Simulation of Nonlinear Circuits in the Frequency Domain," *Computer-Aided Design of Integrated Circuits and Systems, IEEE Transactions on* , vol.5, no.4, pp.521,535, October 1986.

[37] Roychowdhury, J.; Long, D.; Feldmann, P., "Cyclostationary noise analysis of large RF circuits with multi-tone excitations," *Custom Integrated Circuits Conference, 1997., Proceedings of the IEEE 1997*, vol., no., pp.383,386, 5-8 May 1997.

[38] Gray, R. M., "Toeplitz and Circulant Matrices: A review," *Foundations and Trends in Communications and Information Theory*, vol.2, issue.3, pp.155-239, 2006.